Experimental Analysis of Permeability Barriers to Hydraulic Fracture Propagation

by

TIMOTHY SEAN QUINN

B.S. Mech. Eng., University of Dayton (1990)
M.S. Mech. Eng., Massachusetts Institute of Technology (1992)

Submitted to the Department of
Mechanical Engineering
In Partial Fulfillment of the Requirements
for the Degree of

DOCTOR of PHILOSOPHY
in MECHANICAL ENGINEERING

at the

MASSACHUSETTS INSTITUTE OF TECHNOLOGY

May 1994

Signature of Author _____
Department of Mechanical Engineering
May 1994

Certified by _____
Michael P. Cleary
Adjunct Professor of Mechanical Engineering
Thesis Supervisor

Accepted by _____
Professor Ain A. Sonin
Chairman of Mechanical Engineering Departmental Committee on Graduate Students

Experimental Analysis of Permeability Barriers to Hydraulic Fracture Propagation

by

TIMOTHY SEAN QUINN

Submitted to the Department of Mechanical Engineering
in May 1994 in partial fulfillment of the requirements
for the Degree of Doctor of Philosophy
in Mechanical Engineering

ABSTRACT

The effects of stratified permeability on hydraulic fracture propagation are modeled with an Interface Separation Apparatus. The existence of permeability barriers to hydraulic fracture growth is verified and the magnitude of the barriers is quantified as a function of material parameters. The analytical and experimental models focus on permeability contrasts, with fracture initiation in a low permeability region and propagation into a higher permeability zone. The permeable media are simulated using bonded granular materials which allow tight control over the material properties.

An analytical model is developed describing the two-dimensional leakoff near the fracture tip. Experimental studies are compared against this tip leakage model to verify the steady state leakage approximations for circular geometries. The two-dimensional model predicts results which more accurately match laboratory experiments than simple one-dimensional models.

The analytical model is applied to describe leakoff behavior as the fracture tip reaches a higher permeability interface. A characteristic 'holding time' is derived to describe the time a fracture is delayed as the fracture propagates from a region of low permeability into a higher permeability zone. Experimental results for permeability variations of one to two orders of magnitude are compared against predicted values for fracture holding time.

The experimental data are also used to calibrate the stratified permeability coefficients in a lumped-parameter field simulator. A representative field case is then analyzed using those coefficients as model parameters. The simulator is found to predict fracture growth which matches other field evidence of fracture containment.

The analytical and experimental development provide the first basis for an accurate model to estimate levels of fracture containment under field conditions. Such a capability for analyzing fracture growth can be used to better predict the effect of permeability barriers when executing hydraulic fracture operations in the field.

Thesis Supervisor: Professor M. P. Cleary
Title: Adjunct Professor of Mechanical Engineering

ACKNOWLEDGMENTS

I would like to take a small space here to acknowledge a number of the individuals who have influenced or contributed to this work.

First of all I would like to thank the UROP's. Christian, Paul, and Rebecca have worked the long hours in the lab and helped this project from its inception through the failures, and successes. It is safe to say that this thesis would not have been as thorough or even completed without their help. In the days ahead they will be sorely missed. Christian for the ability to never take a project so seriously that he couldn't have a little fun; Paul for the things he has taught me, and Rebecca, who was there to take care of all of the details. Thank you, and good luck.

I would also like to thank Eddie and Kurt for their help in preparing for Quals. Our Qual meetings and research discussions helped me stay focused. I wish them a luck in finishing up quickly.

Forrest Patterson deserves special note because of the discussions that helped form the theory and experimental techniques included in this work. I wish you luck and may the future find you successful in all you pursue.

Discussions with Dave Barr and Eric Montagut contributed heavily to the development of the analytical models. I am grateful for your assistance and I hope I have also been of some help to you. May you and your families be happy.

Several individuals in the Mechanical Engineering department deserve extra recognition. Leslie Regan was one of the reasons I came to MIT and I hope the department recognizes what a valuable asset that Leslie, Joan, and Susan are to the graduate students at MIT. John O'Brien, Lucie Piazza, and Maurene De Courcey have been there to smooth out the funding problems for the lab. These are the people that never get to see the success of the research but handle the problems cheerfully and efficiently. I wish them luck in their years ahead at MIT.

I would like to thank my committee members, Prof. Kamm and Prof. Einstein. Your input and feedback has helped define the scope of this research. I would like to thank Prof. Cleary for supporting this research and helping to derive the relationship in Equation (2.8). I would also like to thank Prof. Virgil for supplying the materials for the first generation of permeable materials.

Thanking my family is something that should not be taken lightly. I am indebted to them for so much in the past and what I am now has been greatly influenced by their thoughts, actions, and love. I will always be a part of that family and for that I am thankful.

In the same thought I would like to thank my fiancée. Kristin has been there through the long nights, numerous proof readings, and stressful deadlines, and through it all she has been supportive and loving. Thank you and I look forward to spending the rest of our lives together.

TABLE OF CONTENTS

Page

ACKNOWLEDGMENTS 3
TABLE OF CONTENTS 4
LIST OF FIGURES 8
LIST OF TABLES 10
NOMENCLATURE 11
CHAPTER 1 INTRODUCTION AND BACKGROUND 13
1.1 Hydraulic Fracture Propagation 13
1.2 Permeability Issues 15
1.2.1 Fluid Loss 15
1.2.2 Efficiency 16
1.3 Dimensional Scaling 16
1.3.1 Requirements 16
1.4 Previous work 17
1.4.1 Analytical 17
1.4.1.1 1-D Approximations 17
1.4.1.2 Numerical Models 19
1.4.2 Experimental 20
1.4.2.1 DISLASH 21
1.4.2.2 Foam 22
1.4.2.3 Growth Regimes 25
1.5 Current studies 26
1.5.1 Identification of Problem Addressing 26
1.5.1.1 Multiple Permeability Zone Fractures 26
1.5.1.2 Laboratory Scale 27
1.5.2 Contribution 27
1.5.2.3 Experimental Analysis 27
1.5.2.4 Quantify Permeability Barrier "Strength" 28
1.6 Overview 28
CHAPTER 2 DEVELOPMENT OF MODEL 30
2.1 Assumptions 30
2.2 Leakoff Models 32
2.2.1 One-Dimensional Leakoff 33
2.2.2 Near-Tip Leakoff Behavior 35

2.3 Temporal-Spatial Relationship 39
CHAPTER 3 DEVELOPMENT OF SIMULATION 40
3.1 Dimensional Scaling 40
3.1.1 Previous Work 40
3.1.1.1 Verification of Elastic Model 40
3.1.2 Field Scale / Lab Scale 41
3.1.2.1 Properties 41
3.1.2.2 Higher Viscosity 42
3.2 DISLASH 42
3.2.1 Assumptions 42
3.2.1.1 Confining / Contact Stress 42
3.2.1.2 Half-Crack Model Assumptions 43
3.2.1.3 Non-Infinite Medium 43
3.2.1.4 System Compliance / Response Time 44
3.3 Permeable Materials 45
3.3.1 Foams 45
3.3.2 Granular Materials 46
3.3.3 Assumptions / Modeling Requirements 47
3.4 Data Collection 50
3.4.1 Pressures 51
3.4.2 Photographs of Fracture Propagation 51
3.4.3 Penetration Depth 52
3.5 Data Reduction 52
3.5.1 Preflood Zone 53
3.5.2 Pressure 53
CHAPTER 4 TESTING AND RESULTS 54
4.1 Radial Growth 54
4.2 Pressures 56
4.3 Length / Height vs. Time 60
4.4 Comparison to Theory 66
4.5 Agreement / Problems with Numerical Simulators 67
CHAPTER 5 FIELD APPLICATION 68
5.1 North Sea Water Injection 71
5.2 Description of Situation 71
5.3 Numerical Simulation 72

5.3.1 Use of Laboratory Coefficients 72
5.3.2 Fracture Growth 73
5.4 Evidence of Containment 76
CHAPTER 6 CONCLUSIONS AND RECOMMENDATIONS 78
6.1 Role / Contribution of Preflood Zone 78
6.2 Effect of Multi-Zones 78
6.3 Consequences for Field Studies 79
6.4 Recommendations 79
REFERENCES 81
APPENDIX A Conversion Factors 89
APPENDIX B Material Properties 90
B.1 Property Definitions: 90
B.1.1 Permeability: (intrinsic permeability) 90
B.1.2 Hydraulic conductivity: 90
B.1.3 Porosity: 91
B.2 DISLASH parameters: 91
B.2.1 Granular Materials: 94
APPENDIX C Contact Stress Measurement 96
C.1 Introduction and Background 96
C.1.1 Significance 96
C.2.2 Previous Work 97
C.3.3 Current Work 98
C.4 Theoretical Prediction 100
C.5 Experimental Results 100
C.6 Conclusions 103
APPENDIX D Major Modifications to Apparatus 104
D.1 Improved Signal to Noise Ratio 104
D.2 Increased Time Resolution 105
D.3 Other Changes 106
APPENDIX E Permeability Testing 110
E.1 Axial 110
E.1.1 Compressive Permeameter 110
E.2 Transverse 112
E.2.1 COSPERT 112
APPENDIX F Dimensional Scaling 116

F.1 Dimensional Groups 116
F.2 Characteristic Scaling Parameters 118
F.2.1 Characteristic Time 118
F.2.2 Characteristic Pressure 119
F.2.3 Characteristic Radius 119
APPENDIX G Inverse Permeability Barriers 120

LIST OF FIGURES

Table Page

Figure 1.1 Typical Field Hydraulic Fracture 15
Figure 1.2 Fluid Penetration (Dry Medium) 17
Figure 1.3 One-Dimensional Zones of Leakoff and Thermal Penetration 19
Figure 1.4 Side and Top Views of Smaller DISLASH 21
Figure 1.5 Axial and Transverse Permeabilities of Scott Felted Foam. 23
Figure 1.6 Hypothetical Foam Schematic 24
Figure 1.7 Axial and Transverse Permeabilities of Gray Foam 25
Figure 1.8 Typical Field Strata with Varying Confining Stress 26
Figure 2.1 Hydraulic Fracture Approaching High Permeability Zone 32
Figure 2.2 Hydraulic Fracture Approaching High Permeability Zone (3 Views) . 33
Figure 2.3 One -Dimensional Leakoff Model 34
Figure 2.4 Pressure Distribution Along Fracture 34
Figure 2.5 Leakoff Through Fracture Tip 36
Figure 2.6 Two-Dimensional Leakoff Models 37
Figure 3.1 Effect of Free Surface on Stress Intensity Factor 44
Figure 3.2 Flow Boundary Conditions 48
Figure 3.3 Hypothesized Increase in Interfacial Permeability 50
Figure 3.4 Photo of DISLASH Multi-Zone Test 52
Figure 4.1 Uniform, Impermeable, Radial DISLASH Test 55
Figure 4.2 Uniform Permeable DISLASH Test 57
Figure 4.3 Uniform Permeable DISLASH Test (Zoomed) 57
Figure 4.4 Measured and Predicted Fracture Radius for Impermeable Test 58
Figure 4.5 Predicted Leakoff Volumes for DISLASH Test 59
Figure 4.6 Fluid and Fracture Front Radius 59
Figure 4.7 Fluid Penetration for DISLASH Test 60
Figure 4.8 Fluid Penetration for DISLASH Test (1-D, 2-D and Experimental) ... 61
Figure 4.9 Multi-Zone Length and Height Growth (Low Contrast) 62
Figure 4.10 Photographs of Multi-Zone Growth (High Contrast) 64
Figure 4.11 Photograph of Multi-Zone Growth (High Contrast) 65
Figure 4.12 Multi-Zone Length and Height Growth (High Contrast) 65

Figure 4.13 Multi-Zone Length and Height Growth (High Contrast)..... 67
Figure 5.1 Simplified Pay-Zone Strata ($k_1 < k_2$)..... 68
Figure 5.2 Waterflood into Strata with High Permeability Contrast..... 69
Figure 5.3 Waterflood with Fracture into Strata with High Permeability Contrast 70
Figure 5.4 Injection and Pressure Gauge Data..... 72
Figure 5.5 DISLASH Multi-Zone Results Matched by Simulator (Scaled)..... 74
Figure 5.6 North Sea Water Injection Well Pressure Match From Simulator..... 74
Figure 5.7 North Sea Water Injection Well Fracture Geometry From Simulator . 75
Figure 5.8 North Sea Water Injection Well Fracture Length and Height From Simulator..... 75
Figure 5.9 North Sea Water Injection Well Fracture Geometry (No Containment) 77
Figure 5.10 North Sea Water Injection Well Fracture Length and Height..... 77
Figure B.1 Field and Lab Parameters..... 93
Figure B.2 Permeability of Unbonded Granular Materials..... 94
Figure B.3 Permeability of Bonded vs. Unbonded Granular Materials..... 95
Figure C.1 DISLASH Rolling Diaphragm..... 97
Figure C.2 Contact Pressure Measurement Plate..... 99
Figure C.3 Schematic of Fluid Under Tester Probe..... 99
Figure C.4 Measured Values of the Contact Stress..... 101
Figure C.5 Map of Contact Stress Over Surface of Big DISLASH Block..... 102
Figure C.6 Map of Contact Stress for Channel Geometry in Little DISLASH.. 103
Figure D.1 Comparison of Old and New Data Acquisition Data..... 105
Figure D.2 Big DISLASH Side View..... 107
Figure D.3 Big DISLASH System Schematic..... 108
Figure D.4 Little DISLASH System Schematic..... 109
Figure E.1 Axial Compressive Permeameter Configured for Granular Sample.. 111
Figure E.2 Axial Permeabilities of Several Foams..... 112
Figure E.3 Transverse Compressive Permeameter (COSPERT)..... 113
Figure E.4 Transverse Permeabilities for Several Foams..... 114
Figure E.5 Axial and Transverse Permeabilities for Bonded Granular Samples.. 115
Figure G.1 DISLASH Simulation of Fracture Growth ($k_2 > k_1$)..... 121

LIST OF TABLES

Table Page
Table 5.1 Relevant FRACPRO Permeability Contrast Coefficients. 73
Table B.1 DISLASH Material Parameters 91
Table B.2 DISLASH Fluid Parameters 92
Table B.3 DISLASH Flow Rates 92
Table F.1 Variables Used For Dimensional Scaling 116

NOMENCLATURE

Dimensions: m=mass, L=length, t=time.

A	Area through which fluid flows in Darcy law equation	(L^2)
α	Empirical structural permeability parameter	(-)
b	Gap thickness	(L)
β	Relative channel thickness	(-)
δ	Fracture opening	(L)
δ_{eff}	Effective fracture opening (incorporating flow parallel to walls)	(L)
E	Young's modulus of elasticity	(m/Lt^2)
$\bar{E}$	Crack opening modulus $= E/4(1-\nu^2)$	(m/Lt^2)
ε	1-D Efficiency	(-)
ϕ	Porosity	(-)
g	Acceleration of gravity	(L/t^2)
Γ	Separation Energy	(m/t^2)
γ_1	Gamma factor for crack opening	(-)
γ_{12}	Gamma factor for lateral stress gradient	(-)
γ_{13}	Gamma factor for lateral cross-sectional area	(-)
γ_{14}	Gamma factor for lateral channel flow	(-)
γ_v	Gamma factor for fracture volume	(-)
γ_P^F	Pore pressure influence function	(m/L^3t^2)
h	Thickness of permeability sample	(L)
$\dot{\gamma}$	Shear strain-rate	(t^{-1})
K	Consistency index	(m/Lt)
K_I	Mode I stress intensity factor	$(m/L^{½}t^2)$
K_{IC}	Critical value of K_I at which crack propagation occurs	$(m/L^{½}t^2)$
K_{Icyl}	Stress intensity factor for a penny shaped crack in an cylinder	$(m/L^{½}t^2)$
$K_{I\infty}$	Stress intensity factor for a penny shaped crack in an infinite medium	$(m/L^{½}t^2)$
K_ℓ	Leak-off coefficient	$(L/t^{½})$
k	Permeability	(L^2)
k_1	Originating permeability	(L^2)
k_2	Approaching permeability	(L^2)
k_{axial}	Axial permeability	(L^2)
$k_{trans.}$	Transverse permeability	(L^2)
ℓ_1, ℓ_2	Lengths of the left and right fracture wings	(L)
μ	Viscosity	(m/Lt)
μ	Effective channel-flow viscosity	(m/Lt)

$\tilde{\mu}$	Effective leakoff viscosity	(m/Lt)
υ	Kinematic viscosity	(L^2/t)
ν	Poisson ratio	(-)
n	Flow behavior index	(-)
p_F	Fluid pressure	(m/Lt^2)
p_P	Pore pressure	(m/Lt^2)
P_w	Driving pressure for permeability testing	(m/Lt^2)
p	Excess pressure $p = P_F - \sigma_c$	(m/Lt^2)
Δp	Reservoir pressure difference $(P_F - P_P)$	(m/Lt^2)
Q	Injection rate	(L^3/t)
Q_{FC}	Flow rate for full crack assumption	(L^3/t)
Q_{HC}	Flow rate for half crack assumption	(L^3/t)
Q_L	Leakoff flow rate perpendicular to fracture face	(L^3/t)
$Q_{\parallel}$	Flow rate parallel to the fracture face	(L^3/t)
q'	Flow rate into the fracture tip, (per unit depth)	(L^2/t)
R	Radius of penny shaped fracture	(L)
R_{cyl}	Radius of cylindrical Silastic block	(L)
R_w	Wellbore radius	(L)
r_i , r_o	Preflood zone inner and outer radii	(L)
R_i , R_o	Permeability sample internal and external radii	(L)
ρ	Fluid density	(m/L^3)
σ_c	Confining stress	(m/Lt2)
$\sigma_{contact}$	Contact stress	(m/Lt^2)
σ^*	Characteristic pressure	(m/Lt^2)
t	Model time	(t)
t_h	Characteristic 'holding' time	(t)
τ	Shear stress	(m/Lt^2)
τ^*	Characteristic time for impermeable constant injection rate	(t)
τ_h^*	Characteristic holding time for constant injection rate	(t)
V_F	Volume of fluid in fracture	(L^3)
V_L	Volume of fluid leaked from fracture	(L^3)
V_T	Total volume of fluid pumped into fracture	(L^3)
v	Velocity of fluid in fracture	(L/t)
v_p	Velocity of fluid in permeable fracture walls	(L/t)
W	Weight of Silastic block	(mL/t)
ω	Length of the non-penetrated zone	(L)
x_L	Fluid Leakoff penetration depth	(L)

CHAPTER 1

INTRODUCTION AND BACKGROUND

1.1 Hydraulic Fracture Propagation

In simplest terms, hydraulic fracturing, or "hydrafrac," is a technique commonly used to fracture rocks surrounding existing underground wells in order to allow fluids (usually oil or gas) to flow more readily to the wellbore. In practice, the technology involves pumping fluid into the well at pressures sufficient to overcome the existing underground pressures, thereby fracturing the rock, and creating openings wide enough to allow a proppant to be carried into the fracture. The proppant then serves to hold the fracture open after the fluid pressure is removed. The fracture is aligned approximately perpendicular to the direction of least stress: for most underground conditions, in tectonically relaxed areas with horizontal least stresses, the fracture should be vertical. [1]

Hydraulic fracturing is a widely used method of increasing the productivity of oil and natural gas wells. In the forty years since hydrafrac was introduced into the industry [2] more than a million wells have employed the technology [3]; about half of all wells drilled today use hydraulic fracturing [4]. As the demand for oil and natural gas increases and producing companies are forced to investigate less efficient geological areas with lower rock permeability, hydrafrac technology is increasingly in demand to aid in making petroleum extraction conditions more favorable. In order to create economically optimal fracture conditions, detailed modeling of the geological structure

and fracturing process is necessary to provide insight into the proper pressures, flow rates, and pumping volumes.

A typical field hydraulic fracture situation is shown in Figure 1.1. Hydrafrac is a demanding application that involves pumping large quantities of fluids and can require significant capital investment; as a result, accurate modeling of the process is required for best economic return. Stratified reservoirs complicate the modeling of the fracturing process; although many researchers have attempted to model this process, their results ignore a variety of mechanisms. A major deficiency has been the effect on growth of different leakoff in each stratum, (i.e. permeability barriers to growth and fracture holding time). This study deals with the process of fracture growth in permeable, stratified media.

This study is important for several reasons. Primarily, the resource recovery process is very capital intensive. The cost of drilling and fracturing a well can run into the millions of dollars and the return on the investment must be significant. This is where modeling of the underlying physics becomes important: if the process can be properly understood, then treatments can be designed that take advantage of the natural formations to produce fractures and place (enough) proppant in the area of interest, to enhance the recovery potential of the oil or natural gas reservoirs.

Also important is the need to improve the petroleum recovery process, directly and indirectly. Waterflooding, is an enhanced recovery technique for driving out more of the original oil in place. Such flooding involves injecting fluids via one or more wells into the reservoir to help displace the oil which is produced via one or more other wells. [5-7] Because of large capital investments, or for reasons discussed later, higher injection rates are desired, the waterflooding process may produce pressures above the parting pressure, thereby generating fractures (e.g. Ref. [6,8]). Understanding of the mechanisms and

proper modeling of the fracturing process is essential for determining the best recovery techniques possible.

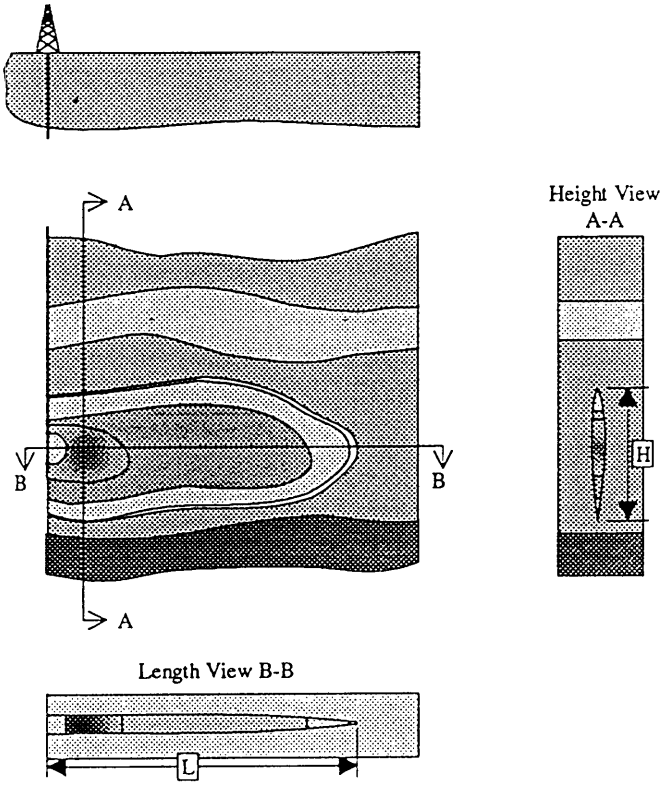

Figure 1.1 Typical Field Hydraulic Fracture

1.2 Permeability Issues

1.2.1 Fluid Loss

The fluid loss in hydraulic fractures has been shown to significantly affect the fracture growth. The effect of permeability on the growth of internally pressurized fractures has been investigated in theoretical and experimental efforts. [9-11] The range of common field values for permeability (as well as other parameters), can be found in Appendix B. Typical permeabilities range from less than 1 μDarcy (air) for shaly rock to a Darcy (defined as 10^{-8} cm^2) or more for sandstones.

1.2.2 Efficiency

The impact of permeability* on a hydraulically driven fracture is significant and has been studied extensively. The permeability of the surrounding material is often one of the principal determining factors for the pressures opening the fracture, and the fluid volume in the crack. Previous researchers [11-13] used a term called 'efficiency', ε, defined as the volume of fluid in the fracture divided by the total volume of fluid pumped as shown in Equation (1.1). Or similarly, the total pumped, minus the volume leaked off, divided by the total volume.

$$\varepsilon = \frac{V_F}{V_T} = \frac{V_T - V_L}{V_T} \tag{1.1}$$

1.3 Dimensional Scaling

The scale and expense of hydraulic fracture operations prevents full scale testing of field situations, while field conditions greatly complicate acquisition of many values. Most importantly, the dimensions of an underground fracture cannot be measured directly as they can in a laboratory environment.

1.3.1 Requirements

Scale testing requires *geometric* and *dynamic* similarity. Geometric similarity requires that the model and the field case must be identical in geometry except for size. The more complex requirement involves dynamic similarity where the forces, or flows, are determined which must be used in the laboratory in order to correspond to realistic field situations. The actual non-dimensionalized groups used for this work are presented in Chapter 3 and Appendix F.

---

* A description of permeability and relevant issues is given in Appendix B. Appendix E contains descriptions of the permeability tests done for this work.

1.4 Previous work

The bulk of previous work investigating permeable hydraulic fractures, especially permeability barriers, has been purely analytical, focusing on numerical simulation. The few experimental simulations performed have had significant shortcomings and will be discussed below.

1.4.1 Analytical

Analytical modeling of fracturing in permeable media is developed or summarized in Refs. [10,12,14-24]. The model that is most practically useful and applies to the conditions investigated in this work is presented in Ref. [10] with clarifications for proposed experimental verification in Ref. [19]. These models represent the fluid flow as a completely one-dimensional flow field away from the fracture into the permeable media. Although two-dimensional contributions are considered in Ref. [10] the complexities involved with combining the near-tip behavior were considered too detailed for the low permeability conditions under immediate investigation.

1.4.1.1 1-D Approximations

Leakoff in hydraulically driven fractures has typically been modeled using a one-dimensional approximation where fluid leakoff occurs uniformly normal to the face of the fracture producing a flooded zone similar to Figure 1.2 below.

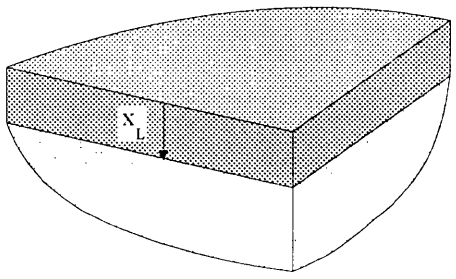

Figure 1.2 Fluid Penetration (Dry Medium)
The pure 1-D model assumes that the fluid leaks from the fracture in a direction perpendicular to the fracture face producing a flooded region of length x_L into both faces of the fracture. This idealized figure shows the leakoff depth into a semi-infinite region. The leakoff depth is represented as a uniform thickness along the plane of the fracture as shown above.

Several general models for 2-D planar fractures have been developed e.g. Refs. [10,22,25,26]. The bulk of these models are based on leakoff penetration depths which, in comparison to the scale of the fracture length can be analyzed using 1-D analysis.* The main features of the Crockett and Cleary models are demonstrated in Figure 1.3. The fluid flow and thermal penetration are modeled as one-dimensional zones bordering the fracture. To simplify the description, the thermal and filter cake effects will be neglected, to better focus the scope of this research. The fluid flow into a two fluid reservoir† is modeled as Darcy flow, and the flux rate can be written as:

$$q_L = \frac{2k(p_F - p_P)}{\mu x_L} \tag{1.2}$$

where the penetration distance of the fracture fluid, x_L is given by the following:

$$x_L(x_o,t) = \frac{1}{2\phi}\int_0^t q_L(x_o,\tau)d\tau \tag{1.3}$$

$$p_F(x_o,t) - p_P - \frac{1}{2}\left(\frac{\mu}{k}\right)x_L(x_o,t)q_L(x_o,t) = \int_o^t d\tau \int_{-\ell_1}^{+\ell_2} q_L(x,\tau)\gamma_P^F dx \tag{1.4}$$

where γ_P^F is the pore pressure influence (Green's) function for a line source parallel to the z-axis (wellbore in this example) which is fully described in Ref. [25], the fracture extends from $-\ell_1$ to $+\ell_2$, and the pressure is assumed known and constant along the length of the fractures.

---

* The scale of pressure penetration in a gas reservoir is typically of order 1 m and in a oil reservoir of order 10 - 100 m. These may be small compared to typical fracture lengths of order 100 m (except, perhaps, in oil reservoirs).

† The experimental fracture simulation discussed here is an idealized description of a gas reservoir where the viscosity of the reservoir pore fluid is negligible compared to the viscosity of the fracturing fluid.

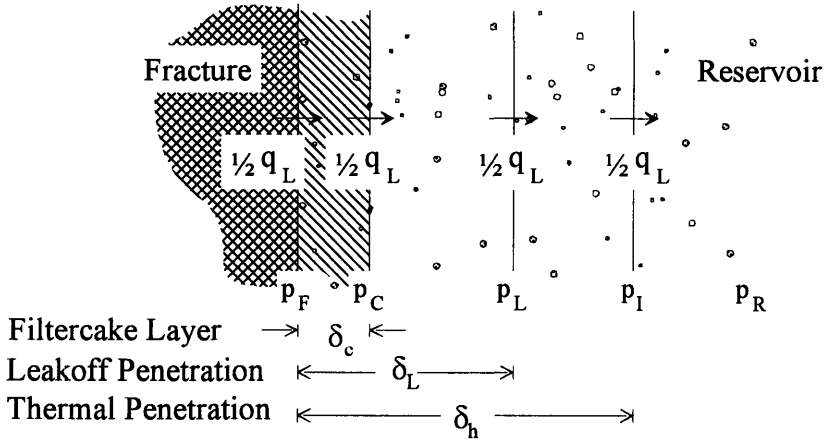

Figure 1.3 One-Dimensional Zones of Leakoff and Thermal Penetration

The focus of this model is to identify the key parameters and define the flows induced in the reservoir near the fracture, using a one-dimensional approximation.

1.4.1.2 Numerical Models

The complex situations involved in hydraulic fracture have prompted the development of numerous simulators incorporating the models discussed above. Two of the available simulators are discussed below. A discussion of the available simulators can be found in Ref. [27]. A wide variety of simulators are used by the petroleum industry, both of commercial and academic origin; however R3DH and the fracture model in FRACPRO were chosen for use because of their ability to readily match laboratory and field data, and the available literature and support for these systems. [28-32]

While numerical simulators are excellent at extending simplified models to very complicated conditions, the development and verification of new mechanisms is often better performed in the laboratory where hypothesized behavior can be studied. The purpose of the experimental work in this study is to evaluate several hypotheses concerning the role of permeability contrasts.

Although both of the simulators (R3DH and the model in FRACPRO) are capable of modeling many other effects, including proppant convection and dilatancy crack tip behavior, these additional special abilities are either not part of the scope of this work, i.e. not important for experimental conditions in the laboratory.

R3DH

The M.I.T Resource Extraction Laboratory with funding from the Gas Research Institute (GRI) and in cooperation with Resources Engineering Systems, Inc., has incorporated physical and mathematical modeling capabilities into a computer program called R3DH. [28,29] R3DH is a fully 3-D simulator which calculates the relevant fracture parameters over the fracture surface. This computationally-intense program requires computing resources beyond those readily available or desirable for field applications.

FRACPRO

FRACPRO, a field oriented simulation program, uses a "lumped-parameter" 3D fracture model to simulate hydraulic fracture under field conditions, (including real-time analysis). The "lumped parameter" model incorporated in FRACPRO has been developed using the results of actual 3D simulators, such as R3DH, as well as checking the results against previous laboratory simulations and matching of field data: a unique feature of the FRACPRO system is the ability to produce time histories of net fracture pressures which can be compared to experimental work and calibrated to established laboratory results. Fluid loss in the simulator is modeled as dominantly one-dimensional flow perpendicular to the fracture face (e.g. Ref. [22]).

1.4.2 Experimental

The experimental apparatus at the Resource Extraction Laboratory have made significant contributions to the modeling of hydraulic fracture growth [33,34]. The

principal developments have been accomplished using DISLASH (Desktop Interface Separation Laboratory Apparatus for Simulation of Hydraulic Fracture) and related laboratory systems.

1.4.2.1 DISLASH

The DISLASH system consists of a low modulus, Silastic rubber block pressed against a comparatively rigid, clear PMMA block shown below in Figure 1.3. DISLASH models the separation of the (rock) faces in fracture growth by forcing a viscous silicon-based fluid into the interface between the pliant rubber block (or low modulus permeable material) and the comparatively rigid PMMA block to simulate **half** of a fractured body. Although there is no breaking or fracturing of material, the separation of the interface will be referred to as a *fracture* for simplicity. Fracture toughness in DISLASH is almost zero which is practically equivalent to field conditions [35]; the only bonding arises from surface tension effects and static electricity between the block and the PMMA, both of which are insignificant compared to the pressures encountered in testing.

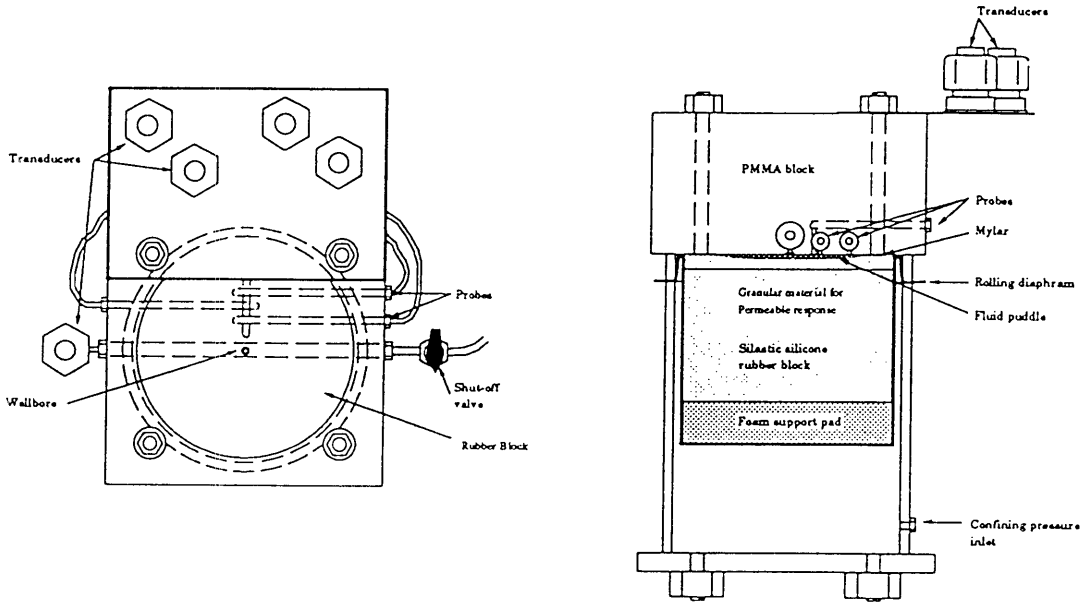

Figure 1.4 Side and Top Views of Smaller DISLASH

This laboratory apparatus was designed to simulate equivalent toughness as close as possible to zero, both for repeatability and because rock toughness has been shown to play a negligible role in field fracturing operations [35]. DISLASH, shown in Figure 1.4 and Appendix D, is the latest version of this experimental approach to modeling hydrafrac. The apparatus has several important features; experiments may be carried out very quickly, lasting less than two minutes in most cases, and fracture growth can be measured visually. Additionally, there is virtually no down-time between tests, because the separation of the interfaces is non-destructive.

When analyzing DISLASH data, it is important to realize that the fracture opening is half the width of an equivalent fracture. To account for the half-crack nature of DISLASH, the equations are simply modified by doubling the crack opening modulus [34]. Although this modification is not exact, it is adequate, in general, certainly for the present study of permeability barriers; it is also consistent with the inherent accuracy of the practically oriented lumped-model analysis Aside from the half-crack modification, DISLASH results can be scaled directly using the relations discussed in Appendix F.

1.4.2.2 Foam

Previous researchers [11-13] have attempted to model permeable conditions using a variety of foam materials. Although the conditions for properly scaling the permeable leakoff had been considered [19], the physical implementation failed to consider possible anisotropic behavior of the foam material. Johnson [11,12] used a Scott felted foam which is formed by taking a normal open-celled foam and compressing it to one tenth to one twentieth of its original height. By compressing the foam, the cells are 'flattened' producing a non-isotropic permeability, further accentuated by the uniaxial compression of the foam pads in DISLASH.

The felted foams suffered from several important complications. The felting process produces transverse permeabilities that are two orders of magnitude greater than

axial permeability as shown in Figure 1.5. The permeabilities were determined using a newly developed experimental apparatus described in Appendix E. These permeameters possess the unique ability to compress the sample with the confining stresses (σ_c) that would be encountered in DISLASH tests. As evident from the Figure, the permeability of the foams is dependent on the confining stress applied.

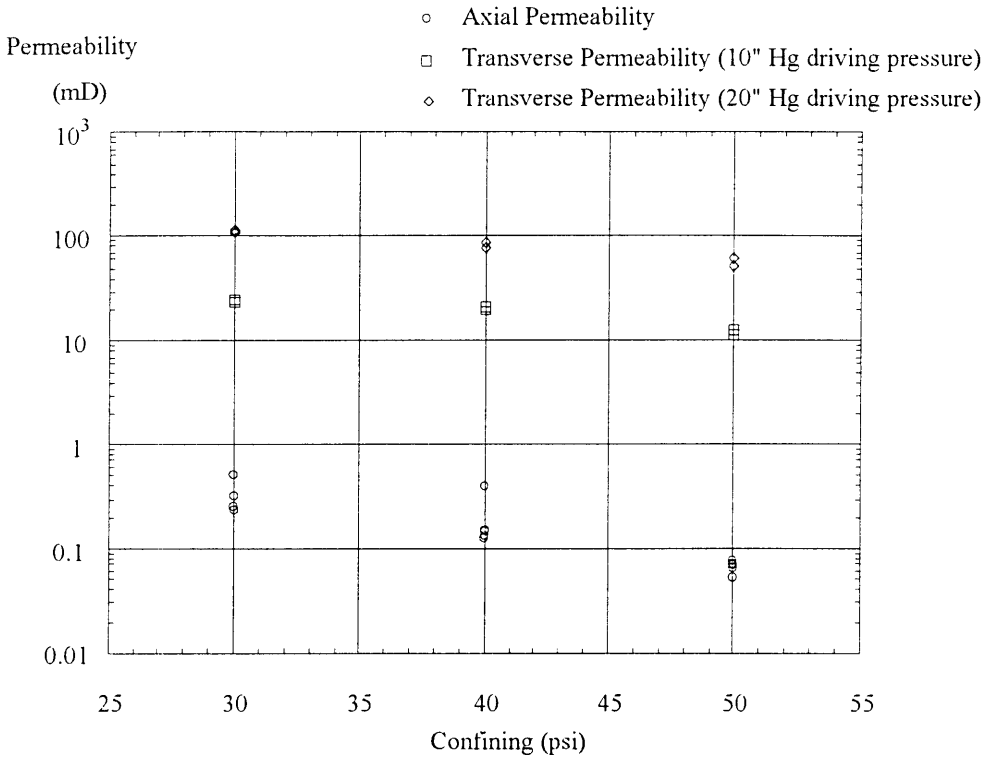

Figure 1.5 Axial and Transverse Permeabilities of Scott Felted Foam.

The foams also exhibit an increase in measured permeability with higher driving pressure. The exact origin of these behaviors has been theorized as due to the nature of the cell openings: a hypothetical situation is shown in Figure 1.6. Although this behavior is interesting, and has been cursorily examined (only in the axial case) by other researchers [36,37], the foams do not accurately model the relatively isotropic permeability conditions of most petroleum reservoirs of primary interest in this work.

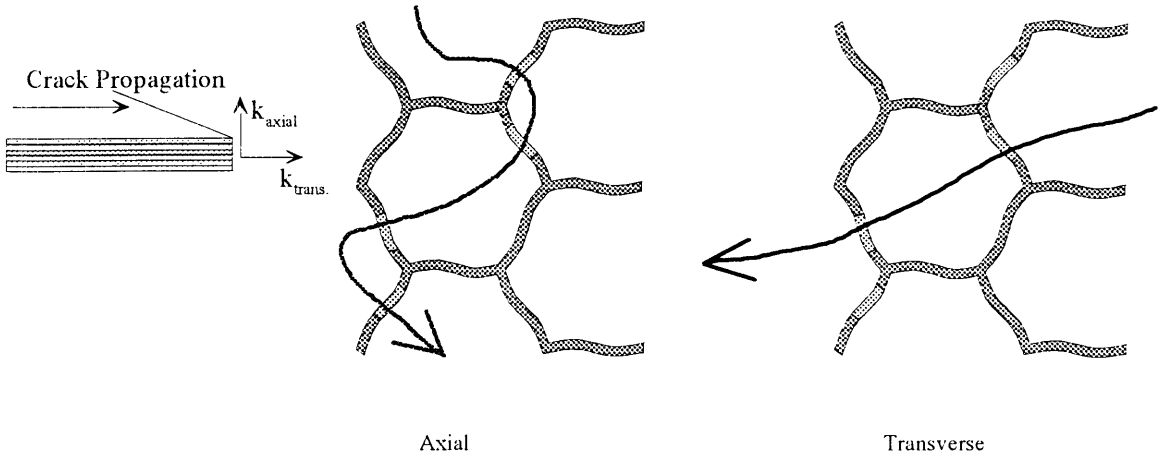

Figure 1.6 Hypothetical Foam Schematic

The two streamlines shown represent flow in the axial and transverse directions, the location of the cell openings may require a much more tortuous flow path in the axial direction shown on the left than flow in the transverse direction shown on the right.

Although the foam does not represent the isotropic case, the larger transverse permeability can be useful for examining modeling conditions. In DISLASH the transverse direction is along the crack propagation direction and would accentuate flow through the permeable material in that direction; for instance, the resulting behavior would accentuates the existence of the preflood zone in front of the actual fracture; where the preflood zone is defined as the region in front of the opened fracture which is saturated with fluid leaking from the pressurized fracture.

Felted foams also required extensive preparation to remove a heat-affected top layer with a fly-cutter. This process was not only time consuming, but produced an uneven surface for mating with the PMMA block in DISLASH. To produce similar permeability conditions without the time consuming sample preparation times, non-felted foams were examined. By properly selecting the material, the transverse anisotropy was reduced, and the dependence of permeability on over-pressure was reduced, as shown in Figure 1.7.

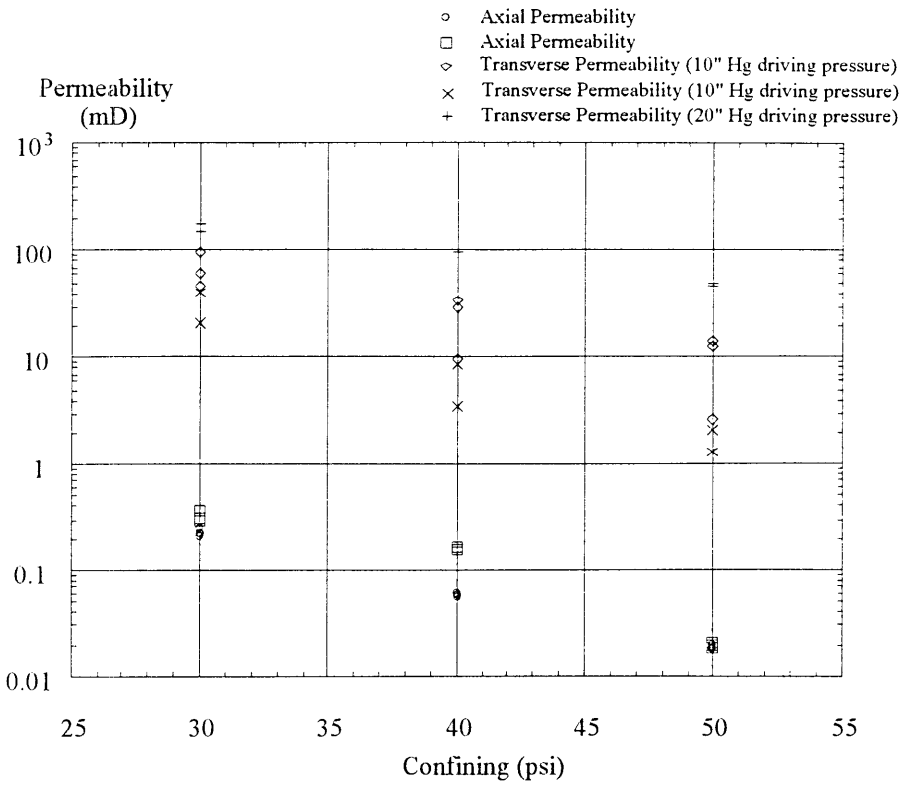

Figure 1.7 Axial and Transverse Permeabilities of Gray Foam

1.4.2.3 Growth Regimes

The important contribution of foam studies is the identification of growth regimes, (first noted, but not quantified in Ref. [13]): as fluid is pumped into the PMMA - permeable material interface, the fluid must first saturate the permeable material at least to the extent that the pressure required to push more fluid into the material exceeds the confining stress, at which time, the fracture will initiate and propagate. The fracture will remain open at any point only as long as the pressure remains above the confining stress and enough fluid is supplied to that point.

The fluid penetrating ahead of the crack, resulting in *pre-flooding*, was first noted in foam materials due to the larger transverse permeability that accentuates this behavior, although all permeable materials will exhibit this behavior to some extent.

1.5 Current studies

1.5.1 Identification of Problem Addressing

The purpose of this work is to determine the degree to which permeability contrasts can influence fracture propagation under hydraulic fracture conditions.

1.5.1.1 Multiple Permeability Zone Fractures

Typical field conditions involve fracturing into complicated strata which have varying material properties; such properties include material modulus, fracture toughness, permeability, and porosity, as well as varying levels of confining stress. Figure 1.8 shows a typical configuration in which the material and stratification profile determine the confining stresses and permeabilities. For modeling simplicity in this thesis, the case of step changes in permeability is being considered independent of other material or stress changes. This modeling assumption serves to isolate the effects of permeability barriers. The decision to vary only permeability significantly complicates the experimental requirements. The resulting solution is discussed in Chapter 3.

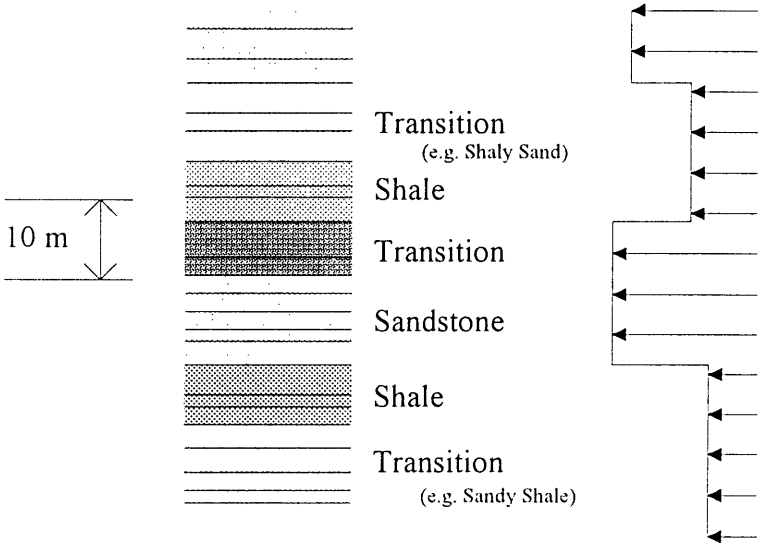

Figure 1.8 Typical Field Strata with Varying Confining Stress
Figure adapted from Ref. [38]

1.5.1.2 Laboratory Scale

The large scale of field conditions requires the use of dimensional scaling for accurate laboratory reproduction of conditions. Laboratory scale apparatus have been specially modified to simulate permeable leakoff in short term experiments. These improvements have made use of innovative materials and practices that overcome the shortcomings of previous configurations and will be discussed in Chapter 3.

1.5.2 Contribution

Although numerous simulators have been developed to model the hydraulic fracture process, few, are capable of matching field data over a wide range of conditions without unrealistic changes in reservoir parameters [27,34,39]. Simulating fracture conditions in the controlled environment of the laboratory will enable the development and verification of models that can later be implemented in simulators that are able to superimpose the results discussed in this work onto the complex reservoir conditions found in the field [40].

1.5.2.3 Experimental Analysis

The proposed method uses dimensional scaling to model the dominant processes in laboratory scale apparatus. The physical laws which govern fracture propagation through permeable media, as well as the development of the theoretical models used to scale the experiments, will be discussed. Although previous researchers [10-13,19,41-44] have attempted to model fracture in permeable materials, this work is the first to examine and properly implement (through dimensional scaling and isotropic permeability) the flow conditions in the permeable material in the laboratory.

The improvements in DISLASH and the supporting apparatus developed for this project have further verified the validity of the interface separation technique. The technological improvement in the data acquisition system and other components is

discussed fully in Appendix D. These improvements have permitted testing over a much wider range of conditions with greater confidence in the experimental findings.

1.5.2.4 Quantify Permeability Barrier "Strength"

The results of the experimental studies will be presented in their original form and in non-dimensionalized summaries which, when compared with relevant field situations, can be used to aid in the understanding of the influences of permeability stratification in hydraulic fracture in the field.

The principal characterization factor related to permeability barriers is the *holding time*, or the amount of time a propagating fracture is detained at the interface between two different permeability zones. Theoretical and experimental values are compared in Chapter 4. Numerous experimental investigations were performed and the results will be compared to numerical modeling software in Chapter 5. By properly understanding the effect of permeability barriers to fracture propagation it will be possible to better predict the behavior of fracture growth in stratified field conditions, leading to increased economic return and enhanced recovery of resources.

1.6 Overview

Following this introduction, the basic elements of the analytical modeling will be discussed in relation to the experimental model and observations. The experimental simulation will then be discussed with particular emphasis placed on the dimensional scaling required for proper modeling of field conditions. The material development will also be discussed in relation to the limitations of the model development and experimental apparatus. Methods of testing and data reduction are included Chapter 3 to clarify the strengths and limitations of the techniques used.

Chapter 4 will include the results from extensive testing over a wide range of conditions with significant reduction of the data into combined, non-dimensionalized plots. The extension of the laboratory results to field conditions will be examined in

Chapter 5 with major emphasis on the available data from a Statoil (Norway) well in a high permeability contrast strata.

The conclusions of this research are detailed in Chapter 6. The various appendices also include significant insights into the development of the analytical and experimental models, and additional observations (e.g. Inverse Permeability Barriers in Appendix G) which, although they did not fit into the immediate scope of this work, are included to detail this and other important mechanisms.

CHAPTER 2

DEVELOPMENT OF MODEL

2.1 Assumptions

Modeling a process as complex as hydraulic fracture requires simplifying assumptions. The first simplification assumes dominant linear elasticity in the fracture opening. This assumption has been verified for numerous situations under a wide range of conditions, most recently in Refs. [39,45]. DISLASH is a purely elastic simulator, and as such, is incapable of producing inelastic effects. While inelastic effects, such as crack tip dilatancy, seem to affect fracture propagation in rock-like materials at sufficient depth [33,40,45], those effects are not included in this study. An additional modeling assumption is the negligible effect of fracture toughness. For large-scale hydraulic fractures, of radius R, the energy required for opening a fracture per unit opening is shown in Equation (2.1a), where the excess pressure is defined as the fluid pressure minus the confining pressure, ($p = p_F - \sigma_c$), while the energy required for fracturing the perimeter is shown in Equation (2.1b). Typical values for the crack opening modulus, $\bar{E}$, and fracture toughness, K_{IC}, can be found in Appendix B. The ratio of opening to fracturing energy, shown in (2.1c), representing the ratio of opening to fracture energy, demonstrates that fracture toughness is negligible.

$$O(p_F \cdot \delta) \approx p_F \cdot \frac{pR}{\bar{E}} \tag{2.1a}$$

$$O\left(\frac{K_{IC}^2}{\bar{E}}\right) \tag{2.1b}$$

$$Ratio = O\left(\frac{p_F\, p\, R}{K_{IC}^2}\right) \approx 10000 \qquad (2.1c)$$

Although important in field applications, thermal effects are also considered negligible in this work. The fluids used in the laboratory are very thermally stable and the models can be adapted for the thermal changes in viscosity for field situations. Uniform, Newtonian fluids are also assumed for all of the analytical modeling to reduce the complexity of the equations used to demonstrate the model physics. More complex fluids are typically used in the field in hopes of increasing performance under the varying thermal conditions encountered underground.

The assumption of a uniform fluid in the fracture, which is also not necessarily valid for most field cases, is required for the following model which assumes single phase, single viscosity flow invading the permeable material near the fracture. Although these assumptions may represent some departure from field conditions, the necessary simplifications will disassociate the role of permeability barriers from the other effects which would confuse the issue being examined. The other complexities of behavior can then be handled with a more general simulator such as the default model in FRACPRO discussed in Chapter 1. The additional assumptions which have been required in the development of the laboratory simulation will be addressed in Chapter 3.

The scope of this work deals with situations where the permeability in which the fracture originates is greater than or equal to the permeability which the fracture approaches ($k_1 \leq k_2$). Situations where this does not apply are discussed in Appendix G.

Low permeability situations have been studied extensively, e.g. refs. [10,25,26,28], and the laboratory evidence supports the findings. Several researchers have developed simulators that model fracture growth, except for high permeability and / or, slow fracture propagation [28]. High permeability situations, however, are outside the realm

typically considered when modeling hydraulic fractures, especially due to the two-dimensional leakoff near the tip of the fracture.

2.2 Leakoff Models

To illustrate the nature of permeability barriers, the leakoff of fluid from a hydraulically-driven fracture as it approaches a high permeability zone is presented in Figure 2.1: the fracture approaches the interface and propagates into the second region; the area of interest is shown in Figure 2.2. The three diagrams represent the same fracture sequentially in time.

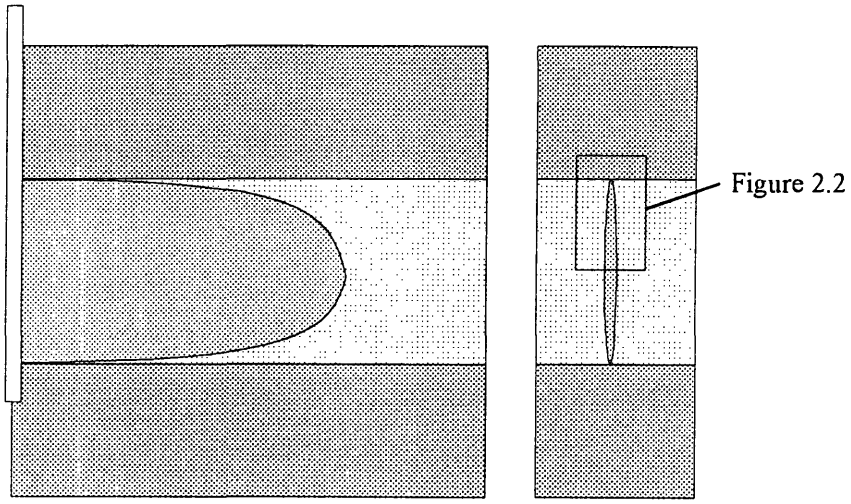

Figure 2.1 Hydraulic Fracture Approaching High Permeability Zone

The depth of the fluid penetration into the surrounding material is typically small relative to the overall fracture length (during the treatment time); this implies that it is sufficient to assume one-dimensional fluid loss normal to the fracture. However, near the fracture tip, the scale of the leakoff is of the order of the distance from the perimeter, necessitating a two-dimensional representation of the fluid flow leaking off through the fracture tip and the fracture walls.

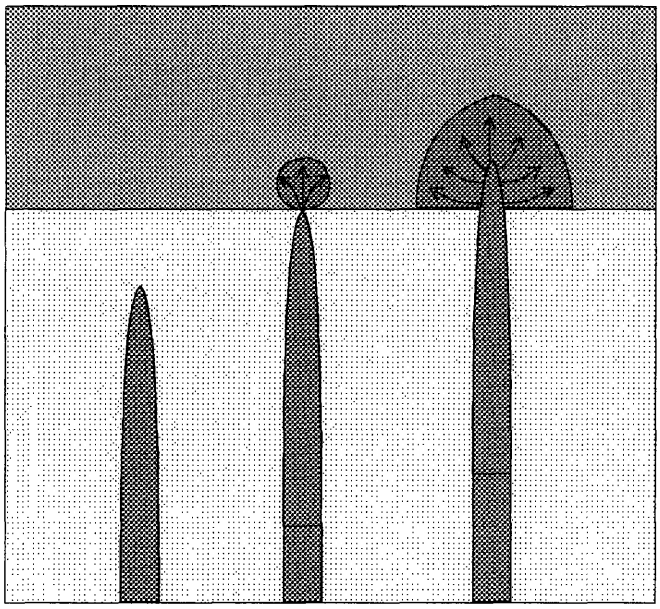

Figure 2.2 Hydraulic Fracture Approaching High Permeability Zone (3 Views) As the fracture approaches the interface the fluid first begins to leak through the fracture tip, preflooding the region directly in front of the fracture. When a sufficiently large pre-flood zone is established, the fracture will begin propagating into the higher permeability zone. (In the above figure, the material on the bottom is represented as impermeable, or of extremely low permeability relative to the material on the top to better illustrate the behavior associated with permeability barriers.)

2.2.1 One-Dimensional Leakoff

The fluid loss through the walls of the main body of fracture is modeled as planar with uniform pore pressure, p_p, along the length of the fracture, similar to Figure 2.3. To provide estimates of the volume of the fluid lost from the fracture, uniform pressure distribution along the fracture length is generally assumed, which is approximately valid except near the tip where large pressure gradients are present, as shown in Figure 2.4. For quasi-static fracture propagation the fluid pressure in the crack is balanced by the fracture toughness of the material and, for relatively impermeable conditions, the confining stress acting over a small region near the tip called the non-penetrated zone. In impermeable conditions, the fluid would have to undergo a near infinite pressure gradient to be forced into the fracture tip which is uncharacteristic of the quasi-static growth

encountered in the lab and in the field. The non-penetrated zone length, ω, is typically small in relation to the length of the fracture but can and has been observed in the laboratory. [11,45] In higher permeability reservoirs the fluid near the tip of the fracture is not constrained by no-slip conditions at the fracture walls and pressure gradients near the tip become dominated by Darcy law flow instead of wall shear. The fluid can then leak through the tip of the fracture, producing a preflooded zone ahead of the fracture instead a non-penetrated zone behind the fracture tip.

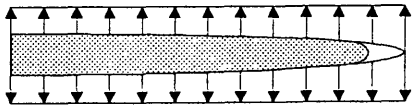

Figure 2.3 One -Dimensional Leakoff Model
Note the absence of leakoff through the tip, parallel to the fracture. This figure represents the same vertical fracture as Figures 2.2 and 2.3, with the axis rotated 90° to simplify the representation of leakoff.

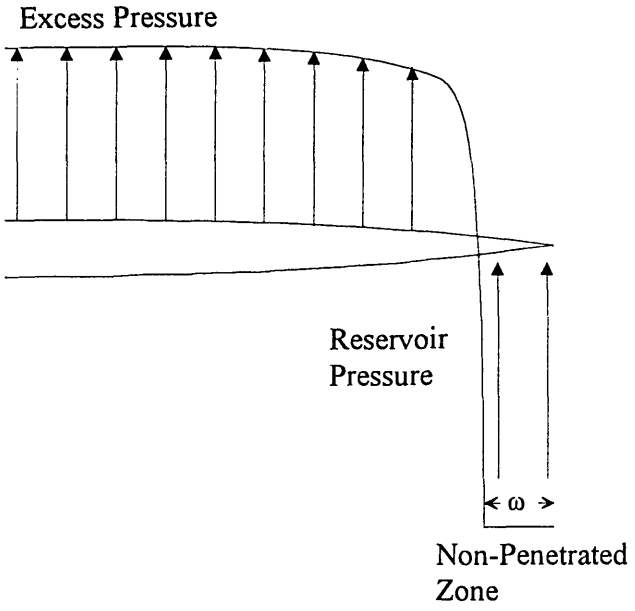

Figure 2.4 Pressure Distribution Along Fracture

2.2.2 Near-Tip Leakoff Behavior

Examining the crack-tip, as shown in Figure 2.5, it is possible to write a simple statement of mass conservation for a crack that is almost stationary, (assuming an incompressible fluid for simplicity):

$$\phi \pi \left(r_o^2 - r_i^2\right) = 2\int_0^t q' \, dt \tag{2.2}$$

in which ϕ is porosity and q', is the volume flux into the near-tip region. The inner radius r_i may be considered negligible by comparison to r_o, but is extremely important in determining the 'holding time'; for an impermeable medium ($k_1 = 0$), all of the flux, q',must pass through the aperture δ_{eff}, which is controlled by r_i as follows:

$$\delta_{eff} \approx g_1 r_i \frac{(p_F - \sigma_c)}{\bar{E}} \tag{2.3}$$

in which g_1 is a geometric function which can be calculated with the relevant simulator, most comprehensively handled in Ref. [28].

The system of equations can now be closed by calculating the leak-off behavior in the region shown in Figure 2.5. To do this we specialize the vector form of Darcy's law to radial flow and assume isotropic permeability to approximate the leak-off pressure near the crack tip as a function of the flooded zone depth, namely.

$$\mu \frac{Q}{A} = -k \nabla p_F \tag{2.4}$$

leads to a simple pressure distribution:

$$p_F(r) = p_P + \frac{\mu q'}{\pi k} \ln\left(\frac{r_o}{r_i}\right) \tag{2.5}$$

The flux is then determined as follows:

$$q' = g_2 \left(\frac{\delta_{eff}^3}{\bar{\mu}}\right) \frac{(p_F - \sigma_c)}{r_i} \tag{2.6}$$

where the geometric function g_2 can be determined also with a simulator [28].

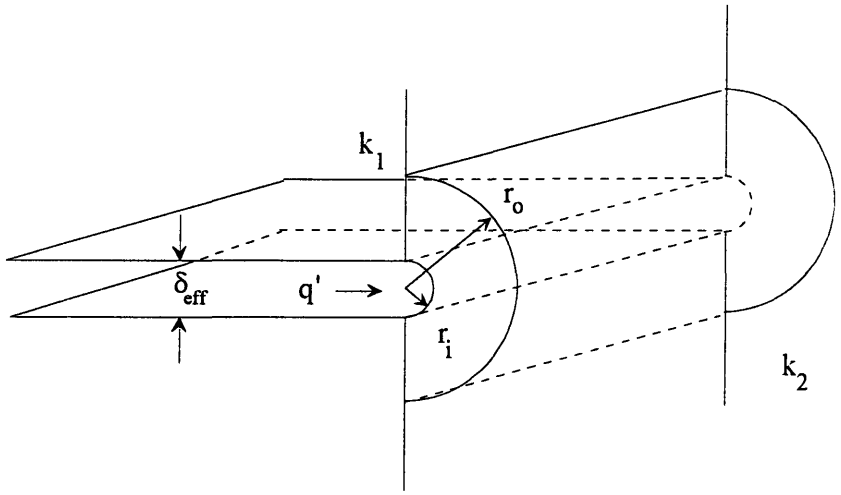

Figure 2.5 Leakoff Through Fracture Tip

A solution to Equations (2.2) - (2.6) can be obtained as follows:

$$r_i^2 \approx k' \exp\left(\frac{2t}{\tau_c}\right) \tag{2.7}$$

from which the characteristic time can be extracted in the following phenomenological form (for negligible permeability k_1):

$$\tau_c \approx \frac{\phi\pi}{g_1^3 g_2} \frac{\bar{\mu}\bar{E}^3}{(p_F - \sigma_c)^4} \exp\left[\frac{k}{k'}\frac{2\pi}{e^2}\frac{(\sigma_c - p_P)\bar{\mu}\bar{E}^3}{\mu g_1^3 g_2 (p_F - \sigma_c)^4}\right] \tag{2.8}$$

For non-negligible k_1, we may require two-dimensional modeling; to appreciate this, it is useful to compare fluid velocities in the permeable material to velocities in the fracture. Comparing flow parallel to the fracture faces in the two regions would signify the relative contributions of each mechanism [28]. Flow velocity through the permeable material, shown in Equation (2.9) incorporated into the ratio of velocity in the crack, under similar pressure gradient, in Equation (2.10) produces the right hand side dimensionless number, assuming a common fluid pressure gradient. For ratio values much less than one, the crack flow dominates and one-dimensional models would model the predominant behavior.

$$v_\ell = -\frac{k}{\mu}\frac{\partial p}{\partial r} \tag{2.9}$$

$$\frac{v_\ell}{v_c} = \frac{-\frac{k}{\mu}\frac{\partial p}{\partial r}}{-\frac{\delta^2}{\overline{\mu}}\frac{\partial p}{\partial r}} = \left.\frac{\overline{\mu}k}{\mu\delta^2}\right|_{\substack{\text{Common} \\ \text{Pressure Gradient}}} \tag{2.10}$$

The above number assumes a common fluid pressure gradient. For regions far from the crack tip the ratio is of order 10^{-7} and 10^{-8} for field and lab conditions respectively in a low permeability of order 10^{-1} mD. For higher permeabilities the ratio is increased to 10^{-5} and 10^{-4} for field and lab conditions far from the crack tip. When the region near the fracture tip is investigated and the dominant length scale decreases, the above ratio reaches values of order one and the fluid flow parallel to the crack can no longer be neglected.

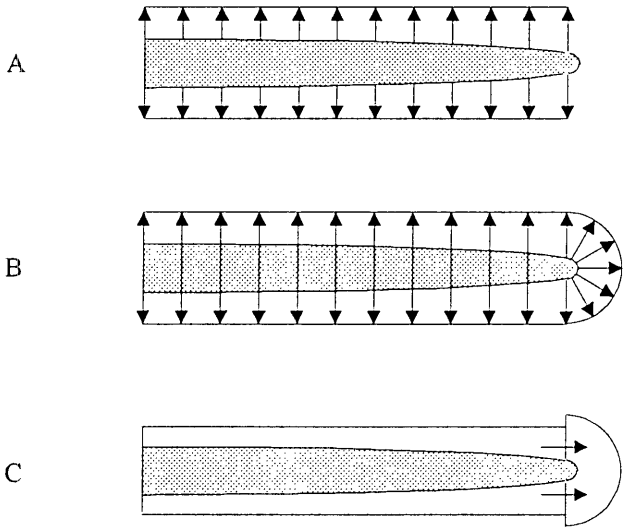

Figure 2.6 Two-Dimensional Leakoff Models
Sub-figures A, B, and C represent the three components of fluid loss through the fracture. While sub-figure A idealizes fluid leakoff though the fracture walls, B and C more accurately represent the contributions to flow through the fracture tip.

By modeling the quasi-static fracturing progression as a piece-wise continuous time-space behavior, it is possible to examine the instant in time when the fracture

encounters the step change in permeability. Although the effect of the permeability interface is felt slightly prior to the fracture tip reaching the interface*, low permeability in the initiation zone minimizes this effect. The critical event under study is what happens as the fracture front effectively reaches the interface and fluid loss from the fracture can no longer be approximated by one-dimensional leakoff perpendicular to the fracture walls. Figure 2.6 above, idealizes the tip leakage model as a fracture reaches a step change in permeability, the reservoir parameters k_1 and k_2 representing the low and high permeabilities, respectively. Several assumptions are implicit in Figure 2.6; primarily, the preflood zone is assumed semicircular regardless of the contribution due to transverse flow. This is somewhat compensated by increasing the crack opening to an effective value, δ_{eff}, which is used to incorporate the transverse flow through the permeable fracture walls.

Parallel flow into the crack tip zone also contributes to the fluid preflood and is included by producing an effective crack opening that simulates the flow through the permeable media in addition to the flow through the crack. The parallel flow acts through the leakoff zone depth, x_L, shown here in Equation (2.11).

$$x_L = \sqrt{\frac{2\,\Delta p\, k_1 (t-\tau)}{\mu \phi}} \tag{2.11}$$

Where Δp represents the difference between fluid pressure and pore pressure. Using the leakoff depth, the parallel flow is shown here side by side with the flow through the fracture.

$$Q_{\parallel} = 2\frac{x_L k_1}{\mu}\frac{\partial p}{\partial r}\bigg|_{\text{Crack Tip}} \qquad Q_{FC} = \frac{\delta^3}{\overline{\mu}}\frac{\partial p}{\partial r}\bigg|_{\text{Crack Tip}} \tag{2.12}$$

---

* For fracture initiation in the low permeability strata, the preflood zone is typically small compared to the fracture dimensions. Investigation of the inverse case, high permeability initiation and growth into a low permeability zone, can be found in Appendix G.

The effective crack opening may therefore be approximated with the following function:

$$\delta_{eff} = \delta + \left(\frac{Q_{\parallel}}{Q_{\parallel} + Q_{FC}} \right) x_L \tag{2.13}$$

The result of Equation (2.12) can now be used in Equation (2.9) above. Although the parallel flow is typically small, it is included to achieve some generality. To further generalize the model, for smaller permeability contrasts, a preflood time can be subtracted from the holding time. The preflood time is of the same form as the holding time, with the originating permeability, k_1, substituted for the approaching permeability, k_2. For permeability differences of order 10^3, as tested in the lab and field, this contribution is essentially negligible but for lower contrasts, most notably where $k_1 = k_2$, subtracting the preflood contribution reduces the holding time to zero (the desired limit).

2.3 Temporal-Spatial Relationship

The permeability-barrier behavior over time is characterized by three possible cases. The first occurs when the fracture is feeding the preflood zone, the second occurs as the fracture begins to open and propagate, the third occurs as the open fracture closes as a result of dropped fluid flow or continued leakoff. This complex 'valve - like' [40] behavior can be described by three distinct regimes. The first involves the situation where insufficient fluid has leaked-off to produce the pressure gradient necessary to open the fracture. This behavior is characteristic of the flow into the preflood region from the fracture tip. The second case is typical of fracture propagation where the flow is greater than required to produce the Darcy law pressure drop equal to the confining stress and the additional flow can be used to extend the fracture. The third situation occurs as the flow rate drops below the required value and the volume of the fracture must drop, closing the fracture, to maintain the required Darcy pressure gradient.

CHAPTER 3

DEVELOPMENT OF SIMULATION

3.1 Dimensional Scaling

Development of fracture models has relied heavily on numerical and laboratory simulations. While simulation of complicated situations is well suited to numerical modeling, characterization and verification of new phenomenon is better suited to laboratory simulation. In order to accurately represent the physical conditions present in the field, it is required to apply correct dimensional scaling. The importance of properly scaling laboratory experiments is accentuated by the presence of leakoff in the fracture which introduces more mechanisms which must be accurately scaled for good correlation to field conditions.

3.1.1 Previous Work

Scaling of laboratory conditions to field conditions has traditionally been carried out through the characteristic numbers, τ^*, σ^*, and R_w developed in Refs. [22,46] and established in the laboratory e.g. Refs. [11,12,34,39,46-48] The development of these characteristic numbers is detailed in Appendix F.

3.1.1.1 Verification of Elastic Model

Significant work has been done to establish the validity the elastic models and the development here is suited to elastic behavior only. [11,12,28,34,40,45,46,49,50] Other non-elastic effects which may impact fracture propagation, such as crack tip dilatancy,

are not included in this analysis and are not present in the purely elastic DISLASH system.

3.1.2 Field Scale / Lab Scale

The process of developing laboratory simulations begins with an understanding of the range of conditions encountered in the field*. The three main concerns for scaling of field conditions are the size scale, time frame, and fracture stability. Of these concerns the range for size scale is the largest constraint. Fractures which are of order 100 m in the field must be scaled to lab dimensions of less that one meter. The experimental time also constrains the conditions under which tests must be performed. Fracturing operations can take place over days but need to be simulated in the lab in more reasonable times of order minutes. Coupled to these constraints is the concern for fracture stability. Hydraulic fracturing operations are typically quasi-static crack propagation and experimental conditions should accurately simulate controlled fracture growth. Integration of the relevant parameters necessary for correct dimensional scaling has been addressed in Refs. [39,51].

3.1.2.1 Properties

The number of material properties considered for inclusion in dimensionless groupings should be limited to those properties relevant to the situation under investigation. For this reason, several material properties have been embedded into parameters. The crack opening modulus, $\overline{E}$, is a combination of the Young's modulus and Poisson ratio as they appear in the elastic crack opening equations, which results in no loss of generality. Similarly leak-off dependent variables are lumped into the leak-off coefficient, K_ℓ, which is different for each layer under stratified conditions. K_ℓ is a grouping of variables associated with Carter type flow, detailed in Ref. [9].

---

* Graphs detailing the range of laboratory and field parameters are located in Appendix B.

3.1.2.2 Higher Viscosity

Using the scaling parameters developed above and in Appendix F the viscosity required for adequate pressures, time and fracture width yielded a viscosity of O(10,000 cSt). Although lower viscosities would have produced suitable scaling relationships, the higher viscosity is required to prevent surface irregularities from disturbing the flow field in the interface.

3.2 DISLASH

The DISLASH system has been under continual development and improvement since its conception over ten years ago. The main concept, simulation of hydraulic fracture through interface separation, has not changed but the laboratory implementation has improved dramatically. The system discussed here was especially modified for this study and is detailed in Appendix D. While the history of the apparatus can be found in many references [34,45-49,52,53] the original work details a much different system than is in place today.

3.2.1 Assumptions

In order to properly interpret the results of DISLASH testing there are several factors which must be considered. Among these factors are:

- Confining / Contact Stress
- Non-Infinite Medium
- Half-Crack Model Assumptions
- System Compliance / Response Time

Other more general modeling assumptions, such as zero fracture toughness, are discussed in Chapter 2.

3.2.1.1 Confining / Contact Stress

It has been established that fracture growth rate is somewhat dependent on confining stress in DISLASH, e.g. Refs. [11,50]. Although the more recent studies have determined that the role of confining stress is small [11], proper measurement and

uniformity of the interface contact stress is important for interpreting fracture growth rates and fracture geometries. Appendix C details the studies of this phenomenon and verifies the hypothesized uniformity of contact stress required for detailed experimental analysis.

3.2.1.2 Half-Crack Model Assumptions

One advantage of the DISLASH system over other methods is the ability to visually observe the fracture through the relatively rigid, clear PMMA top block. This, of course, produces a fracture configuration that is only half of a normal fracture. It has been established in previous work [11,45] that the functional lumped parameter relationship between crack opening and modulus for DISLASH allows scaling of the 'half-crack' to full crack results by doubling the crack opening modulus, $\overline{E}$. The relationship shown in Equation (3.1) represents the self-similar growth dependence relationship for hydraulically driven fractures where p is the excess pressure, δ is the fracture opening, and γ_1 is the fracture opening integration parameter, or gamma factor [22,33,35,54].

$$\frac{\delta}{R} = \gamma_1 \frac{p}{\overline{E}} \tag{3.1}$$

For scaling of DISLASH results, the doubled $\overline{E}$, is used in the scaling relationships and characteristic numbers developed in Appendix F.

3.2.1.3 Non-Infinite Medium

In contrast to field situations where the fracture is propagating through an essentially infinite medium, DISLASH fractures propagate in an interface constrained by two finite blocks. The presence of the free surface affects the crack by allowing crack openings which are larger than those in an infinite region. The crack behaves as if the material were softer. An elegant solution presented by Barr in Ref. [28], uses the result of Keat [55] that the "effect on deflections is uniform over the entire surface for fractures

of 4.5 cm radius within a cylinder of radius 7.0 cm." Using these results from Ref. [28], it is possible scale the apparent modulus of the DISLASH Silastic block by the relationship in Equation (3.2), where K_{Icyl} and $K_{I\infty}$ are the stress intensity factors for a penny shaped crack in an cylinder, and infinite medium as presented in Ref. [56] and represented in Figure 3.1.

$$\bar{E}_{eff}(R) = \frac{\bar{E}}{K_{Icyl}/K_{I\infty}} \tag{3.2}$$

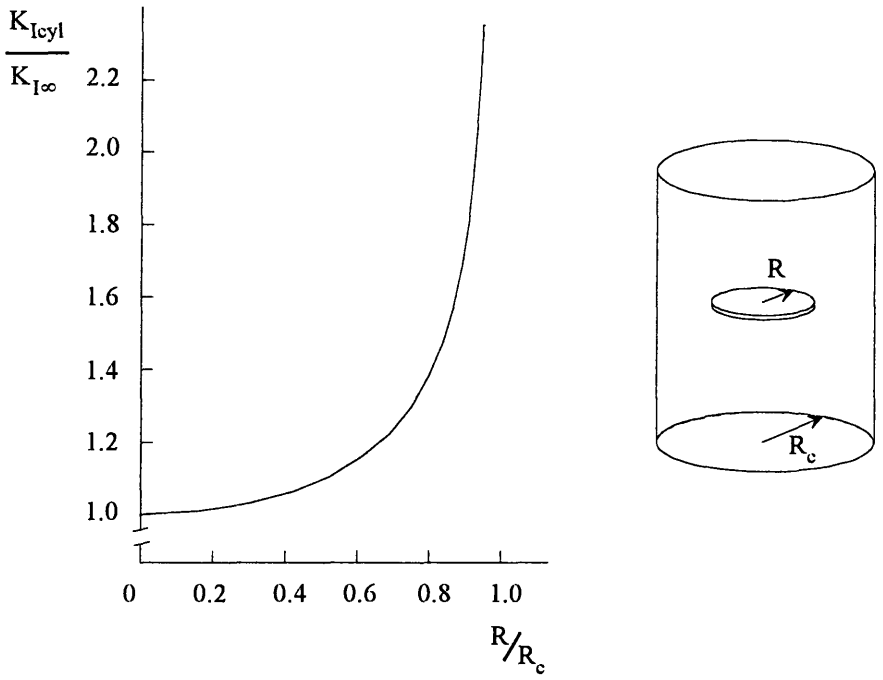

Figure 3.1 Effect of Free Surface on Stress Intensity Factor
Results taken from Refs. [28,56]. Using this scaling parameter increases the accuracy of modeling DISLASH fractures, although the result is only evident for larger radii (R/R_{cyl}) ≈ 0.6 while typical DISLASH tests are only used to (R/R_{cyl}) = 0.72.

3.2.1.4 System Compliance / Response Time

Significant time lags in the DISLASH system have been attributed to compliance of the fluid and fluid supply lines, e.g. Refs. [28,39]. Redesign of the system, detailed in Appendix D, have significantly reduced the lag time in the pressure probes and uniform,

automated pre-pressurization of the system by the data-acquisition system has almost completely removed the variable delay time to initiation common in previously reported work.

3.3 Permeable Materials

Various attempts at simulating low permeability conditions in DISLASH have produced useful but limited results. The permeabilities were not measured accurately, and only in the axial direction. The first attempts to quantify the required materials identified the need for a material with very specific modulus and permeability. [19] Material specification and uniformity was the principal difficulty facing experimental efforts

3.3.1 Foams

Several researchers have attempted to study the effects of permeability on hydraulic fracture in DISLASH. A Scott felted foam was chosen for testing and large amounts of work was done with this material. [11,13] All analysis assumed one-dimensional leakoff into the material and the results were interpreted using this assumption.

The principal problem with using foams as a permeable material, as it was attempted in Refs. [11,13], is the uniaxial compression of the sample in DISLASH. As the foam is compressed by the rolling diaphragm, the foam 'cells' crush flat creating inhomogeneity in the material. As a result, the permeabilities are different in the axial and transverse directions. In Scott felted foams the permeabilities are 0.2 mD in the axial direction, as compared to 20 mD in the transverse direction. (See Figure 1.4). Other foams were tested and the inhomogeneities were similar in magnitude and the results can be found in Appendix E. The much larger transverse permeability accentuated the presence of a pre-flood zone ahead of the fracture.

3.3.2 Granular Materials

The current implementation of permeable materials in DISLASH has overcome the weaknesses of previous studies and allowed a much greater control over the material properties. In order to produce results that can be scaled to field conditions, specific permeability and modulus constraints are imposed on the material selection process. By using granular materials, a more accurate geometric similarity to field conditions can be achieved and the permeability can be controlled by varying the size distribution of the particles. Although there is no specific means of theoretically determining the permeability based on the size distribution of particles, experimental trends were developed to aid in producing the proper mixtures for desired permeabilities.

The permeable samples are constructed of a mixture of plastic powders ranging in size from 710 μm to less than 35 μm. Theses are separated into various size ranges and then mixed together in fixed ratios to achieve desired permeabilities. Once the powders are mixed together, a binding solution of Fuller "hot melt" adhesive dissolved in methylene chloride (an organic solvent which dissolves the glue but does not harm the plastic) is added and mixed thoroughly. The mixture is then poured into a mold to cure for approximately 48 hours. As the solvent evaporates the glue encapsulates the plastic powder particles, binding them together, leaving tortuous passageways, with relatively few entrapped void spaces. The glue is not 'sticky' to the touch at room temperature and does not dissolve in the DC200 fluid used in DISLASH.

By changing the proportions of different particle sizes the permeability of the sample can be adjusted to desired values. Specifics of the permeabilities achieved can be found in Appendix B. Multiple permeability zones can be achieved by casting these different mixtures side by side. The moduli of the samples were found to be essentially independent of the mixture of powder sizes (probably due to the effect of the glue

binder), therefore the multiple layers are step changes in permeability only, with all other properties remaining constant.

3.3.3 Assumptions / Modeling Requirements

The use of permeable materials in DISLASH introduces additional modeling challenges. Ideally, to properly scale all of the factors, the grain size would also have to be scaled to proper geometric proportions. In order to scale the grain size with the size of the fracture, the materials in DISLASH would need to be of order 1 μm to match sandstone grain sizes of 1/16 mm to 2 mm in the field* . [38,57] Particles in the 1 μm range would still produce porous materials but negligible permeability. [57] For this study the permeability is more important than any grain size effects. The impact of grain size on the formation of fractures could be more significant in actual fracturing situations where fracture toughness or dilatancy could impact fracture growth, as opposed to DISLASH which is governed by elastic interface separation. The modeling assumptions are based on Darcy's law which is not effected by the grain size as long as the flow remains in the same flow regime. The granular material - PMMA interface also introduces several new problems.

The model, as developed in Chapter 2, is highly dependent on the assumption of Darcy Flow. Darcy's Law requires that pressure drop through the permeable material be due to viscous forces rather than pressure gradients due to radius of curvature of the flow field. [58] For the materials used in the lab the pore Reynolds number is $O(10^{-5})$ which is well within the valid range for Darcy's Law.

An additional modeling consideration, due to the half crack model, is the flow at the interface especially near the fracture tip due to the high pressure gradients. The flow in DISLASH is different, due to the presence of the impermeable, rigid interface, than

* Particle sizes in the lab are in the 50 μm range.

would actually occur in a full fracture. The impermeable interface prevents fluid slip, while the permeable material permits fluid slip at the fracture wall. Figure 3.2 demonstrates the different conditions possible.

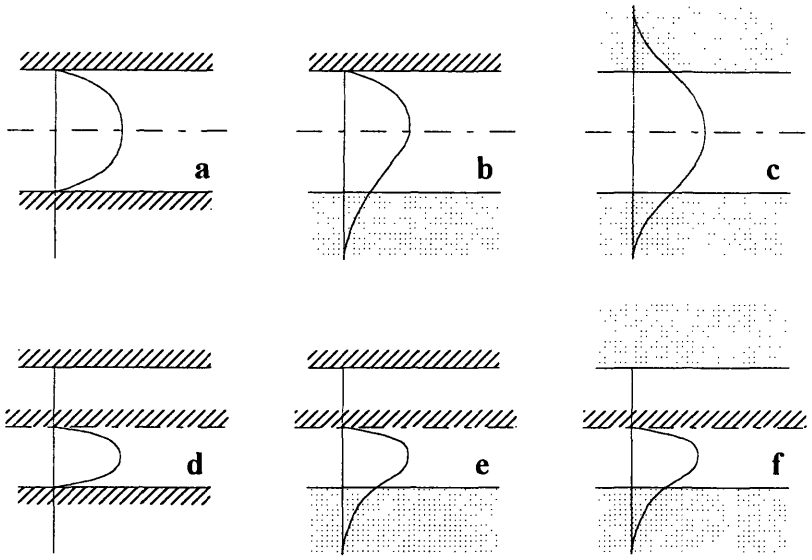

Figure 3.2 Flow Boundary Conditions

The six schematics above represent the possible boundary conditions for flow in the field, **a-c**, and flow as it is modeled in the laboratory, **d-f**. The impermeable configuration is shown in **a**, the permeable configuration is shown in **c**, noted by the continuous velocity profile through the "wall", and the hybrid shown in **b**, (unlikely but possible if fracture were to grow along an interface). In the laboratory the half crack assumption modifies each of the above graphs to produce a no-slip condition at the mid-plane. Notice that **e** and **f** are the same flow condition.

By calculating the total flow rate for each of these conditions it is possible to calculate the level of compromise that is required to model each condition with the half crack approximation. The models for flow through channels such as 3.2 **b**, and **c** have been developed by others e.g. Refs. [41,59-64] and compared to flow through impermeable channels. By modifying the modeling boundary conditions, it is possible to compare those situations represented by Figures 3.2 **c** and 3.2 **f**.

$$\frac{Q_{HC}}{Q_{FC}} = 1 + \frac{(6+3\alpha\beta)(\beta+2\alpha)}{\alpha\beta^2+\alpha\beta^3+3\alpha\beta(\beta+2\alpha)} \tag{3.3}$$

where:

$$\alpha = \sqrt{\frac{\tilde{\mu}}{\mu}}; \qquad \beta = \frac{b}{\sqrt{k}} \tag{3.4}$$

with the gap thickness, b, the permeability, k, and effective viscosity, $\tilde{\mu}$ as defined by Neale and Nader in Ref. [60] where they propose that the parameter $\tilde{\mu}$, can typically be set equal to μ, especially for packed spheres. The relative channel thickness, β, can range from $O(10^3)$ for large permeabilities to $O(10^6)$, for small permeabilities. The empirical structural parameter, α, as defined by Beavers et al [59], has values typically O(1).

The ratio of Q_{HC} to Q_{FC} in Equation (3.3) represents the change in flow rate due to the modeling of the fracture as a half crack. For typical DISLASH conditions the above ratio is only $O(10^{-6})$ to $O(10^{-2})$ less than one for low permeability and high permeability cases respectively. The only regime where this parameter is of concern is near the fracture tip, where, due to smaller fracture opening, the flow could be as much as 30% higher if there were significant fluid penetration. The model described in Chapter 2 accurately represents flow in the surrounding medium by breaking the flow near the tip into two components, the radial tip fed flow, and the transverse flow through the leak off layer into the preflood region.

The second effect of the half crack model is a possible increase in interfacial permeability due to inefficient grain packing at the interface. [61,65] Figure 3.3 illustrates the mechanism. Fortunately, as a byproduct of the granular material casting process where the interface contact surface is cast facing down, smaller granules settle to the bottom. The smaller particles on the bottom face of the sample provide the efficient packing needed to prevent an increase in interfacial permeability. Examination of the tested samples confirm this by displaying no increase in fluid penetration along the interface.

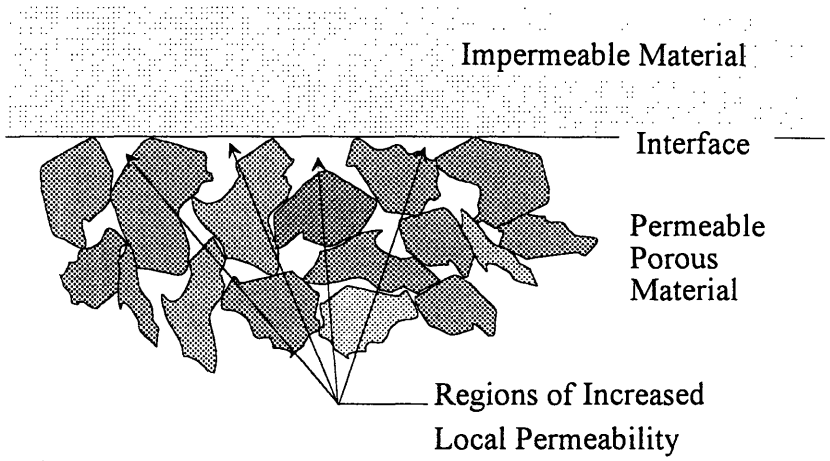

Figure 3.3 Hypothesized Increase in Interfacial Permeability

A third problem introduced by the use of permeable materials is the effect of a different modulus material on fracture opening. By properly choosing the binder for the granular materials it was possible to closely match the modulus of the Silastic rubber. Additionally, the permeable material is only a thin layer placed over the top of the Silastic block. The crack opening is therefore almost completely dependent on the elastic properties of the Silastic block. Testing of permeable samples covered by thin layers of mylar have confirmed that impermeable radial fracture growth is unaffected by the presence of the permeable sample.

3.4 Data Collection

The computerized data acquisition and control system, coupled with pressure transducers and visual data acquisition, provide substantial information for each experiment. The applied confining pressure, wellbore pressure, and in the case of Little DISLASH, the probe pressures are recorded for each test at 10 Hz to adequately capture all transient behavior. The half-crack model and special program instructions, allow visual data collection of the fracture position as a function of time. While the details of the apparatus, especially the more recent modifications, can be found in Appendix D, several experimental samples will be discussed here to outline the capabilities and limitations of the apparatus.

3.4.1 Pressures

The fluid pressure is collected at the wellbore, (and corrected for pressure drop through the smaller wellbore to the interface) as well as at 1 cm increments measured radially from the center of the fracture. This information can be assembled to give a measure of the pressure drop along the fracture which closely follows the representation in Figure 2.3. The probes are pre-pressurized to just below confining pressure, with low viscosity, (1000 cSt) DC200 fluid,* to provide faster time response, and prevent interference with the fracture growth. Typical pressure data can be found in Figure 4.1.

3.4.2 Photographs of Fracture Propagation

It is possible to record the time at which the fracture reaches predefined increments by striking a key on the computer keyboard. This computerized method is useful for fairly steady fracture growth but it is incapable of recording the short transient 'holding time' as the fracture encounters higher permeability regions. To augment the regular data collection, photographs are taken as significant events occur. Photographs of the fracture progression still represent a series of discrete time events, but the added information provides the necessary data concerning fracture holding times. A typical photograph is shown in Figure 3.4, for a Little DISLASH multi-zone experiment described in more detail in Chapter 4.

---

* The probes can only be pressurized for impermeable material testing. The pore pressure and capillarity behavior of the permeable materials would allow the probe fluid to saturate a portion of the material, changing the leakoff characteristics of the fracture. For permeable tests the probes are filled but not pressurized, to limit fracturing fluid from entering into the probes, and prevent contamination of the permeable material.

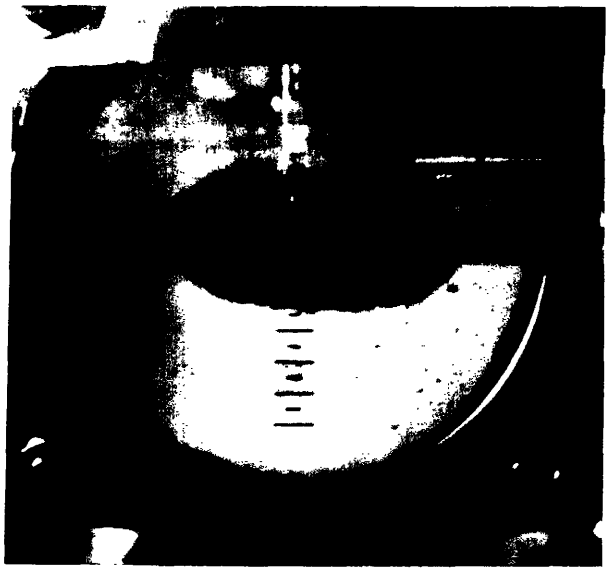

Figure 3.4 Photo of DISLASH Multi-Zone Test

3.4.3 Penetration Depth

The permeability of the samples is well quantified by controlling the mixture of particle sizes and concentrations of binder but additional information can be gathered by noting the fluid penetration depth into the permeable sample. The area near the wellbore, far from the fracture front, where the one-dimensional approximations are most valid, can be used as a cross check on the permeability. By measuring the penetration depth and comparing the depth to that predicted by Equation 3.5, sample to sample variation can be quantified.

$$x_L = \left[\frac{2(p_P - p_F)k}{\mu\phi}\right]^{1/2} \sqrt{(t-\tau)} \qquad (3.5)$$

Where the fluid pressure, p_F, is a function of time.

3.5 Data Reduction

Data for every DISLASH test is assembled from various forms. The pressures and computer entered radii are stored electronically and compared with the photographs of discrete events in the fracturing process. Several corrections to the data are necessary.

The fluid injection pressure must be corrected for the pressure drop through the wellbore due to the known flow rate. The radius data must also be identified as fluid front or fracture front.

3.5.1 Preflood Zone

During the fracturing process the fluid prefloods a region in front of the fracture to create the necessary pressures to separate the faces of the fracture. This preflood zone represents the difference between the fluid front and the fracture front. The scale of this zone is determined by the fluid rheology and the permeability of the material. DISLASH tests typically exhibit preflood zones of maximum one cm in length, for very large leakoff conditions, to zero for impermeable conditions.* By observing the propagating fracture through the side of the block it is possible to observe this phenomenon. Unfortunately it is impossible to capture this behavior with a simple overhead monocular camera setup so the data must be collected manually as the test is being performed.

3.5.2 Pressure

Although it was previously required to filter and smooth pressure data due to system noise, modifications made to the system have reduced the noise to acceptable levels as discussed in Appendix D.

* For an impermeable situation there is actually a non-penetrated zone in front of the fluid front due to the large pressure gradient that would be necessary to move fluid into the small fracture tip area.

CHAPTER 4

TESTING AND RESULTS

The performance of the DISLASH system is well quantified. Thousands of DISLASH tests have been run over the history of the apparatus. [11-13,45-50,53,66-68] In the course of this research, over one hundred granular tests have been performed. The results of these tests have been examined by category, separated by the viscosity, material tested, and testing configuration. The results shown in this chapter represent individual data sets or characteristic curves where appropriate. The details of the DISLASH experimental procedure can be found in Appendix D.

4.1 Radial Growth

Uniform, impermeable, radial growth is the baseline, calibration test for DISLASH. Numerous researchers have verified the results [11,12,28,34,40,45,46,49,50] and thousands of tests have confirmed its repeatability. For each permeable test, an impermeable test can be run by covering the sample with a thin layer of mylar. The mylar protects the permeable sample and allows any variation in the surface properties to be detected. The results of this test can be used to test the uniformity of the specimen stiffness and thickness. The effect of the uniformity of confining stress is extremely critical due to the interest in the fracture geometry. It has been shown that in-situ stresses can be one of the predominant influences on hydraulic fracture geometry. [14,69,70] By verifying the uniformity of the contact stress, any changes in crack shape are attributed to the effect of the permeability contrast.

Comparing the radial growth of tests performed using only the Silastic block and tests with a thin permeable specimen over the block, it has been determined that the modulus of the thin sample, which is close to the modulus of the Silastic rubber, has little or no effect on fracture growth.

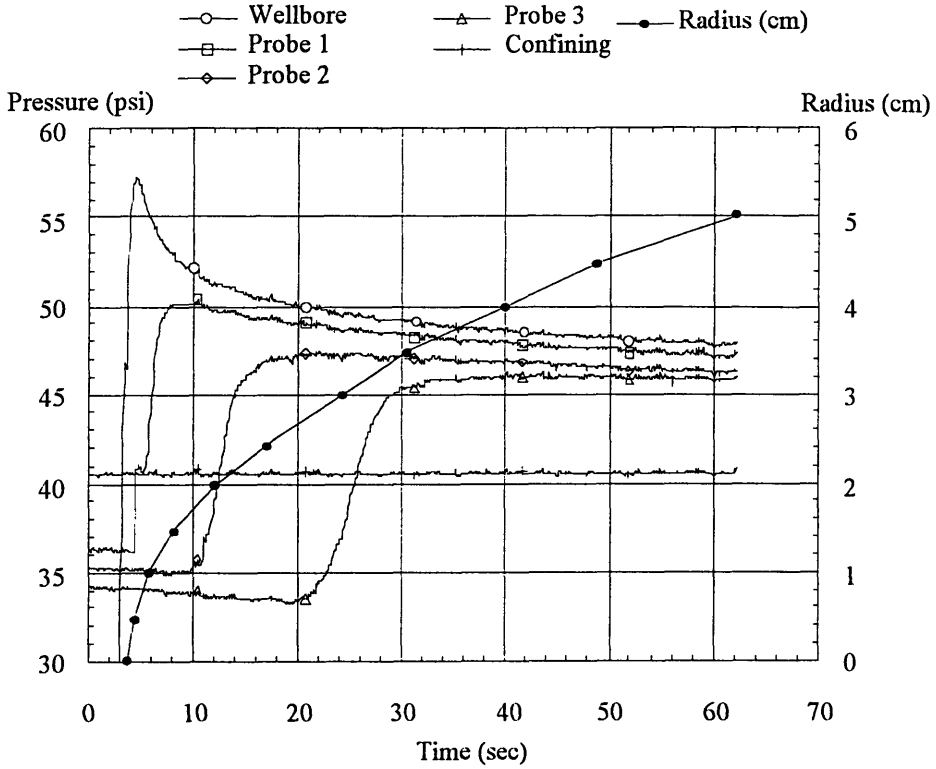

Figure 4.1 Uniform, Impermeable, Radial DISLASH Test

In order to understand multi-zone behavior, it is necessary to quantify the uniform permeable situations. The key factors that must be understood and quantified are the one-dimensional leakoff through the walls of the fracture; the preflood zone in front of the opened fracture; and the behavior of the materials in the apparatus as a scaled simulator. The material properties have been quantified under in-situ-like conditions and the results can be found in Appendix B. The model for fluid leakoff through the fracture walls and fracture tip was developed in Chapter 2.

4.2 Pressures

Figure 4.2 below depicts a typical Little DISLASH, uniform permeable test. The fluid front radius is plotted on the same time axis as the pressures. The wellbore pressure for the permeable test is higher compared to the pressure shown in Figure 4.1, as expected. In a constant injection rate test the fluid leakoff produces a smaller fracture opening which contributes to the higher wellbore pressure. Of particular interest is the slow build up of the pressure in probe 2 at 2 cm from the wellbore. This type of behavior is typical of fracture in permeable materials and indicates the presence of a preflood zone in front of the actual fracture. Examining the area of interest from 35 seconds to 50 seconds is shown in Figure 4.3. If the slow increase in the probe pressure were due only to the preflood zone the dimension of the zone could be calculated by multiplying the mean fluid front velocity, (for the time of interest), by the affected time. For this case, the predicted preflood dimension would be approximately 0.227 cm. This is an over estimate due to the compliance of the fluid in the probe lines and the pressure drop near the tip of the actual fracture which extends the time the probe is affected by the passing of the fluid/fracture front.

Using the information from the probes it is possible to determine the approximate pressure distribution along the fracture as a function of radius. Assuming a static situation it is possible to apply the solution for an internally pressurized crack from Refs. [71,72], to predict the fracture opening as a function of radius. By integrating the opening to find the total fracture volume, it is possible to compare to the volume pumped at a known flow rate. The results for an impermeable Little DISLASH test are shown in Figure 4.4 and the radial match is excellent. For a permeable simulation the volume of the fracture is matched to the volume pumped minus the volume leaked off normal to the fracture walls and leaked off through the fracture tip to produce the preflood zone.

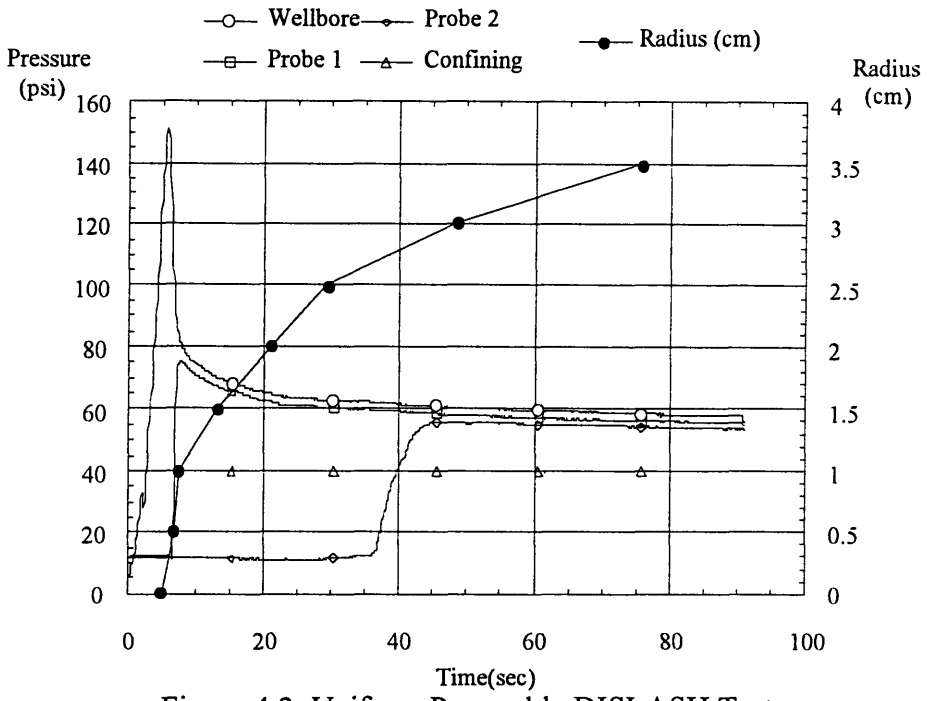

Figure 4.2 Uniform Permeable DISLASH Test

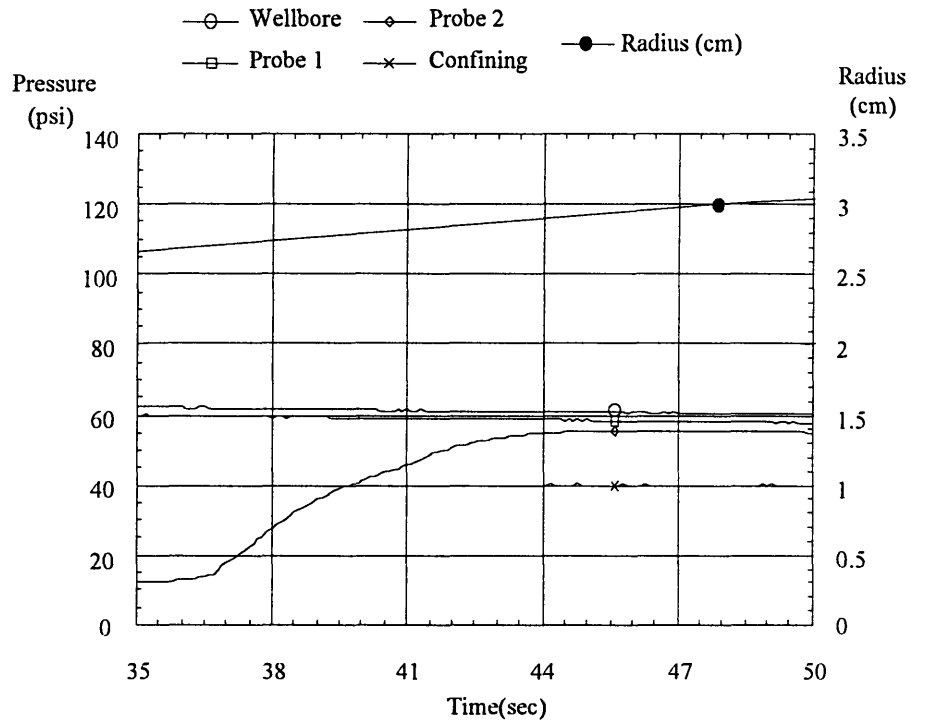

Figure 4.3 Uniform Permeable DISLASH Test (Zoomed)

This graph represents the portion of the test during which the fluid front is crossing the probe located at 2 cm from the wellbore.

Assembling this information, it is possible to predict the location of the fracture front and the fluid front to within reasonable accuracy (± 8% volume (max.) or ≈ ±2% for radial measurement). Figure 4.6 shows the comparison of fluid front to predicted fracture front. The magnitude of the predicted preflood zone for fluid front radius equal to 2 cm is ~ 0.2 cm which agrees with the pressure observations from Figure 4.3.

The specimen can be cut apart after the test to reveal the level of fluid penetration. The photo shown in Figure 4.7, demonstrates the level of fluid leakoff along the fracture for a uniform permeable test.

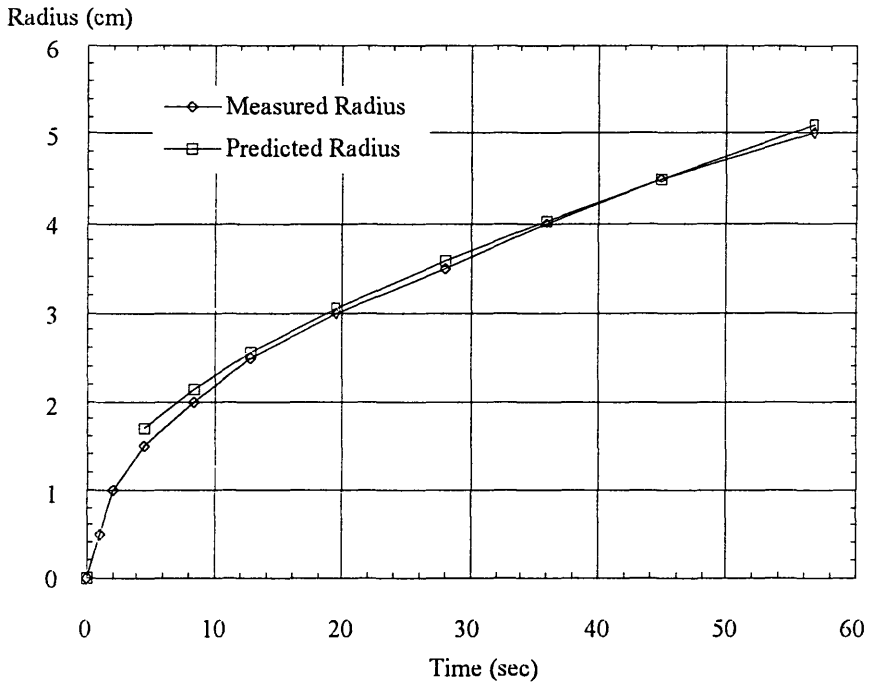

Figure 4.4 Measured and Predicted Fracture Radius for Impermeable Test
The predicted fracture front radius for the uniform impermeable test presented above agrees with observations of the growing fracture. Small radii do not match for this technique because of the transients occurring in the first few seconds of growth.

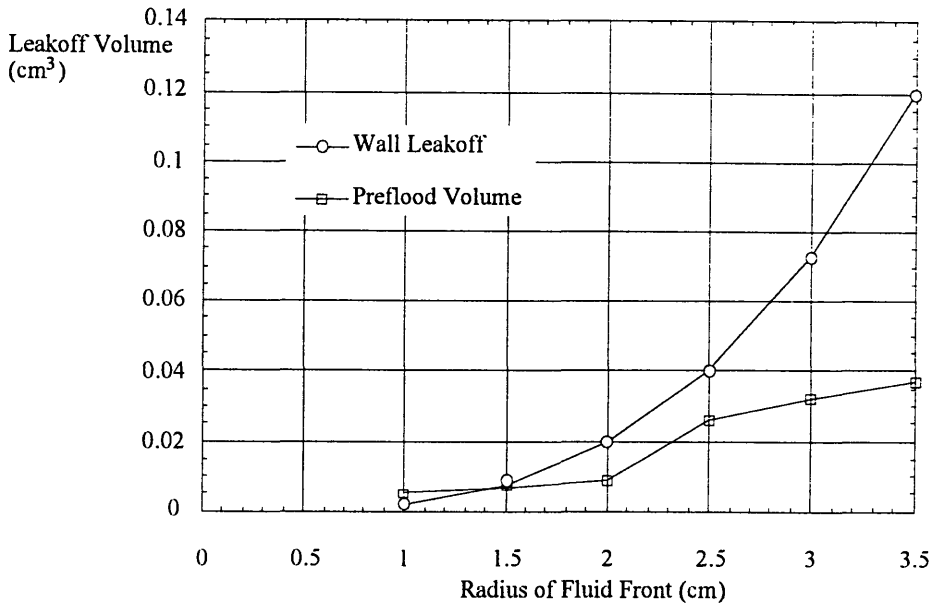

Figure 4.5 Predicted Leakoff Volumes for DISLASH Test

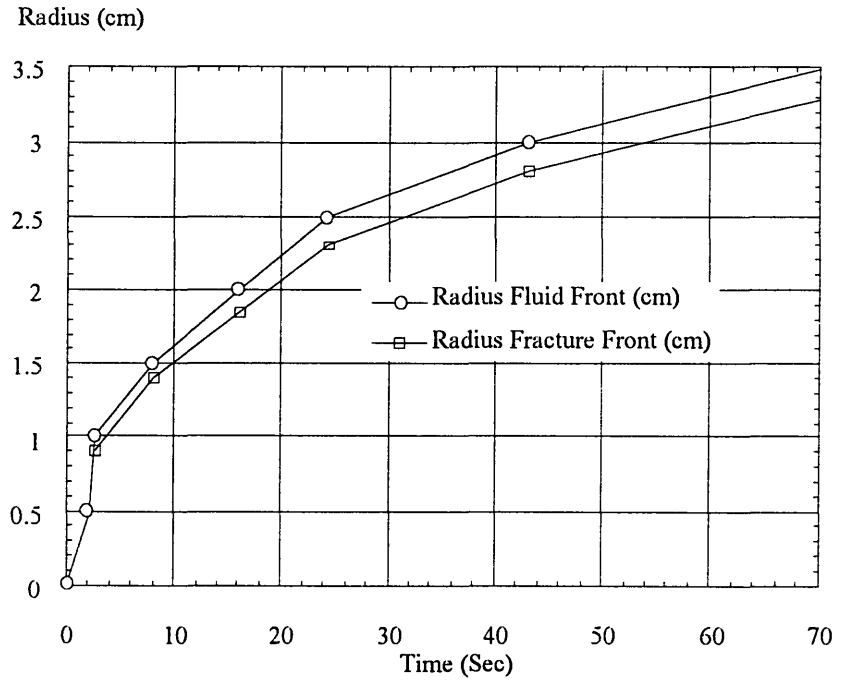

Figure 4.6 Fluid and Fracture Front Radius

The predicted fracture front radius for the uniform permeable test presented above agrees with observations of the growing fracture which exhibits a significant preflood area in front of the fracture. The preflood zone is distinguished by observable contact between the PMMA and the permeable sample in the fluid saturated region just behind the fluid front, followed by a marked fracture opening.

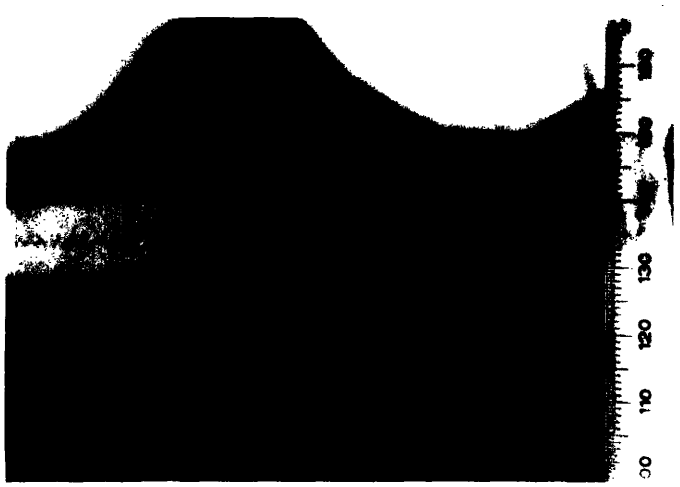

Figure 4.7 Fluid Penetration for DISLASH Test

By visually recording the penetration depth from photographs as shown in Figure 4.7 it is possible to compare the predictions for leakoff using one-dimensional and two-dimensional assumptions to the experimental values. Comparing the values in Figure 4.8, the one-dimensional model predicts a much shallower penetration depth than observed, especially near the tip. The two-dimensional representation of the leakoff behavior predicts a preflood zone which correctly models the larger degree of penetration.

4.3 Length / Height vs. Time

For interpretation of the data, the dimension from the wellbore to the fracture tip, in the direction aligned with the initiating permeability zone, is designated as the length of the fracture by field conventions. The height is measured at right angles to the length, perpendicular to the direction of the initiating zone, measured from the point of injection.

Numerous experiments were performed for various permeabilities and many levels of contrasts. This section will detail a low contrast case and a high contrast case demonstrating the effect of permeability barriers and validating the holding time predictions from Chapter 3.

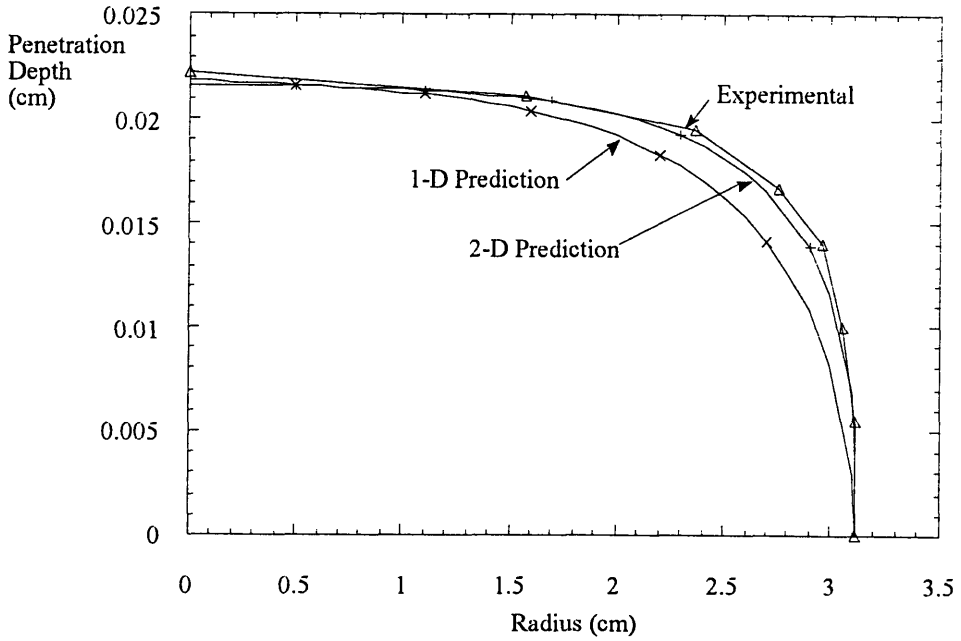

Figure 4.8 Fluid Penetration for DISLASH Test (1-D, 2-D and Experimental) The triangles on the experimental curve represent actual data points, while the +'s and ×'s are for identification only. Also note the different scales used for the axes, the abscissa is 3.5 cm total scale and the ordinate is 0.025 cm total scale.

By compiling a number of data sets it is possible to characterize the data for multi-zone tests in relation to the uniform permeable configuration. Figure 4.9 below shows the fracture front growth for a moderate permeability contrast. Also on the graph are the curves for uniform permeable cases representative of the initiating low permeability and for the approaching high permeability material. Although the multi-zone data represented here was acquired from still photographs it is possible to identify the effect of the permeability barrier in terms of a holding time. The interesting point on this graph occurs as the fracture reaches the contrast interface. The height growth stops, holding the fracture at the interface while the length dimension continues to grow. After a brief period, the fracture begins to propagate in the height direction once again. The large scale representation of the data shows the fracture growing the same as for the uniform low permeability in the length direction, and approaching the growth level of the uniform high permeability in the bounding high permeability regions.

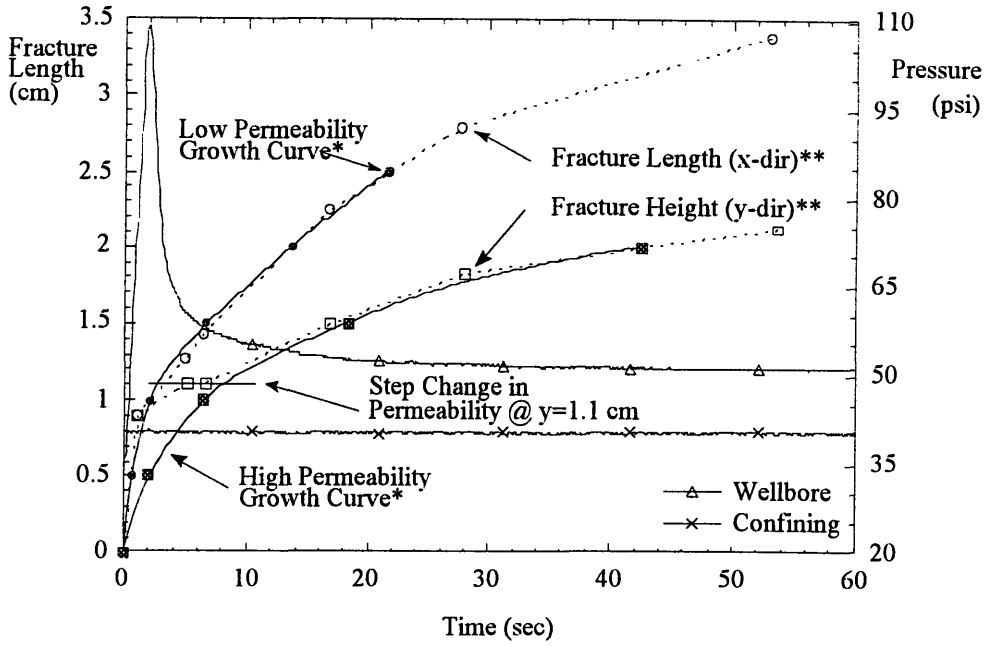

* Curve Fits to Experimental Data N=6
** Experimental Data Points

Figure 4.9 Multi-Zone Length and Height Growth (Low Contrast)

Photos from a very high contrast experiment demonstrate the level of fracture containment possible in stratified permeability situations. The experiment was run using 10,000 cSt fluid at an injection rate of 0.04 cc/sec, into a low permeability region. The fluid front makes contact with the permeability interface at approximately 4 seconds and begins preflooding the surrounding material. The fracture is shown growing in the length direction, slightly accentuated in Figure 4.10**b**. The test continues, further propagating in the length direction, and beginning to develop sufficient preflood in the high permeability zone to initiate growth in Figure 4.10**c** as evidenced by the deepening in the color associated with fracture opening verses the lighter coloring of preflooding. Figure 4.11 demonstrates the significant difference of preflooding verses opening. The last frame in Figure 4.10 shows the depth of penetration into the sample after 70 seconds of injection into the fracture. The central zone is only slightly penetrated due to the low permeability, while the high permeability zones demonstrate the predicted leakoff patterns.

The contrast in Figure 4.9 above represents a moderate contrast in permeabilities between the initiation and approaching zones. A larger contrast is shown in Figure 4.12 below where the growth is significantly accentuated by the presence of the permeability barriers. The holding time is still evident by the two points as the fracture reaches the permeability contrast. The significance of this test is the growth in the low permeability region which is faster than the growth for a fracture in a uniform sample of the same material. The growth in the higher permeability region is similarly retarded. This behavior is a result of the lack of, or greatly reduced fracture opening in the high permeability regions. Because this test was run using a constant injection rate, the volume of the fracture is defined by the pumping rate. If the wings of the fracture in the higher permeability regions are not as wide, the fracture must extend further in the length direction to compensate.

4.4 Comparison to Theory

The characteristic 'holding' time predicted by the model in Chapter 2 and observed in tests similar to those discussed above, can be non-dimensionalized and plotted to demonstrate the range of behavior observed. In Figure 4.13 the dependence on the level of the higher permeability, the abscissa for the graph is:

$$\frac{k(\sigma_c - p_P)\bar{\mu}\bar{E}^3}{\mu(p_F - \sigma_c)^4 k'}$$

where the permeability, k, is the higher permeability k_2, and k' is the permeability based on r_i at time equal to τ_c. The factor, k', determines the nucleating radius, r_i', and is based heavily on material microstructure; for Figure 4.13 a grain size of 3.1×10^{-4} cm is used to calculate k' from Equation (2.7). The ordinate of Figure 4.13 represents the normalization of the characteristic 'holding time' to the fracture propagation time.

$$\frac{\tau_c(p_F - \sigma_c)^4}{\bar{\mu}\bar{E}^3}$$

The right hand portion of the curve tends towards large numbers where the fracture is contained almost indefinitely by the permeability barriers. For DISLASH conditions, Point **1** represents a very high contrast test in which the fracture was contained in the low permeability region by the higher permeability O(1000 mD), for the duration of the test.

The middle region signifies where the fracture will appear to stop for a finite time, at Point **2** the high permeability region of O(10 mD) contained the fracture for approximately one second which matches with the curve prediction. Point **3** on the graph represents a low permeability contrast where the fracture is uninhibited by the presence of the increase in permeability. The predicted characteristic holding time of only one tenth of a second is below the resolution of the data collection.

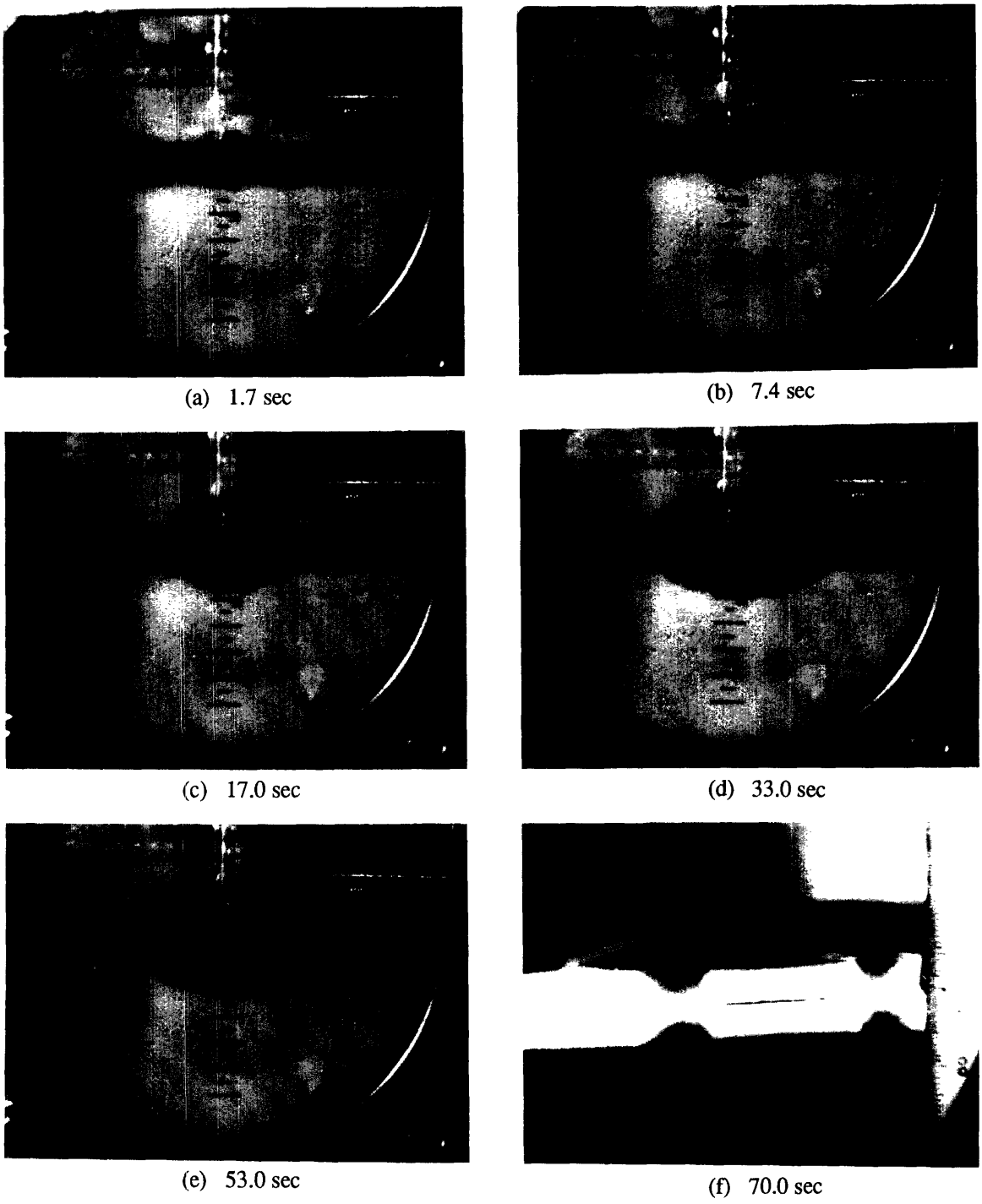

(a) 1.7 sec

(b) 7.4 sec

(c) 17.0 sec

(d) 33.0 sec

(e) 53.0 sec

(f) 70.0 sec

Figure 4.10 Photographs of Multi-Zone Growth (High Contrast)
This test was run at 40 psi confining pressure, with 10,000 cSt fluid injected at 0.04 cc/sec. The bonded granular materials were cast simultaneously to produce an idealized interface with no stress contrasts and a step change in permeability. Fluid can flow through the interface, parallel to the fracture, better simulating actual conditions.

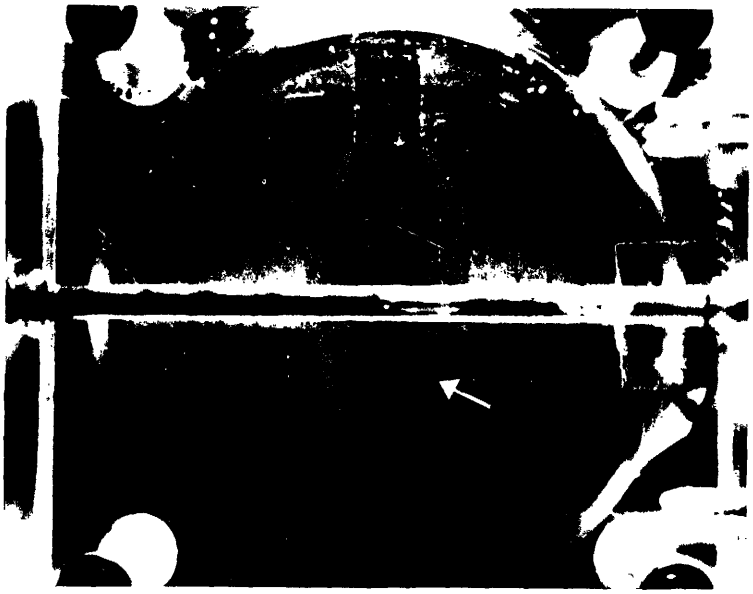

Figure 4.11 Photograph of Multi-Zone Growth (High Contrast)

This photograph shows a foam multi-zone experiment with an extremely low permeability initiation zone and high permeability approaching zones. Prior to the test the sample surface was lightly sprayed with a reflective paint to better define the regions where the fracture had actually opened. The arrow indicates the high permeability region where the fluid has penetrated, but from the indication of the reflective paint, the fracture has not opened. This behavior is characteristic of the higher transverse permeability foams which exhibit larger preflood zones than would be expected in isotropic materials.

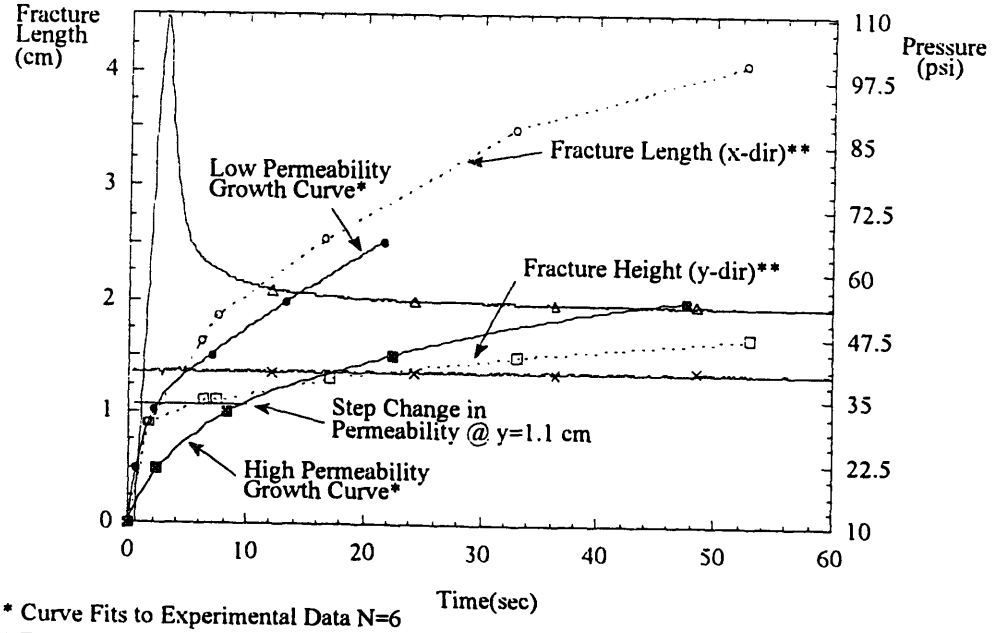

* Curve Fits to Experimental Data N=6

** Experimental Data Points

Figure 4.12 Multi-Zone Length and Height Growth (High Contrast)

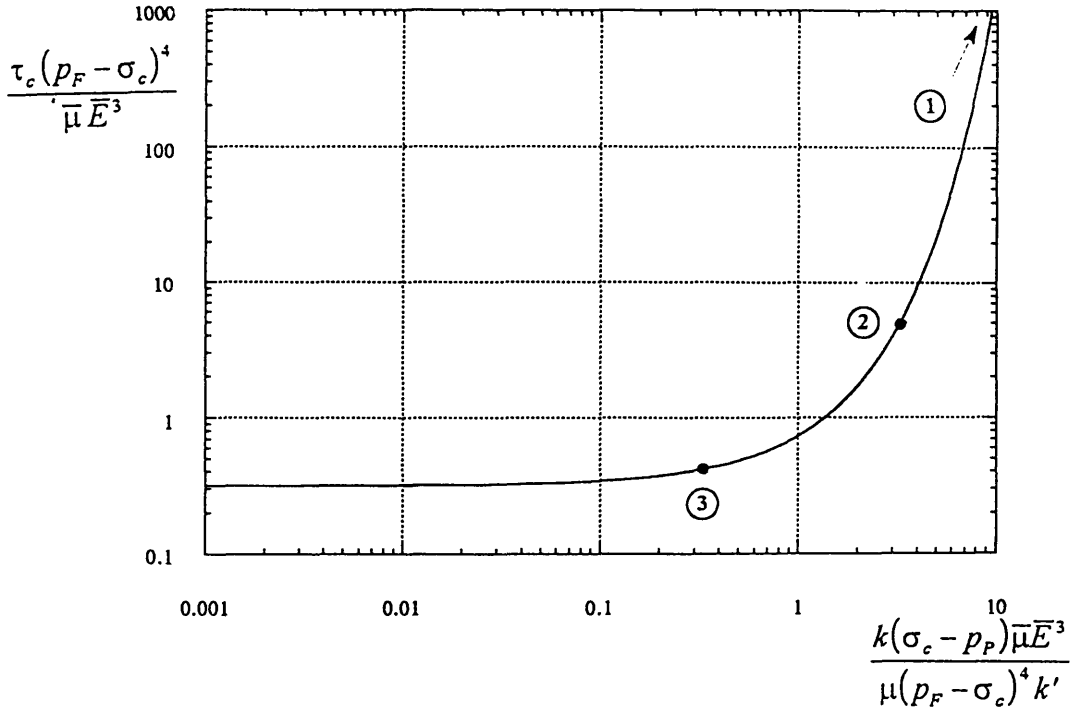

Figure 4.13 Non-Dimensionalized Characteristic 'Holding Time'

4.5 Agreement / Problems with Numerical Simulators

The numerical simulators have several difficulties when modeling laboratory conditions. FRACPRO, the simulator with lumped-parameter, discussed previously, is incapable of accepting lengths of less than one foot on some of the input screens. Although this is never a problem when modeling field conditions, the small height of the multiple zones in DISLASH presented problems because heights must be entered as integers. This limitation is bypassed by scaling the laboratory results to the corresponding field values. The results for multi-zone growth are shown in Chapter 5. FRACPRO does not exhibit the 'holding time' type behavior exhibited in the above plots but, by careful choice of the contrast coefficients, it is possible to match the level of growth retardation into the high permeability zones, seen in the laboratory experiments.

CHAPTER 5

FIELD APPLICATION

The direct field applications of this research can be used to increase oil and natural gas recovery in regions of high permeability where the fluid leakoff into adjacent strata is sufficient to retard fracture propagation. Of particular note are situations where the desired resources are present in adjacent strata, or 'pay zones', of different permeabilities. The expense involved in drilling and producing wells requires recovery of the maximum amount of oil possible. Situations where such a large volume of oil is unrecoverable are uneconomical for the production companies. For example, in Figure 5.1 the two zones depicted are oil bearing rock of essentially the same porosity. Note that zone 1 has a permeability lower than zone 2 and is also significantly larger, therefore containing the majority of the oil.

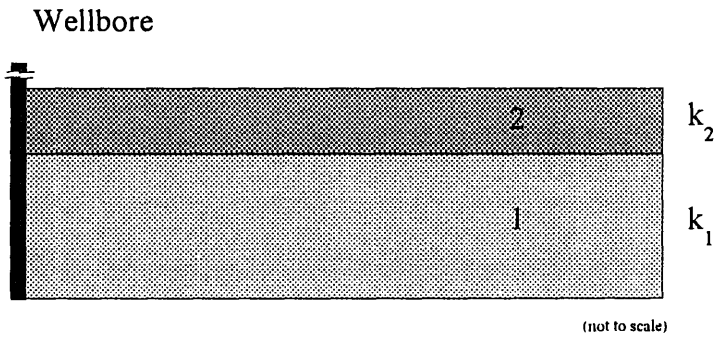

Figure 5.1 Simplified Pay-Zone Strata ($k_1 < k_2$).

One method of recovering this oil involves waterflooding* the reservoir: injecting from one well and removing the oil through a second well. Traditional methods require perforating the wellbore in both the upper and lower pay zones and injecting fluid to displace the oil from both zones. The outcome of this process would be unfavorable because the higher flow permeability of zone 2 causes that zone to be swept first, as shown in Figure 5.2. This results in poor recovery of oil from zone 1 which is especially costly in this case because its dimensions are much greater than the upper zone. The majority of the oil would still be trapped in zone 1.

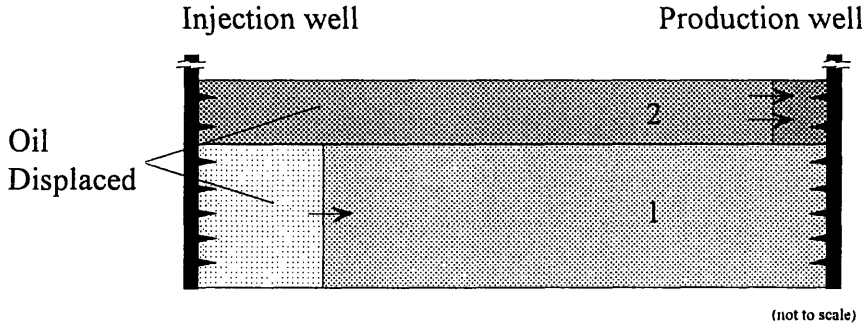

Figure 5.2 Waterflood into Strata with High Permeability Contrast.

In order to maximize productivity and recovery in this situation it is possible to apply the models developed for permeability contrasts to identify the magnitude of the permeability barrier's influence in containing the fracture to pay zone 1. Containing the waterflood process to zone 1 would enhance the recovery from that region. The process involves perforating the wellbore in the bottom, low permeability region, thereby aiding fracture initiation in that region. By injecting above the reservoir parting pressure, the fluid forms fractures which are contained in zone 1, (Figure 5.3). The fracture acts as a localized permeability increase which allows more water to flow into the bottom pay-zone displacing the oil. The fracture continues to grow for the holding time, t_c, discussed

* This method of improved oil recovery is discussed in Chapter 1.

in Chapters 3 and 4. At the end of the holding time, the fracture begins to propagate into zone 2, and the waterflood begins leaking into the higher permeability stratum at which point pumping should be stopped, causing the fracture to close, thus preventing the upper zone from flooding out.

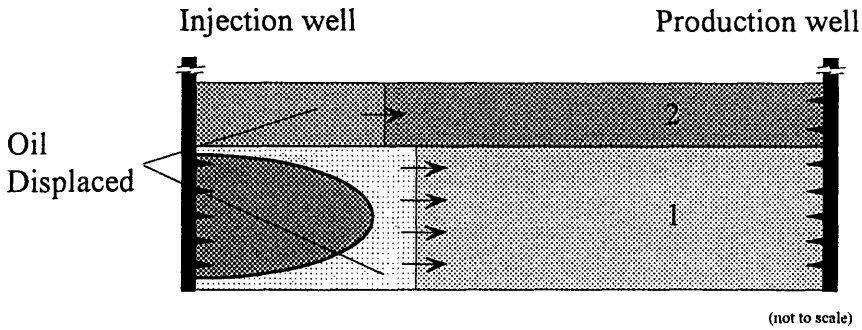

Figure 5.3 Waterflood with Fracture into Strata with High Permeability Contrast.

This technique is a significant improvement over the traditional approach because the procedure can further increase the area of the low permeability region swept by 'shutting in' the well (stopping injection of water and allowing the pressure to fall off) when the fracture reaches zone 2. After a short time the fluid in the fracture will leakoff, allowing the fracture to close. For example, if the holding time is of order 10 days shutting in for one day would allow the reservoir pressures to equilibrate. After the reservoir pressure has equalized, the water injection can continue. The fluid will begin to reopen the original fracture(s), and as the top of the fracture approaches the interface, tip leakoff will prevent fracture propagation with another 'holding time'. This cycle can continue repeatedly until the reservoir has been depleted or water has broken through to the producer well.

Several caveats must be considered when employing this procedure. Because reservoir parameters cannot be measured without uncertainty‡, the holding time cannot

‡ There is inherent uncertainty in the well logging process. Reservoir properties can only be measured a small distance from the wellbore and large fracture growth can interact with materials over a large distance.

be determined exactly and the procedure followed should include several additional phases. During the injection process the pumping rate should be changed or stopped periodically, for miniature shut-ins, to verify that the fracture has not grown into the higher permeability stratum This can be determined from the pressure falloff behavior. Also, the figures above show a very simple strata configuration to demonstrate the proposed procedure. The elements of the wellbore, fracture, perforations, etc. are not drawn to scale. Fracturing usually produces more than one fracture wing and the two-dimensional diagrams are meant to show only the general, large scale behavior and not the specific flow patterns surrounding the fracture or near the strata interface.

5.1 North Sea Water Injection

It is possible to apply this procedure to a field situation. Among the information and data available for study are data sets for sea-water injection into several North Sea wells described in Ref. [73]. The fracturing treatment data acquisition was significantly aided by the use of downhole gauges which provided actual pressures seen near the fracture. The use of sea water as a fracturing fluid also simplified the analysis by removing any hypothetical fluid reactions under the large overburden, that may have affected the fluid leakoff for a more complex fluid.

5.2 Description of Situation

Of particular interest to this study are the relatively high permeability levels encountered for one of the wells, Statoil A[†]. The information concerning the exact strata, or formation structure has not been released but the dominant factors include a low

[†] Although the data for the well and treatment history has been released, permission has not been grated for the use of the well name, field name, or location. For convenience the well will be referred to as Statoil A, in reference to the service company that operates the well and has released the data for publication.

permeability zone bounded above by a relatively high permeability streak. The pumping schedule and data set collected are shown in Figure 5.4.

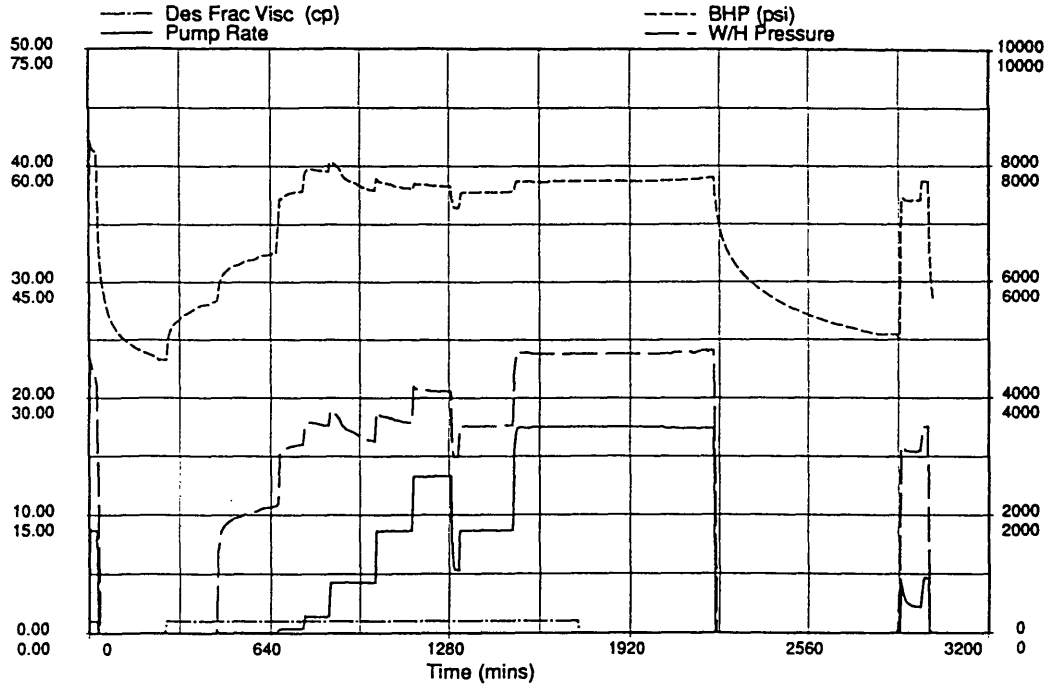

Figure 5.4 Injection and Pressure Gauge Data.

The downhole gauge allows real time collection of the bottom hole pressure (BHP).

5.3 Numerical Simulation

5.3.1 Use of Laboratory Coefficients

Laboratory conditions were scaled using the dimensional relationships discussed in Chapter 3 and Appendix F, and entered into the FRACPRO simulator. A growth and pressure history match was then achieved by redefining the parameter coefficients which are used for modeling permeability contrasts, shown in Figure 5.5. For close matches to the laboratory results the coefficients were modified from the defaults as shown in Table 5.1. A mean growth curve from laboratory experiments was used for the matching process. The laboratory results for one of these cases is shown in Figure 4.9. The coefficients in FRACPRO have some physical meaning, as denoted by the column titles.

The *Distance Effect* controls how far from the interface the effect of the change in permeability is felt. The *Containment Effect* determines the 'strength' of the effect, and the *Permeability Level* represents some value, below which the effect of permeability contrasts are insignificant. This final variable was not modified from the default because the laboratory results used, and hypothetically the field case, all exhibited some level of containment.

Table 5.1 Relevant FRACPRO Permeability Contrast Coefficients.

	Distance Effect	Containment Effect	Permeability Level
FRACPRO Defaults	3.0	3.0	0.25
Laboratory Match	4.0	4.0	0.25

The default coefficients used in FRACPRO for permeability contrast behavior are not theoretically derived, instead they are the result of previous matches to field results. Field data is much more complex, for reasons discussed above, and the fracture is not observable. Matching to laboratory experiments is one method of refining the model. Several other coefficients also needed to be changed to accurately represent the elastic nature of the DISLASH experiments, namely γ_{i2} was changed to 0.5 from the default of 0.0001 to compensate for the purely elastic opening in DISLASH.

5.3.2 Fracture Growth

After matching the above results, the Statoil A well data from Figure 5.4 was modeled using the containment coefficients from above. Using the simulator it was possible to produce matches to the observed pressures, shown in Figure 5.6. The pressures compared favorably The fracture geometry detailing the level of fracture containment predicted by the simulator is shown in Figures 5.7 and 5.8.

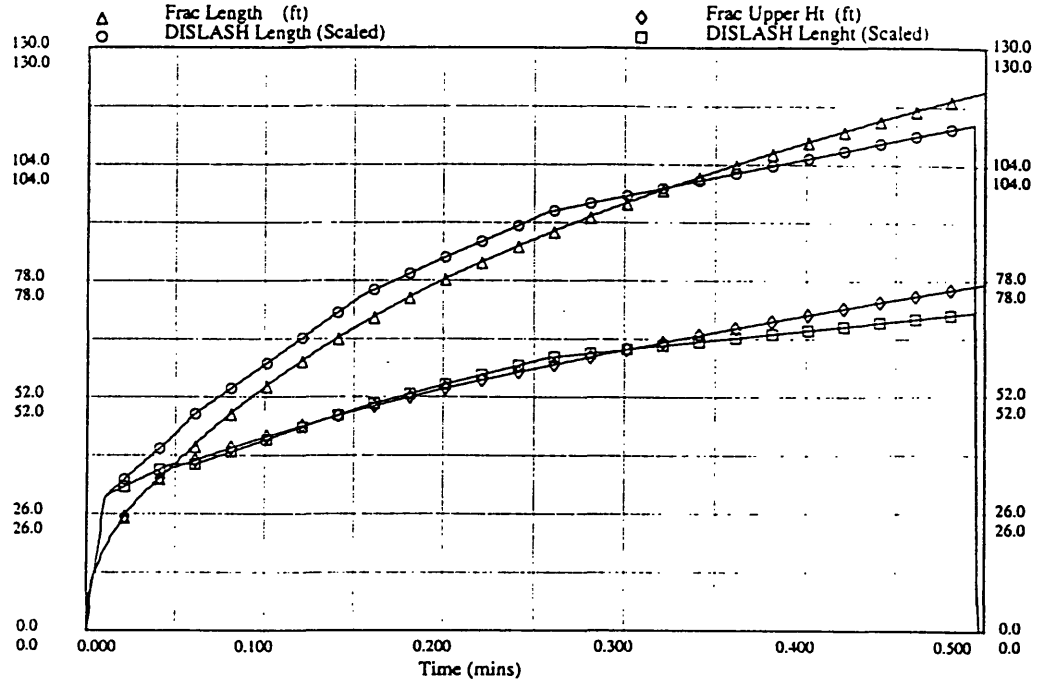

Figure 5.5 DISLASH Multi-Zone Results Matched by Simulator (Scaled)

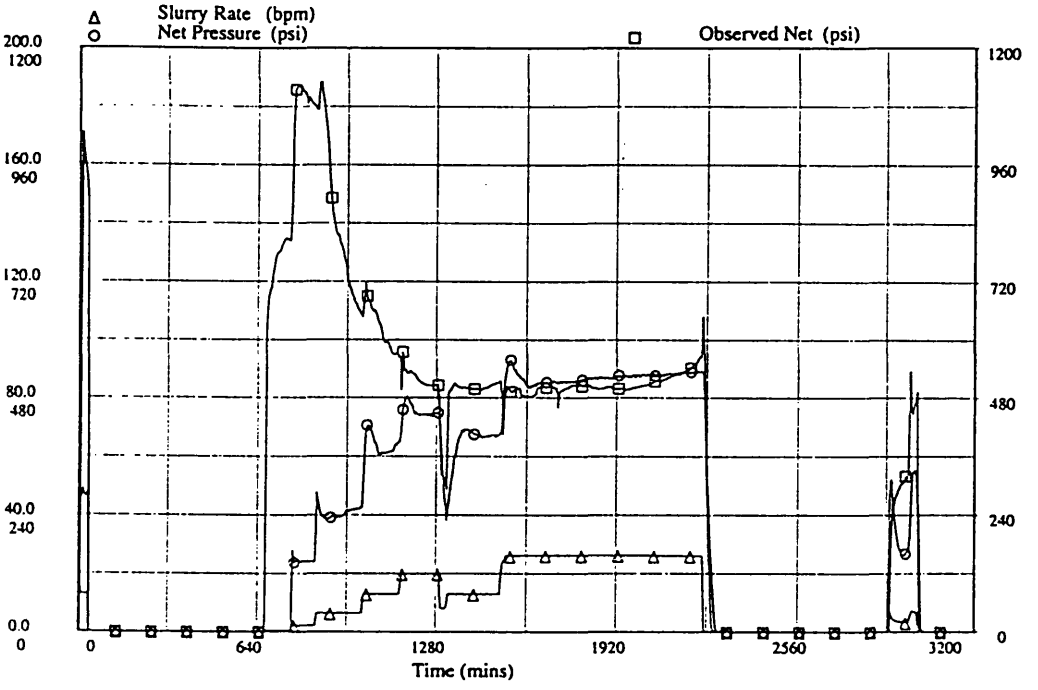

Figure 5.6 North Sea Water Injection Well Pressure Match From Simulator

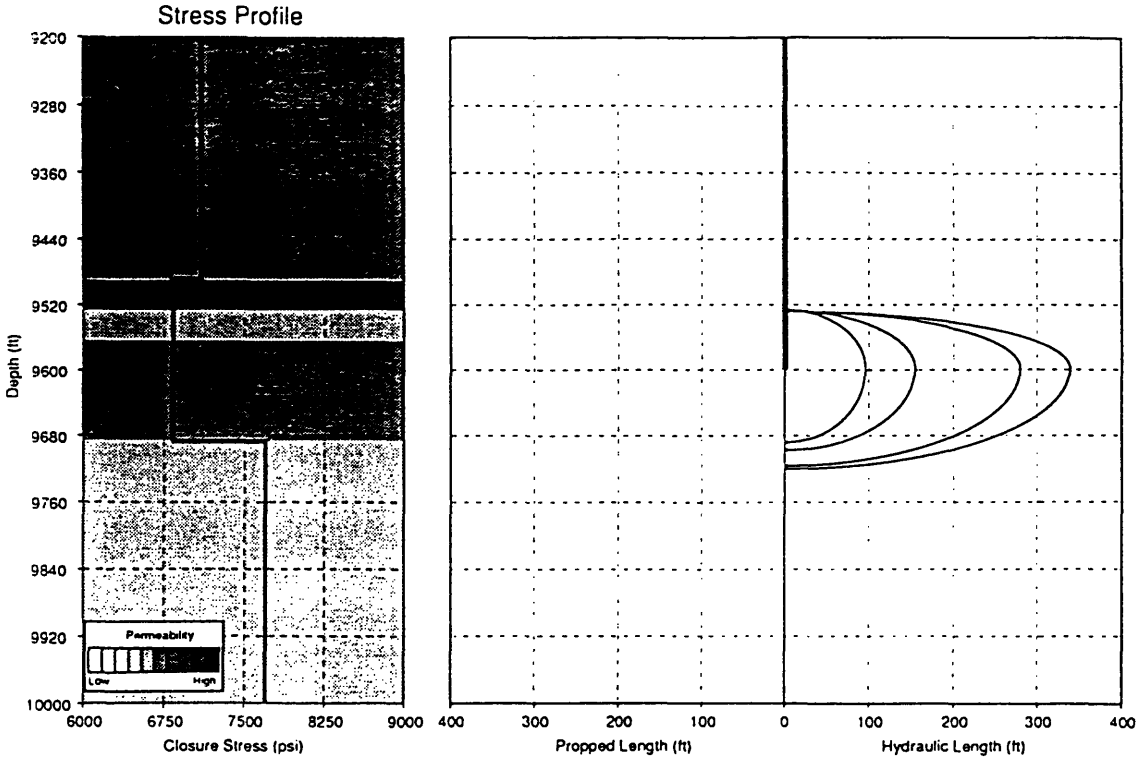

Figure 5.7 North Sea Water Injection Well Fracture Geometry From Simulator

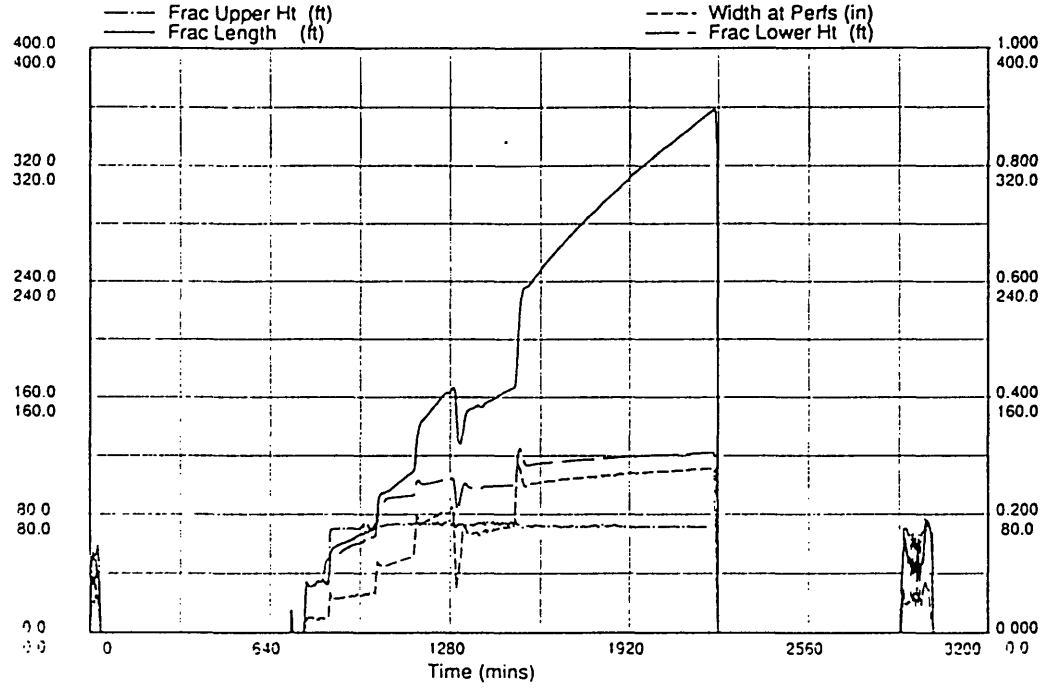

Figure 5.8 North Sea Water Injection Well Fracture Length and Height From Simulator
Note containment of upward fracture growth while the fracture length continues to grow.

5.4 Evidence of Containment

If the contrast coefficients are changed to produce no confinement the results are strikingly different. The predicted fracture geometry is shown in Figures 5.9 and 5.10.

Using the simulator it was possible to compare situations where the fracture propagated up into the higher permeability streak as opposed to being contained by the permeability barrier. The pressures predicted for the contained case better match the observations from the field.

Using the laboratory derived parameters is was possible to characterize the fracture growth and closely match the pressure behavior. From the modeling it is assumed, and in the laboratory it has been demonstrated, that the holding time for this situation would be finite and for continued pumping the fracture would begin propagating into the high permeability zone. This behavior was observed by secondary field evidence which confirmed that the fracture penetrated up through the high permeability streak into the strata above at a later date. [40,74]

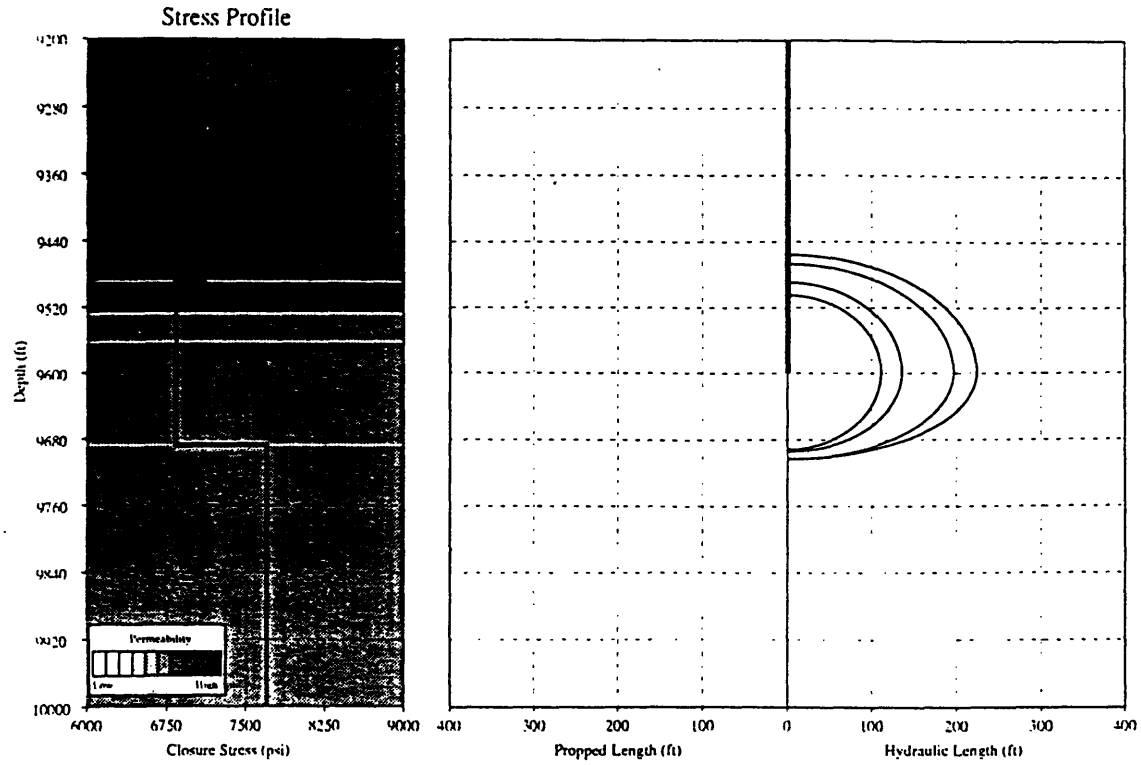

Figure 5.9 North Sea Water Injection Well Fracture Geometry (No Containment)

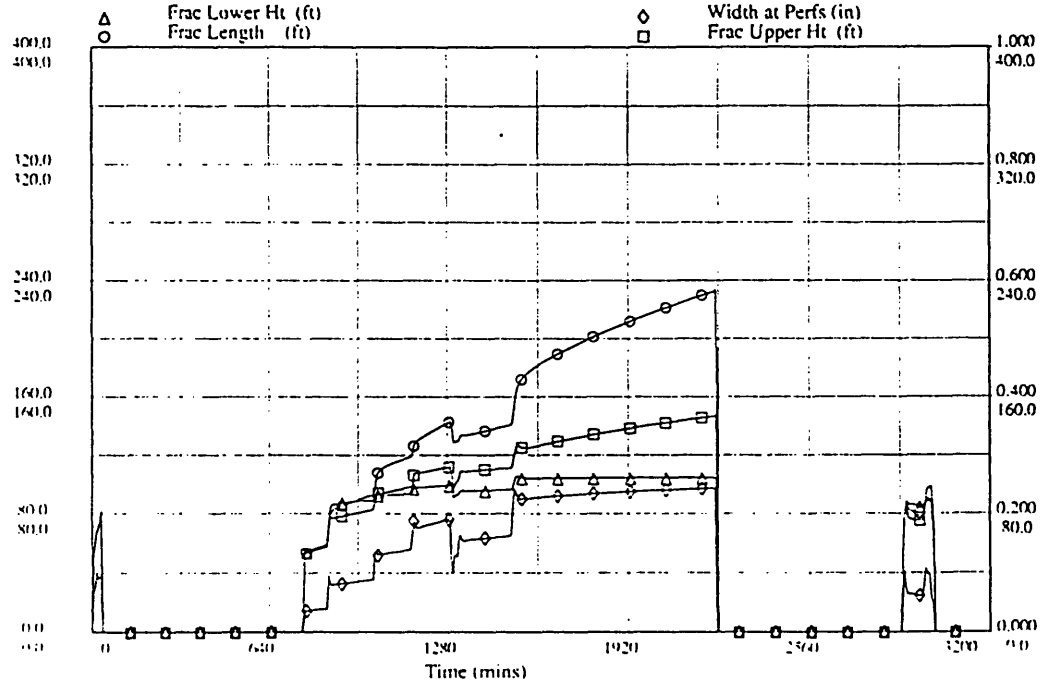

Figure 5.10 North Sea Water Injection Well Fracture Length and Height

CHAPTER 6

CONCLUSIONS AND RECOMMENDATIONS

This research has verified the existence of permeability barriers using a laboratory scale apparatus and quantified their behavior as a function of material parameters. In order to properly evaluate and predict leakoff behavior, a two dimensional model has been developed. In the course of the work isotropic permeable materials were developed and implemented in DISLASH to accurately model leakoff conditions over a wide range of permeable conditions.

6.1 Role / Contribution of Preflood Zone

Using the two-dimensional model to predict the level of fluid leakoff ahead of the fracture the penetration depth of the fluid was matched to the theoretical expectations and observations of penetration levels matched the predicted levels of preflooding. This information, coupled with matches of radial growth, served to validate the tip leakoff models required to study permeability contrasts.

6.2 Effect of Multi-Zones

The permeable materials were used to simulate stratified permeability conditions. The multiple zone cases investigated demonstrated the impact of permeability barriers through visual identification of the fracture propagation. Use of the bonded, granular, permeable materials allowed investigation of contrasts in permeability without the need to compensate for differences in other material properties such as modulus or confining stress.

Fracture 'holding times' were observed in the laboratory and found to agree with theoretical predictions. The range of permeability contrasts investigated in the lab produced varying levels of fracture containment. Very large contrasts produced containment of fracture growth for the duration of the test while smaller contrasts verified the existence of a finite 'holding time' which inhibited fracture growth until sufficient preflood levels were established to allow continued fracture propagation. The agreement to theoretical predictions for holding time was good over the entire range tested. Unfortunately, size limitations on the apparatus limited testing times so situations which induced very long holding times were contained for the duration of the test and propagation in the higher permeability zones could not be observed.

6.3 Consequences for Field Studies

The results of the laboratory simulations were used to calibrated the permeability contrast coefficients of a commercially available field hydraulic fracture simulator. The simulator was then used to interpret field data provided by Statoil. The results produced agreement with observed pressures for the field case. Further use of this model and the implications of verification of permeability barriers and quantification of holding times associated with contrasts in permeability could greatly impact efforts at recovery of resources in stratified, high permeability regions. The impact for 'waterflood injection above parting pressure' described in Chapter 5 presents a concrete example of the impact this research can have on field operations. Enhanced recovery of resources and increased profitability of hydraulic fracturing in highly stratified conditions is possible with proper implementation of these results.

6.4 Recommendations

This study has resolved several problems surrounding the DISLASH system. The experimental error has been reduced below the threshold of the existing equipment's measurement systems. Consequently, any further apparatus improvements would require

to completely rebuilding DISLASH to higher tolerances with higher quality transducers and data acquisition / control systems. Several additions to the apparatus have been made, including a constant pressure pump system described in Ref. [68], which was not fully implemented in time for inclusion in this study but, could provide additional data for matching to scaled field simulators.

Material behavior of the foams under compression produced interesting results that could be advantageous to other researchers studying non-homogeneous permeabilities for underground and biomechanics related issues. Although full quantification of the material properties was beyond the scope of this work, the apparatus described here, especially in Appendix E, should provide the tools necessary for future work.

Although the behavior of inverse permeability contrasts has only been experimentally modeled here, the methodology could be used to produce numerical simulations capable of simulating the complicated fluid and fracture front geometry described in Appendix G.

This study has shown the impact and physics behind permeability barriers and demonstrated the basis in reality through experimental simulations. Further applications to the field should incorporate other relevant physical considerations, namely thermal and filtercake effects on leakoff, as quantified in Ref. [22] for one-dimensional cases. Combining the complexities of these phenomena with the behavior characterized in this thesis is best left to simulators, such as FRACPRO. The simulation runs using laboratory derived coefficients successfully matched field observations and further work in the industry will hopefully implement the concepts and results presented here.

REFERENCES

[1] Economides, Michael J., and Kenneth G. Nolte, eds. *Reservoir Stimulation.* 2nd ed. Englewood Cliffs, NJ: Prentice Hall, 1989.

[2] Farris, R.F.: Hydraulic Fracturing, a Method for Increasing Well Productivity By Fracturing the Producing Formation and Thus Increasing the Well Drainage Area. U.S. Patent. 23733. issued 10 Nov. 1953.

[3] Waters, A.B. "Hydraulic Fracturing - What Is It?" *Journal of Petroleum Technology* (August 1981): 1416.

[4] Veatch, R.W. "Overview of Current Hydraulic Fracturing Design and Treatment Technology - Part 1." *Journal of Petroleum Technology* (April 1983): 677-87.

[5] Donohue, David A.T., and Karl R. Lang. *A First Course in Petroleum Technology.* Boston: International Human Resources Development Corporation, 1986.

[6] Howard, G.C., and C.R. Fast. *Hydraulic Fracturing.* Dallas, TX: Millet, 1970.

[7] Mian, Mohammed A. *Petroleum Engineering Handbook for the Practicing Engineer.* Vol. 1. Tulsa, OK: PennWell Publishing, 1992.

[8] Ali, Nazir, P.K. Singh, C.P. Peng, G.S. Shiralkar, Z.A. Moschovidis, and W.L. Baack. "Injection-Above-Parting-Pressure Waterflood Pilot, Valhall Field, Norway." *SPE Reservoir Engineering* (February 1994): 22-28.

[9] Howard, George C., and C.R. Fast. "Optimum Fluid Characteristics for Fracture Extension." *Drilling and Production Practice* (1957): 261-70.

[10] Crockett, Alan Richard. "Studies of Fluid Flow, Heat Transfer, and Induced Stresses In and Around Underground Fractures." MS Thesis, Massachusetts Institute of Technology, 1984.

[11] Johnson, Donald Edward. "Experiments and Analysis on Hydraulic Fracture Growth in an Interface Separation Apparatus." MS Thesis, Massachusetts Institute of Technology, 1990.

[12] Johnson, Donald Edward. "Underground Hydraulic Fracture: Leakoff Dependence on Viscosity in a Porous Medium." BS Thesis, Massachusetts Institute of Technology, 1988.

[13] Yap, Jee-Lian. "The Effect of Permeability and the Importance of Fracture Propagation During Shut-in of Hydraulic Fractures." BS Thesis, Massachusetts Institute of Technology, 1990.

[14] Simonson, E.R., A.S. Abou-Sayed, and R.J. Clifton. "Containment of Massive Hydraulic Fractures." *Society of Petroleum Engineers Journal* (1978): 27-32.

[15] Ruina, Andy L. "Influence of Coupled Deformation-Diffusion Effects on the Retardation of Hydraulic Fracture." *Proceedings of the 19th U.S. Symposium on Rock Mechanics, Porous Media Series* 1, no. 15 (June 1978): 41.

[16] Cleary, M.P., and M.E. Hanson. "Development of a General-Purpose Numerical Program to Simulate Hydraulic Fracturing in Brittle (Including Porous) Media." *Quarterly Report for Lawrence Livermore Laboratory* 2 (1 April 1978).

[17] Cleary, M.P. "Primary Factors Governing Hydraulic Fractures in Heterogeneous Stratified Porous Formations." *ASME Publication, Submitted for presentation at the Energy Technology Conference & Exhibition, Houston, Texas.* (1978): 12.

[18] Cleary, M.P. "Rate and Structure Sensitivity in Hydraulic Fracturing of Fluid-Saturated Porous Formations." *Presented at the 20th U.S. Symposium on Rock Mechanics* (1979): 127-42.

[19] Vogeler, Suki, Amaury Fonseca Junior, Andrew I. Gray, Elaine Cohen, and Michael P. Cleary. "Fracture Propagation in Porous Media." *MIT UFRAC Project* 85-8 (1985): 50.

[20] Huang, N.C., and S.G. Russell. "Hydraulic Fracturing of a Saturated Porous Medium I: General Theory." *Theoretical and Applied Fracture Mechanics* 4 (1985): 201-13.

[21] Huang, N.C., and S.G. Russell. "Hydraulic Fracturing of a Saturated Porous Medium II: Special Cases." *Theoretical and Applied Fracture Mechanics* 4 (1985): 215-22.

[22] Crockett, A.R., N.M. Okusu, and M.P. Cleary. "A Complete Integrated Model for Design and Real-Time Analysis of Hydraulic Fracturing Operations." *SPE Paper No. 15069 prepared for the 56th California Regional Meeting of the Society of Petroleum Engineers* (1986): 13.

[23] Gordeyev, Yu N., and A.F. Zazovsky. "Self-Similar Solution for Deep-Penetrating Hydraulic Fracture Propagation." *Transport in Porous Media* 7 (1992): 283-304.

[24] Liu, Ci-qun, and Xiao-Dong Wang. "Transient 2D Flow in Layered Reservoirs With Crossflow." *SPE Formation Evaluation* (December 1993): 287-91.

[25] Cleary, M.P., A.R. Crockett, J.I. Martinez, V.M. Narendran, and S. Slutsky. "Surface Integral Schemes for Fluid Flow and Induced Stresses Around Fractures in Underground Reservoirs." *SPE Paper No. 11632 Presented at the SPE Symposium on Low Permeability held in Denver CO* (1983): 283-94.

[26] Crockett, A.R., R.M.Jr Willis, and M.P. Cleary. "Improvement of Hydraulic Fracture Predictions by Real-Time History Matching on Observed Pressures." *SPE Paper No. 15264, presented at the Unconventional Gas Technology Symposium of the SPE* (1986): 649-61.

[27] Warpinski, N.R., Z.A. Moschovidis, C.D. Parker, and I.S. Abou-Sayed. "Comparison Study of Hydraulic Fracturing Models - Test Case: GRI Staged Field Experiment No. 3." *SPE Production & Facilities* (1994): 7-16. SPE 25890 (see also response to SPE 25890 by M.P. Cleary p17-18).

[28] Barr, David T. "Leading-Edge Analysis for Correct Simulation of Interface Separation and Hydraulic Fracturing." Ph.D. Dissertation, Massachusetts Institute of Technology, 1991.

[29] Resource Engineering Systems, Inc. *R3DH User's Manual Version 1.0 (Three-Dimensional Hydraulic Fracture Simulator).* Cambridge, MA: Resources Engineering Systems, Inc., 1992.

[30] Cleary, M.P., Michael Kavvadas, and K.Y. Lam. "Development of a Fully Three-Dimensional Simulator for Analysis and Design of Hydraulic Fracturing." *SPE Paper No. 11631 Presented at the SPE Symposium on Low Permeability in Denver CO* (1983): 271-82.

[31] Lam, K.Y., M.P. Cleary, and D.T. Barr. "A Complete Three-Dimensional Simulator for Analysis and Design of Hydraulic Fracturing." *SPE Paper No. 15266 presented at Unconventional Gas Technology Symposium of the Society of Petroleum Engineers, Louisville, KY* (1986): 673-83.

[32] Cleary, M.P., R.G. Keck, and M.E. Mear. "Microcomputer Models for the Design of Hydraulic Fractures." *SPE Paper No. 11628 Presented at the SPE Symposium on Low Permeability in Denver CO* (1983): 257-70.

[33] Cleary, Michael P., Christopher A. Wright, and Timothy B. Wright. "Experimental and Modeling Evidence for Major Changes in Hydraulic Fracturing Design and Field Procedures." *SPE Paper No. 21494 presented at the SPE Gas Technology Symposium* (1990): 15.

[34] Johnson, Ed, and Michael P. Cleary. "Implications of Recent Laboratory Experimental Results for Hydraulic Fractures." (1991). SPE Paper No. 21846, presented at the Rocky Mountain Regional Meeting and Low-Permeability Reservoirs Symposium, Denver, CO.

[35] Cleary, Michael P. "Analysis of Mechanisms and Procedures for Producing Favourable Shapes of Hydraulic Fractures." *SPE Paper No. 9260 presented at the 55th Annual Fall Technical Conference and Exhibition of the Society of Professional Engineers* (1980): 16.

[36] Donnelly, Maura Elizabeth. "Permeability Measurements of Compressible, Porous Media." MS Thesis, Massachusetts Institute of Technology, 1982.

[37] Gibson, Lorna J., and Michael F. Ashby. *Cellular Solids: Structure & Properties.* First ed. Oxford, England: Pergamon Press, 1988.

[38] Southard, John B. "Rocks." In *Lecture Notes on Introduction to Geology.* Cambridge, MA: M.I.T., 1992.

[39] de Pater, C.J.Hans, M.P. Cleary, Tim S. Quinn, David T. Barr, D.Edward Johnson, and Leen Weijers. "Experimental Verification of Dimensional Analysis for Hydraulic Fracturing." *SPE Paper No. 24994 for the European Petroleum Conference, Cannes, November* (1992): 13.

[40] Cleary, M.P. "Critical Issues in Hydraulic Fracturing of High-Permeability Reservoirs." *SPE Paper No. 27618 presented at the European Production Operations Conference & Exhibition in Aberdeen, Scotland* (1994): 16.

[41] Neale, Graham, and Walter Nader. "Formulation of Boundary Conditions at the Surface of a Porous Medium." *Society of Petroleum Engineers Journal* (1974): 434-36.

[42] Jones, Lucile Merrill. "Field and Laboratory Studies of the Mechanics of Faulting." Ph.D. Dissertation, Massachusetts Institute of Technology, 1981.

[43] Vipulanandan, C., O.I. Ghazzaly, M.W. O'Neill, and M. Leung. "Laboratory Modeling of Fractured Clay for Hazardous Waste Studies." *Journal of Hazardous Materials* 22, no. 2 (November 1989): 261.

[44] Goggin, D.J., M.A. Chandler, Gary Kocurek, and Larry W. Lake. "Permeability Transects of Eolian Sands and Their Use in Generating Random Permeability Fields." *SPE Formation Evaluation* (March 1992): 7-16.

[45] Quinn, Timothy S. "Comparison of Experimental Results and Theory For Two Laboratory Hydraulic Fracture Apparatus." MS Thesis, Massachusetts Institute of Technology, 1992.

[46] Mastanduno, Richard. "Design and Testing of an Experimental Hydraulic Fracture Simulation Apparatus." MS Thesis, Massachusetts Institute of Technology, 1986.

[47] Mastanduno, R., J. Kwo, J. Putscher, and M. Cleary. "Further Development and Verification of Interface Separation Apparatus." *MIT UFRAC Project* 84-9 (1984): 57.

[48] Bailey, John, Richard Mastanduno, and Michael P. Cleary. "Leakoff Simulation in Interface Separation Experiments." *MIT UFRAC Project* 87-9 (1987): 37.

[49] Papadopoulos, J., D. Summa, and M. Cleary. "Interface Separation: an Experimental Tool for Studying Hydraulic Fracture." *MIT UFRAC Project* 82-14 (1982): 47.

[50] Papadopoulos, J.M., V.M. Narendran, and M.P. Cleary. "Laboratory Simulations of Hydraulic Fracturing." *SPE 11618 presented at the SPE Symposium on Low Permeability, Denver CO* (1983): 161-74.

[51] de Pater, C.J., and F. Wolters. "Dimensional analysis of hydraulic fracturing - Application to model tests." *Report from the Dietz Laboratory, Section Petrophysics, Delft University* (1991): 30.

[52] Curtis, K.W., K.A. Morris, J.M. Papadopoulos, and M.P. Cleary. "A Computer Controlled Fluid Supply System." *MIT UFRAC Project* 82-5 (1982): 46.

[53] Papadopoulos, J.M., V.M. Narendran, J.B. Parse, T.B. Wright, J. Sununu, K. Park, and M.P. Cleary. "Laboratory Simulations of Hydraulic Fracturing." *MIT UFRAC Project* 83-9 (1983): 33.

[54] Cleary, M.P. "Comprehensive Design Formulae for Hydraulic Fracturing." *SPE Paper No. 9259 presented at the 55th Annual Fall Technical Conference and Exhibition of the Society of Petroleum Engineers* (1980): 20.

[55] Keat, William D. "Surface Integral and Finite Element Hybrid Method for the Analysis of Three-Dimensional Fractures." Ph.D. Dissertation, Massachusetts Institute of Technology, 1989.

[56] Kassir, M.K., and G.C. Sih. "Three-Dimensional Crack Problems." In *Mechanics of Fracture*, 294-303. Vol. 2. Leyden, The Netherlands: Noordhoff International, 1975. N.

[57] Southard, John. Conversation with Christian Hamer. May 10, 1994.

[58] Phillips, O.M., F.R.S. *Flow and Reactions in Permeable Rocks.* Cambridge: Cambridge University Press, 1991.

[59] Sparrow, E.M., G.S. Beavers, and L.Y. Hung. "Channel and Tube Flows with Surface Mass Transfer and Velocity Slip." *The Physics of Fluids* 14, no. 7 (1971): 1312-19.

[60] Neale, Graham, and Walter Nader. "Practical Significance of Brinkman's Extension of Darcy's Law: Coupled Parallel Flows within a Channel and a Bounding Porous Medium." *The Canadian Journal of Chemical Engineering* 52 (August 1974): 475-78.

[61] Somerton, Craig W., and Patricia Wood. "Effect of Walls in Modeling Flow Through Porous Media." *Journal of Hydraulic Engineering* 114, no. 12 (December 1988): 1431-48.

[62] Berkowitz, Brian. "Boundary Conditions Along Permeable Fracture Walls: Influence on Flow Conductivity." *Water Resources Research* 25, no. 8 (August 1989): 1919-22.

[63] Richardson, C.P., and A.D. Parr. "Friction and Free-Surface Flow Over Porous Media." *Journal of Hydraulic Engineering* 117, no. 11 (November 1991): 1496-1512.

[64] Shankararaman, Chellam, and Mark R. Wiesner. "Laminar Flow with Slip in Channels With Uniformly Porous Walls." *Journal of Hydraulic Engineering* 119, no. 1 (January 1993): 126-32.

[65] Daniel, D.E., D.C. Anderson, and S.S. Boynton. "Fixed-Wall Versus Flexible-Wall Permeameters." In *Hydraulic Barriers in Soil and Rock.* ASTM STP 874 ed., edited by A.I. Johnson, R.K. Frobel, N.J. Cavalli, and C.B. Pettersson, 107-26. Philadelphia: American Society for Testing and Materials, 1985.

[66] Papadopoulos, J.M., B.A. McDonough, and M.P. Cleary. "Laboratory Simulation of Hydraulic Fracturing." *MIT UFRAC Project* 82-2 (1982): 62.

[67] Chen, Julie. "Contact Stress Measurement in an Interface Separation Apparatus." BS Thesis, Massachusetts Institute of Technology, 1986.

[68] Lanzilotta, Paul Joseph. "Design and Implementation of a Constant Pressure Pumping Apparatus for Hydrafrac Simulation." BS Thesis, Massachusetts Institute of Technology, 1994.

[69] Warpinski, Norman R., Richard A. Schmidt, and David A. Northrop. "In-Situ Stresses: The Predominant Influence on Hydraulic Fracture Containment." *Journal of Petroleum Technology* (March 1982): 653-64.

[70] Warpinski, Norman R., James A. Clark, Richard A. Schmidt, and Clarence W. Huddle. "Laboratory Investigation on the Effect of In-Situ Stresses on Hydraulic Fracture Containment." *Society of Petroleum Engineers Journal* (1982): 333-40.

[71] Sneddon, I.N. "The Distribution of Stress in the Neighbourhood of a Crack in an Elastic Solid." *Proceedings of the Royal Society of London, A* 187 (1946): 229-60.

[72] Sneddon, Ian N. *Fourier Transforms.* International Series in Pure Applied Mathematics, edited by William Ted Martin. 1st ed. York: The Maple Press Company, 1951.

[73] Unneland, Trond, and Torstein Haugland. "Permanent Downhole Gauges Used in Reservoir Management of Complex North Sea Oil Fields." *SPE Paper No. 26871, prepared for the Offshore European Conference in Aberdeen* (1993): 293-305.

[74] Leslie, Kevan. Conversation. March 7, 1994.

[75] Mechtly, G.W. "The International System of Units: Physical Constants and Conversion Factors, Second Revision." *NASA Special Publication* SP-7012 (1970): 20.

[76] Selection Guide to Dow Corning Silicone Fluids. Form number 22-053-76; Information about Silicone Fluids; Dow Corning Bulletin; Dow Corning Corp. Midland, Michigan.

[77] Dow Corning 200 Fluid. Form number 22-069d-76; Information about Silicone Fluids; Dow Corning Corp. Midland, Michigan.

[78] Brace, W.F. "Permeability of Crystalline and Argillaceous Rocks." *International Journal of Rock Mechanics, Mining Science, and Geomechanics Abstracts* 17 (1980): 241-51.

[79] Ipsen, D.C. *Units, Dimensions, and Dimensionless Numbers.* New York: McGraw-Hill, 1960.

[80] Langhaar, Henry L. *Dimensional Analysis and Theory of Models.* New York: John Wiley & Sons, 1951.

APPENDIX A
Conversion Factors

Quantity	Abbreviated Unit	SI Equivalent
Length	in	2.540 000 E -02 m
	ft	3.048 000 E -01 m
Area	in^2	6.451 600 E -04 m^2
	ft^2	9.290 304 E -02 m^2
Viscosity	centipoise	1.000 000 E -03 Pa·s
	lbm/ft·s	1.488 164 E -00 Pa·s
Volumetric Rate	barrel / day	1.589 873 E -01 m^3/d
	mcf / day	2.831 685 E +01 m^3/d
Permeability	mD	9.869 233 E -04 μm^2
Compressibility	psi^{-1}	1.450 377 E -01 kPa^{-1}
Volume	in^3	1.638 707 E -05 m^3
	ft^3	2.831 685 E -02 m^3
	gallon (US)	3.785 412 E -03 m^3
	barrel (42 Gal)	1.589 873 E -01 m^3
Mass	lb.-mass	4.535 924 E -01 kg
Density	lb.-mass/ft^3	1.601 846 E +01 kg/m^3
	lb.-mass/gallon	1.198 264 E +02 kg/m^3
Force	lb.-force	4.448 222 E +00 N
Pressure	psi	6.894 757 E +00 k Pa

(adapted from Refs. [5,75].)

APPENDIX B
Material Properties

B.1 Property Definitions:

B.1.1 Permeability: (intrinsic permeability)

Intrinsic permeability k has dimensions of L^2. Common units are cm^2, m^2 or darcy, (darcy is the more widely used unit in hydrology) A darcy is defined as "the permeability that allows a transport velocity of 1 cm s^{-1} of a fluid with viscosity 1 centipoise (10^{-2} c.g.s. unit) under a pressure gradient of 1 atmosphere per centimeter. [Using] mean atmospheric pressure [of] 10^{-6} c.g.s units, ... 1 darcy is about 10^{-8} cm^2, or 10^{-12} m^2." [58] Permeability can be expressed in a vector form as shown in Equation (B.1), for anisotropic cases. For homogenous cases $k_x = k_y = k_z$.

$$k = \begin{bmatrix} k_x & & \\ & k_y & \\ & & k_z \end{bmatrix} \tag{B.1}$$

B.1.2 Hydraulic conductivity:

Hydraulic conductivity depends on the permeability of the medium and the fluid, and has units LT^{-1} (velocity).

$$K = \frac{\rho g k}{\mu} = \frac{g k}{\nu} \tag{B.2}$$

where $\upsilon = \mu/\rho$.

B.1.3 Porosity:

Porosity or total porosity is defined as the ratio of void volume to total volume of the material. "Isolated cavities or 'dead end' tubes can contribute to [total porosity,] but do not provide pathways to fluid motion." [58] In this work the term 'porosity' refers to connected porosity which is of major interest in fluid motion studies.

B.2 DISLASH parameters:

Material Parameters:

Table B.1 DISLASH Material Parameters

	Young's modulus (psi)	Poisson's ratio	Permeability* Axial (mD)	Porosity (@ 40 psi)
Silastic E Rubber Medium	384	0.4995	0.0	0.0%
2# Gray Foam	23.94†	≈ 0	0.16	71%
2# Ester Foam	28.41†	≈ 0	0.45	49%
2# Pyrell Foam	76.45†	≈ 0	< 0.01	62%
Chevron Fine (CF)	1200‡	‡‡	8.3	‡‡
A. Schulman Fine (AS)	850‡	‡‡	37	‡‡
Bonded CF	214**	0.4	0.9	10%
Bonded 4AS:1CF	570**	0.4	100	10%

(Values experimentally determined except where noted.)

* 40 psi σ_c
† 20-50 psi σ_c
‡ In unidirectional confined compaction.
** Material properties of the Rubber Medium are dominant in DISLASH tests due to thin layer of material over thick rubber block.
‡‡ Granular material was not bonded for this test. (Data not available.)

Dow Corning 200 Fluid [76]:

Table B.2 DISLASH Fluid Parameters

Viscosity (centistokes)	Specific Gravity (@ 25 C)	Surface Tension (dyne/cm @ 25 C)	Bulk Modulus [77] (MPa)
1000	.971	21.2	965
10000	.975	21.5	965
60000	.976	21.5	965
100000	.977	21.5	965

(All values supplied by manufacturer)

Wellbore Radius: $R_w = 0.278$ cm

Possible Flow Rates:

Table B.3 DISLASH Flow Rates

cm^3/sec
0.004929
0.010474
0.020948
0.041896
0.083791

(Although flow rates in the text may be rounded to more convenient numbers, e.g. 0.04, the values above were used for all calculation purposes.)

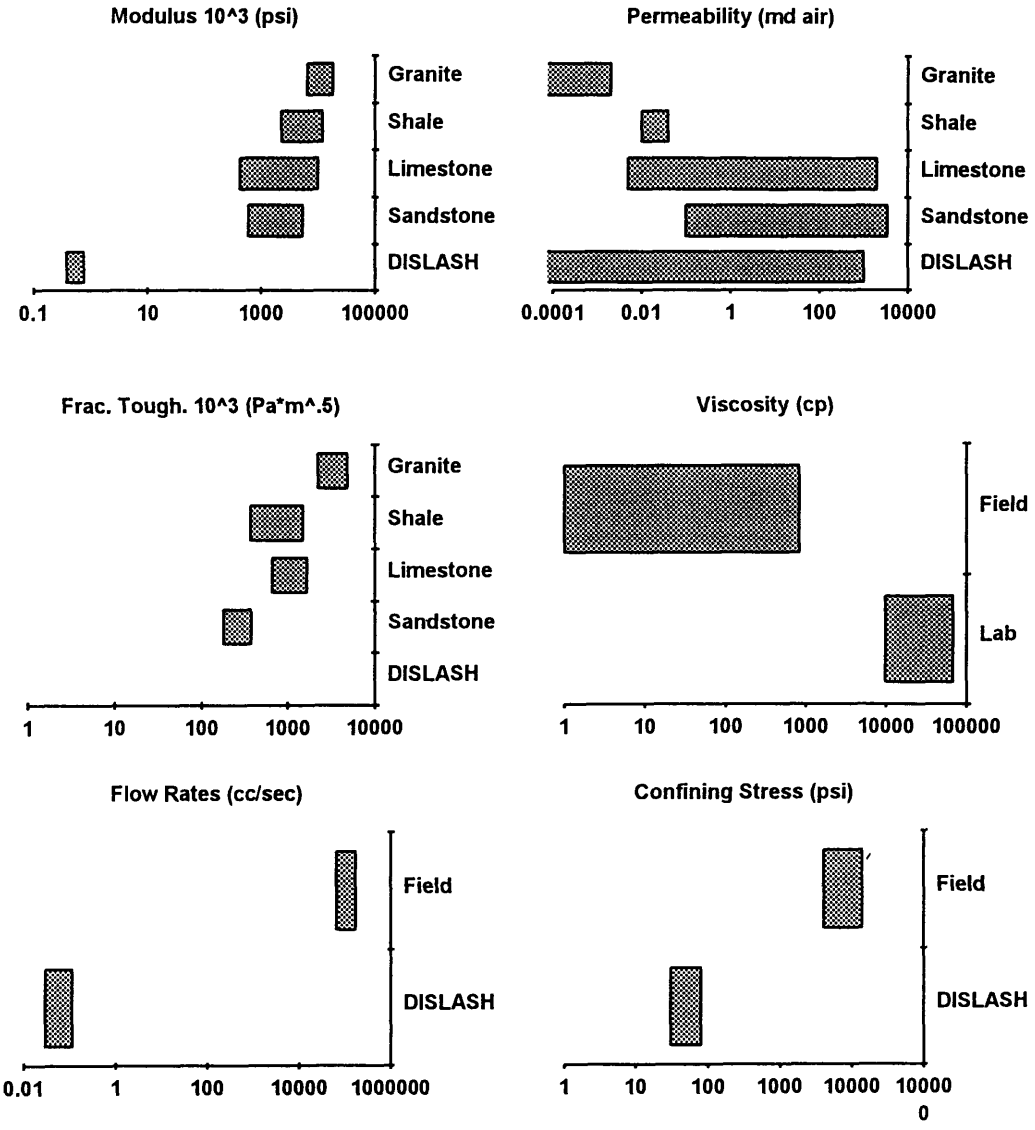

Figure B.1 Field and Lab Parameters

The bars represent typical lab and field values for relevant material properties and operating parameters encountered in the field and used in the laboratory. The fluid rheology properties used represent the range possible with numerous different types of fluids. The minimum values are for fresh or salt water, while the maximum field value shown represents a borate-crosslinked fluid containing hydoxypropyl guar to produce thickening. Values were compiled from many sources, namely Refs. [1,6,78].

B.2.1 Granular Materials:

The permeabilities of the granular materials were first tested by tightly packing the particles without the glue binder. The results are shown in Figure B.2 below. As can be seen there are only small changes in the permeability with changes in the size distribution of the particles. The addition of the glue binder significantly changes the behavior of the materials. One of the greatest changes is, particle size distribution becomes significantly more important and it is possible to tightly control the permeability by controlling the ratio of different particle sizes.

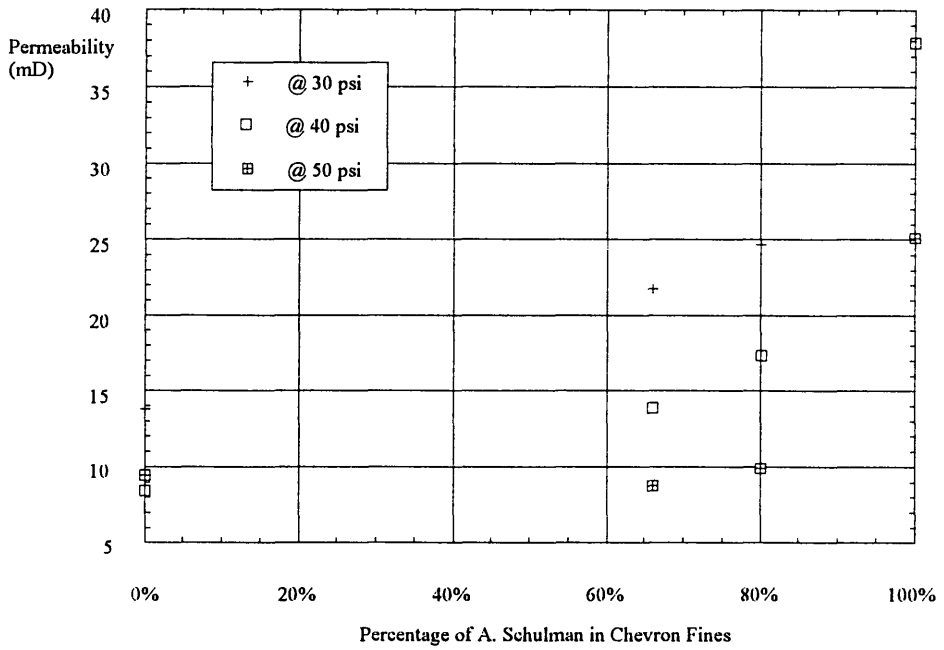

Figure B.2 Permeability of Unbonded Granular Materials
The data points represent average data for tests at several different concentrations of A. Schulman granular material mixed with Chevron Fines. Tests were not run below 50% because the permeability contrasts were not significant.

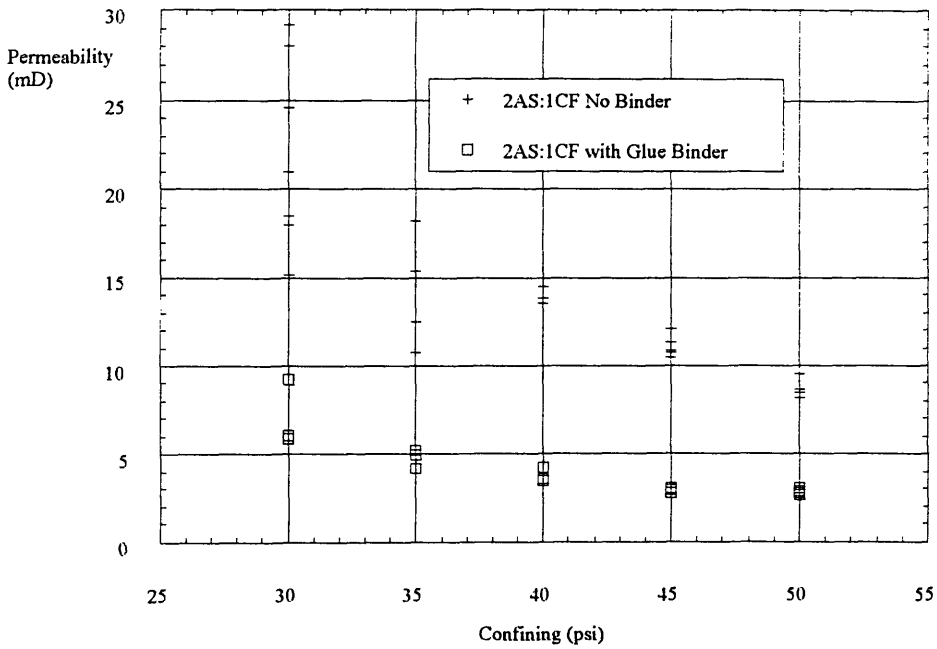

Figure B.3 Permeability of Bonded vs. Unbonded Granular Materials

Other size combinations of granular materials also exhibit similar decreases in permeability when bonded.

APPENDIX C
Contact Stress Measurement

C.1 Introduction and Background

DISLASH simulates underground hydraulic fracture by injecting fluid into the interface between a "rigid" PMMA block and a low modulus Silastic rubber block. In order to simulate the large underground confining stresses, the rubber block is pressed against the PMMA using a rolling diaphragm. As shown in Figure C.1, the pressure inside of the DISLASH housing pushes the diaphragm up, rolling the diaphragm back, and pressing the top surface of the block against the PMMA. Measurement of this contact stress has been attempted by several researchers [11,67] with limited success and large amounts of error.

C.1.1 Significance

Although it has been determined that there is a small dependence between fracture growth and confining stress [11], the principle concern is the variation of the contact stress over the surface of the block. The confining pressure in the DISLASH housing can be tightly controlled and is measured with each test, therefore, any change in this parameter can be incorporated into the data reduction phase. The surface confining stress, or *contact stress*, however, can vary as a function of position on the block. Any change in the contact stress would significantly alter the fracture growth pattern (which is the principle area of interest for permeability barrier studies).

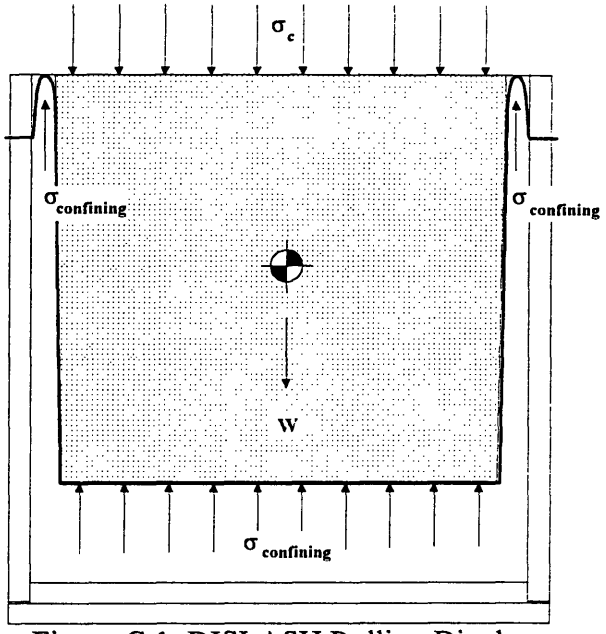

Figure C.1 DISLASH Rolling Diaphragm

The confining stress ($\sigma_{confining}$) is produced with shop air pressurized to a known, constant value. The DISLASH rolling diaphragm seals the gap between the top ring and the bottom portion of the chamber and transfers the pressure to the Silastic Rubber block, forcing the block against the PMMA producing the actual contact stress (σ_c).

C.2.2 Previous Work

Numerous methods of measuring the contact pressure in DISLASH have been devised and tested with only limited success. The first attempt used a surface mounted transducer, which failed to perform satisfactorily due to imperfections in the surface finish of the mounting configuration, coupled with poor deflection matching between the rubber block and the transducer surface. Also, the surface area of the transducer could only produced a very course mapping of the surface. A second method used a matched block with a hole connected to the interface, this hole was then connected to a transducer to measure the pressure of the fluid in the hole. The main problem with this technique stemmed from the inconsistent amount of fluid in the hole. The most successful method involved pumping a small volume of fluid into the interface through a small bore hole and then watching the pressure falloff rate to determine the contact stress from inflections in the time - pressure history. This method failed due to poor experimental

construction that allowed leaks in the fluid lines, and poor implementation due to the fact that the volume of fluid pumped into the interface was not readily controllable. The tests generally failed because the contact stress could only be measured in a small number of locations, and repeatability concerns could not be resolved.

C.3.3 Current Work

The measurement technique described in this Appendix was used successfully to map the contact stress over the block surfaces. To verify the technique, the surface was also changed to produce a step change in contact stress, to simulate channel geometry configurations.

A special testing apparatus, shown in Figure C.2, was designed to measure the contact stress in six locations in the interface. The block, shown below, was constructed of 3/4" PMMA with six equally spaced, radial bore holes leading to small access holes to the interface. The block could then be rotated to eight different positions to measure a total of 41 positions. (The center probe measures the radial center of the block for each rotation of the block.) The probes were filled with a low viscosity fluid, 1000 cSt DC200 fluid, and connected to a transducer and positive displacement pump. To run the test a small amount of fluid (<0.05 ml) was injected into the interface and then the system was sealed. The fluid was then allowed to leakoff into the interface surrounding the probe. It was theorized that after sufficient time the fracture below the probe would grow sufficiently thin that it could be considered closed, thus providing an accurate measure of the fluid pressure required to maintain the interface in an horizontal level as shown in Figure C.3.

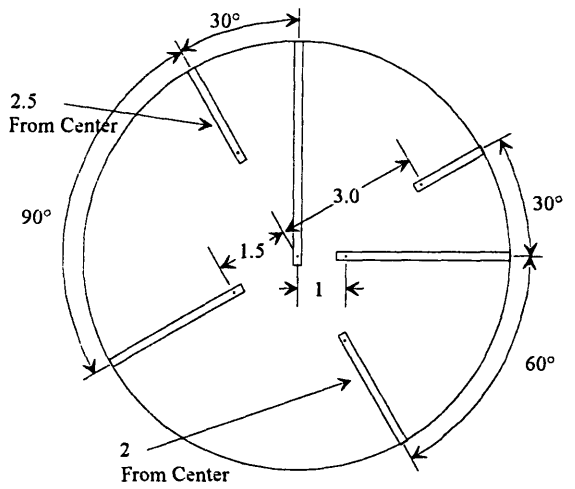

All Dimensions in Inches

Overall diameter 8 7/8"

1/2" thick plexiglass sheet

Boreholes, 11/64" Diam

Probeholes, 1/32" Diam

Figure C.2 Contact Pressure Measurement Plate

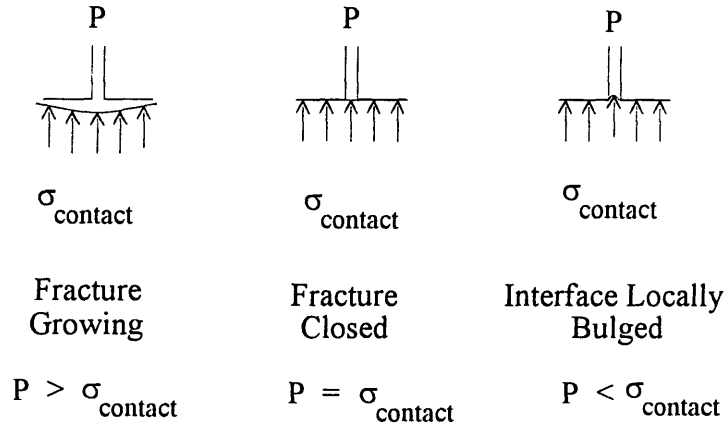

Figure C.3 Schematic of Fluid Under Tester Probe

The three possible situations shown above represent the extremes of the test behavior. The leftmost figure represents the case where the fluid is still moving out from the probe and the fluid pressure is greater than the contact stress. The rightmost figure shows the case where insufficient fluid was present in the probe and the rubber is locally bulging into the probe. This situation produces fluid pressures lower than the contact stress. The middle figure represents the desired condition where the fluid has the same pressure as the contact stress.

A computer program was written to inject a specified amount of fluid into the interface, collect the peak pressures, and the pressure after a fixed length of time.

Several tests were done to collect the complete time history of the pressure to check for inflections in the curve as mentioned above, but the data proved highly prone to scatter.

Multiple test runs were run and the 5 min. pressure proved the most repeatable, (with less than 1% scatter). After 3 min. the pressure had ceased to fall and the fluid was considered completely leaked off into the interface. The stresses for each location were then averaged and plotted as a function of center point stress. This gave an indication of the variation of stress over the interface.

C.4 Theoretical Prediction

The contact stress should be uniform over the entire surface, except very near the edges, and somewhat higher than the confining stress in the DISLASH housing. The free body diagram in Figure C.1 demonstrates this by showing the vertical component of contact stress in the interface, balanced by the pressure applied over the bottom of the block, and also applied on the edges of the rolling diaphragm. The weight of the block should also be taken into consideration, although the weight (11.75 lbf.)* is significantly less than the force generated by the confining pressure acting over the bottom surface of the block (865 lbf.)*. Following this logic, the absolute minimum for the contact stress would be the value of the confining pressure minus the weight divided by the surface area of the block.

C.5 Experimental Results

The important result of this work is the comparison of the measured values to theory which confirms the concept that the contact stress is higher than the confining value, as shown in Figure C.4 below, as opposed to concepts proposed in Ref. [28]. The bottom line is the confining pressure, while the top line is the proposed theoretical value.

---

* The given values are for Little DISLASH. The force generated by the pressure acting over the bottom of the block is for 40 psi acting over a 5.25 in diameter block.

The horizontal axis is the confining pressure. The vertical axis represents the measured value. All of the data points fall into the regime between the theoretical maximum and minimum values.

A map of the contact stress over the block surface is shown below in Figure C.5. The scale to the right of the image represents the level of the contact stress in percent greater than confining stress. The difference over the surface of the entire block is less than 6% from maximum to minimum, with the localized maximum of interest occurring near the center.

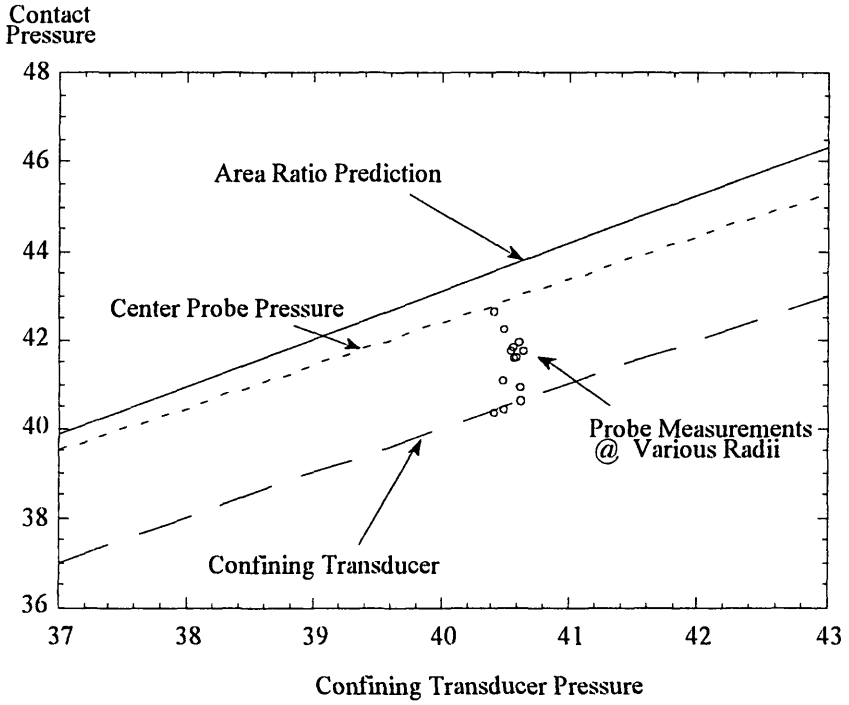

Figure C.4 Measured Values of the Contact Stress.
The theoretical maximum and minimum (confining pressure), are shown as solid lines in the figure. Note that all of the values fall between these two lines.

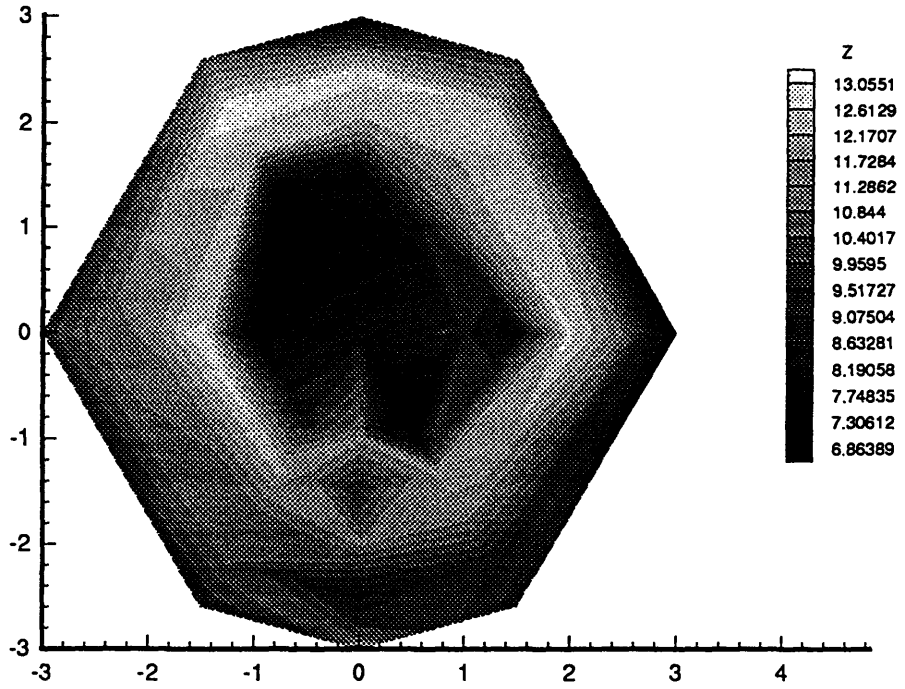

Figure C.5 Map of Contact Stress Over Surface of Big DISLASH Block. The numbers on the table to the right of the figure represent percent over the theoretical minimum value of confining pressure. The spread of the values over the used area of the block is only four percent except for a point approximately one centimeter from the wellbore which peaks at an additional four percent below the expected value. This 'low point' is insignificant due to the proximity to the high pressure region near the wellbore.

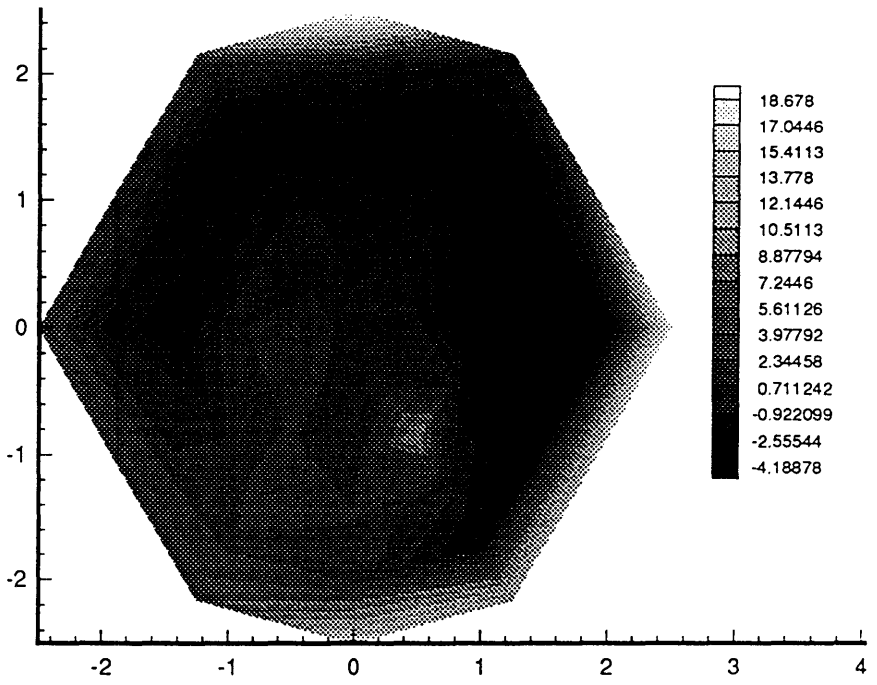

Figure C.6 Map of Contact Stress for Channel Geometry in Little DISLASH. The identification of the higher pressure regions bounding the center region are slightly muddled due to the limited number of discrete points sampled for this set of tests but the sharp delineation on the right side is clear, (due to a larger number of test points near the boundary. The scale is inverted for this test to better delineate the channel zone, therefore the scale to the right of the figure represents the percent under the confining pressure.

C.6 Conclusions

The results demonstrate that the contact stress is slightly higher than the confining stress, and that only small localized regions exhibit significant variations over the surface of the block. The principle 'high points', are near the center, where the fluid pressures in DISLASH tests are typically highest which reduces the significance of this area, in terms of influencing fracture growth patterns. To confirm this statement, the results of channel geometry tests demonstrate that differences of order 20 to 30% are required to significantly affect the fracture growth.

APPENDIX D
Major Modifications to Apparatus

DISLASH was used extensively for several years prior to this work and those researchers had discovered many of the limitations of the apparatus. In the process of this work, the weaknesses have been addressed and, if not resolved, the problems have been minimized. The experimental procedure, however, has not changed significantly. Several references detail the procedure for DISLASH tests [11,45,47-49,53,66,68] and only the changes are included here.

The DISLASH system is composed of four components: the interface separation apparatus, positive displacement pumps, various pressurization sub-systems, and the data acquisition and control sub-system. During the process of this study, all four of the sub-systems have been significantly modified, and a constant pressure pumping system has been developed, Ref. [68]. The data acquisition system software has been upgraded to a compilable language to increase the system response speed and versatility. Reduction of error, useability, flexibility, ease of maintenance, and repair were the prime considerations for system modifications.

D.1 Improved Signal to Noise Ratio

The signal to noise problem, repeatedly mentioned in Ref. [11], was remedied using a reference voltage configuration for the data line channels, where the output of the transducers was recorded relative to the input voltage. This method not only reduced the noise significantly, but also produced more stable calibration curves. Increased electromagnetic shielding of the transducers and data lines, coupled with prudent choice of the sampling frequencies produced marked improvements in the system performance.

Figure D.1 shows typical, unfiltered 10 Hz pressure data from the current system, compared to 10 Hz data using the previous computer data acquisition system, cabling, power supply, and software.

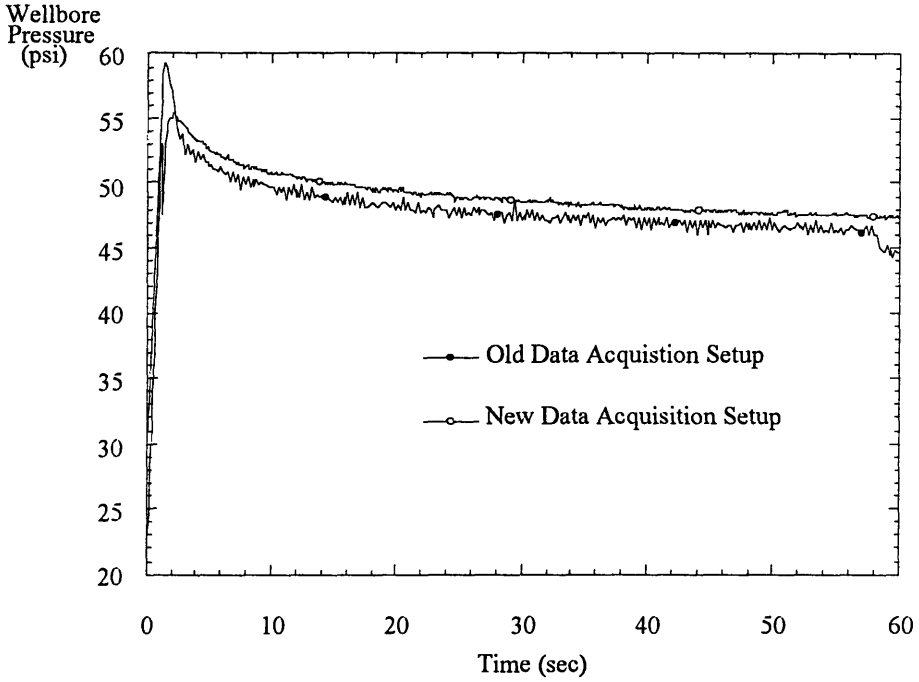

Figure D.1 Comparison of Old and New Data Acquisition Data.
This data is from two 10000 cSt, impermeable Little DISLASH tests identical except for the data acquisition power distribution system. The *Old* data is taken from the start of the project, while the *New* data is from near the end of the project. The improvement in signal to noise is obvious from examining the 'smoothness' of the two curves.

D.2 Increased Time Resolution

Radial growth data is recorded manually by striking a key at predefined radii as the fracture is growing. The previous DISLASH data acquisition system was not capable of recording the rapid key presses that are required during the rapid growth after initiation. This problem introduced a delay into radius vs. time data that was inconsistent with the pressure vs. time data. Other researchers have noted the seemingly incongruous time shifts (e.g. Refs. [11,39]). A combination of rewriting sections of code and moving to a computer system with a faster bus design has eliminated this problem. The control

system pre-pressurizes the wellbore to the same pressure, typically 35 psi, prior to the start of every test. By pre-pressurizing and reducing the compliance of the system, the time shift has been reduced and is uniform from test to test, which eliminates elaborate the shifting schemes used by others. [11,12]

D.3 Other Changes

In order to perform meaningful permeable testing, the positive displacement pump was replaced with several larger volume bore pumps to allow for longer tests with more leakoff. To facilitate refilling these new pumps, a fluid reservoir was attached to each pump. Multiple pumps were constructed to minimize system down-time when changing fluid viscosities. An additional improvement, coupled to the replacement of the pumps, was the decrease in system compliance. To prevent contamination of the pump with air, the attached fluid reservoir, a dual o-ring piston in the pump, and tighter tolerances on the attachment fittings, sealed the possible leakage areas. Refilling of the pump, the time at which the most air would be drawn into the pump, was done at a slower flow rate, 0.02 to 0.005 cc/sec vs. 0.04 cc/sec. The slower flow rate prevented large pressure drops in the fluid supply system that would place the fluid under vacuum.

An older version of DISLASH, now called Big DISLASH, discussed in Refs. [49,50], was retrofitted with a rolling diaphragm, stiffer linkage connections, and improved seals. The larger Silastic rubber block allowed larger diameter tests, coupled with easier preparation due to the pneumatic lifting mechanism, greatly increased accuracy and general productivity.

Other changes involved rebuilding the probe lines and other supply lines to eliminate leaks, reworking the pressurization sub-system to accommodate the added equipment, and other numerous smaller tasks which culminated in the completed DISLASH system shown in the Figures below. Figure D.2 show Big DISLASH which

has a block diameter of 7½" as compared to 5" for Little DISLASH shown in Figure 1.4. The total system schematics are shown in Figures D.3 and D.4.

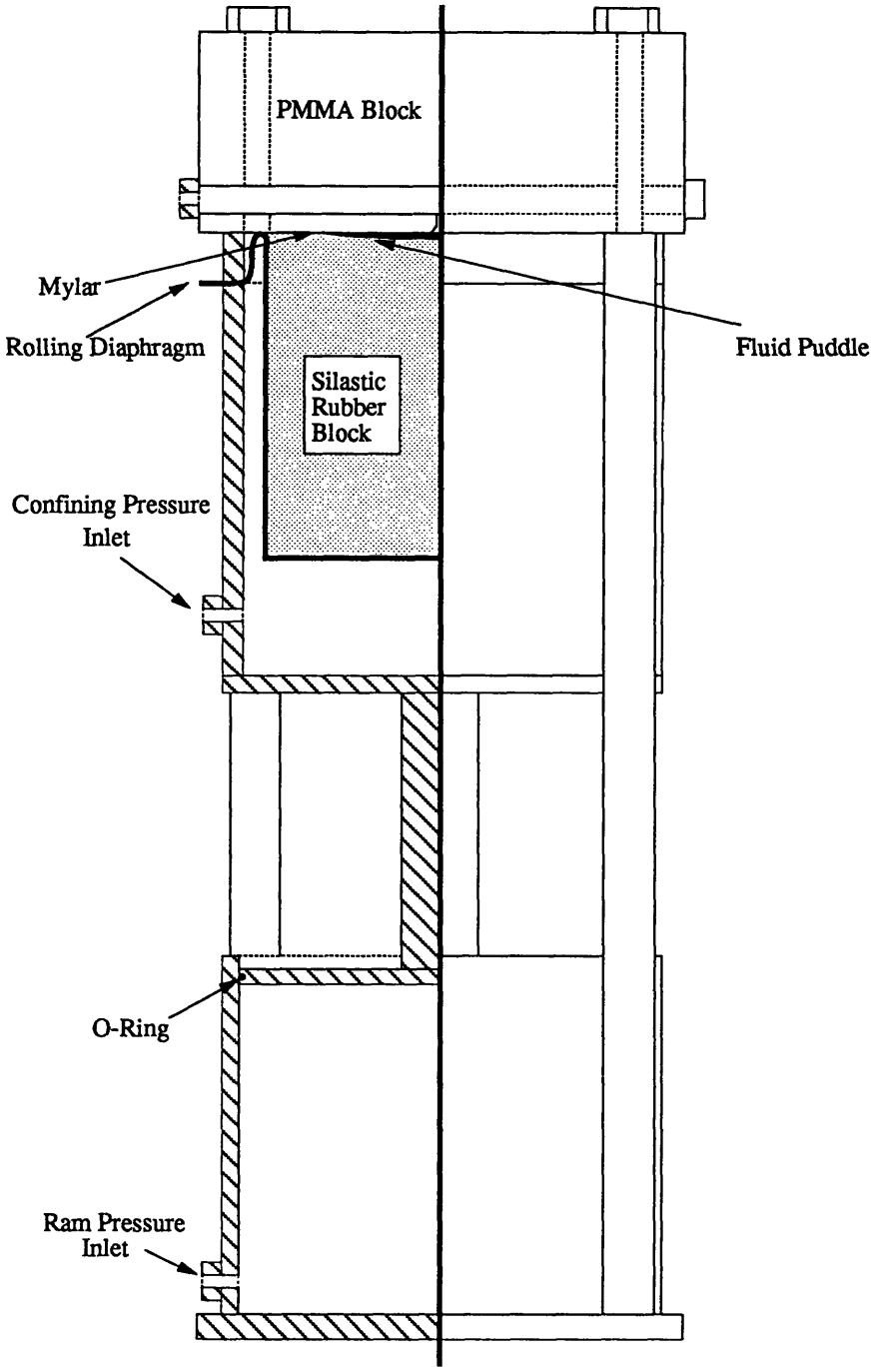

Figure D.2 Big DISLASH Side View.

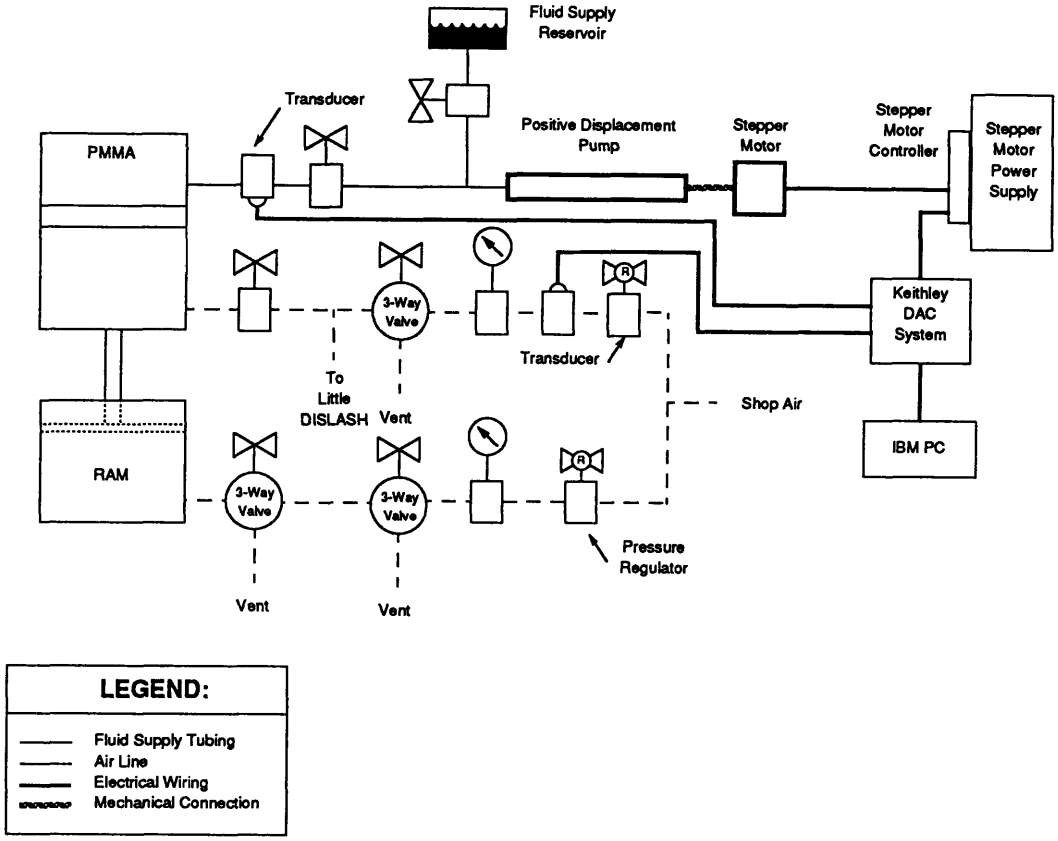

Figure D.3 Big DISLASH System Schematic.

The experimental procedure for DISLASH is well documented in Refs. [11,45,47-49,53,66,68] but the main points are represented here. First the interface must be cleaned using a soft cloth to remove any excess fluid from previous tests. Once the surface is clean, the permeable sample can be placed on top of the Silastic block. In the case of Big DISLASH, the ram can then be pressurized to 20 psi over the desired confining pressure to raise the chamber and diaphragm into place. For Little DISLASH the chamber must be held in place by manually tightening bolts that serve to hold the PMMA and aluminum cylinder tightly together.

Confining pressure can then be applied and allowed to stabilize. For Little DISLASH it is necessary to pressurize the probes to just below the confining pressure (2 psi for a 40 psi test). The data acquisition system can then be started and the test parameters inputted following the on-screen instructions. Important here are the

sampling rate, 10 Hz, volume of fluid to be injected, and total test time, 300 sec. Once the computer is initialized the test can begin.

The first key press pressurizes the wellbore to 5 psi below the confining stress level, to help prevent the time lag discussed above. The second key press begins stepping the pump. The third press records the fracture initiation time. Each additional key press records the time the fracture front, or fluid front, which ever is being measured for this test, crosses predetermined markings, (1/2 cm increments). At the end of the test the pump is stopped by pressing the escape key. As the data is being stored to disk, the confining and ram pressures can be removed and the surface of the PMMA cleaned. If the pump needs to be refilled, there is a separate program designed to refill the pump at a slower rate for a predetermined volume. The schematics represented here show the key features of the two DISLASH apparatus. It should be noted that the confining pressure lines are shared between the two setups and can be switched as needed.

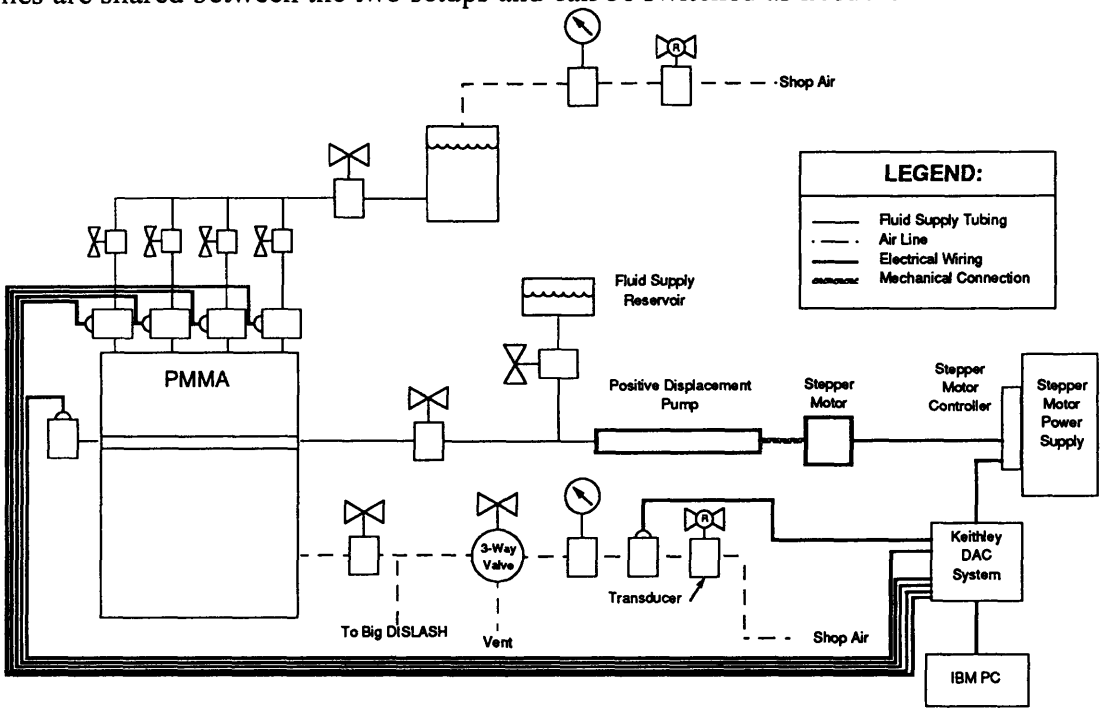

Figure D.4 Little DISLASH System Schematic.

APPENDIX E
Permeability Testing

Determining the permeability of materials has provoked numerous individuals to develop a wide array of apparatus. These can be divided into two basic types: fixed wall and flexible wall permeameters.* The permeameters used to study the foam and granular material permeabilities were of fixed wall design, necessitated by the requirement to clamp the low stiffness materials in place for accurate testing. Side leakage was prevented by large vertical clamping forces in the axial foam tests. The granular materials were tested with significantly large areas and large confining stresses to prevent side leakage. Transverse tests used a thin coating of a viscous sealant (Dow Vacuum Grease) to prevent edge leakage.

E.1 Axial

E.1.1 Compressive Permeameter

The Compressive Permeameter, shown in Figure E.1, is designed to allow axial permeability testing of a material under a specified axially confining pressure. The pressure is used to match the conditions of samples constrained vertically in DISLASH under confining pressure. This testing procedure is necessary due to the significant change in permeability of foams due to compression. It was discovered that changes in

* A particularity good description of the various types of existing permeameters can be found in Ref. [65]. The authors review the strengths and weaknesses of different configurations which were incorporated into the development of the specialized permeameters used to determine the properties of materials used in DISLASH.

the confining pressure can cause changes in the observed permeability, as detailed in Figure E.2.

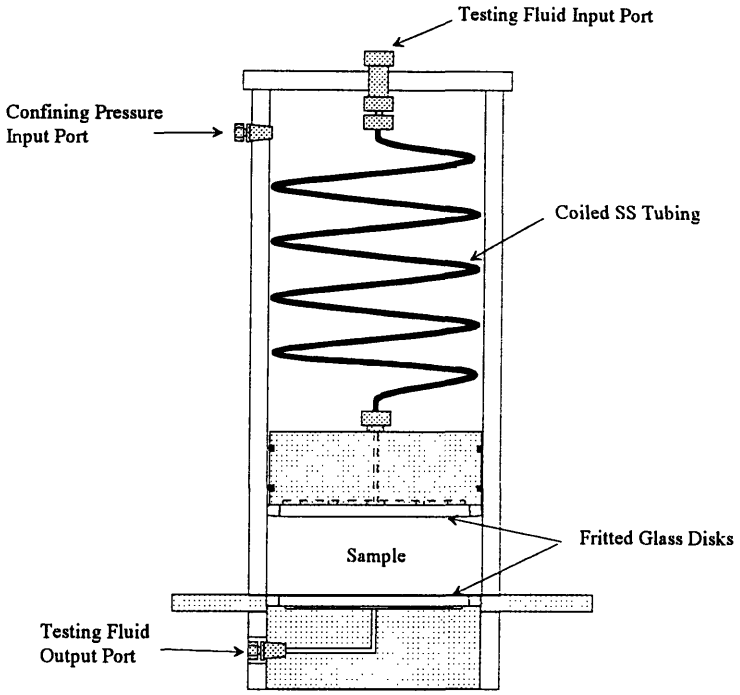

Figure E.1 Axial Compressive Permeameter Configured for Granular Sample. In order to test foam samples in this apparatus the foam is cut larger than the housing and placed between the upper cylinder and the base. The permeameter is then confined using constraint bolts (not shown) which compress the foam, effectively sealing the foam around the edges, preventing fluid leakage. This edge crushing produces minimal effects on the permeability because the confining stress in the inner portion also compresses the foam.

The testing procedure for foam involves crushing the upper body of the tester over a slightly oversized sample to seal around the edges. The top and bottom of the apparatus is then constrained using a bolt and load frame (not shown). Confining pressure can then be applied, compressing the foam. Next, fluid is injected through the testing fluid input port at a specified pressure. After the fluid flow has equilibrated, typically in less than a minute, the flow rate is determined by measuring the amount of fluid that has passed through the sample at specified time intervals. The confining pressure can then be increased and another test run. By separately measuring the stress

deflection behavior of the sample it is possible to determine the length of the sample under confining stress and calculate the permeability using Darcy's law.

Granular materials are tested similarly, except the sample is placed inside of the upper housing after a layer of vacuum grease has been applied to the inner housing to seal against edge leakage.

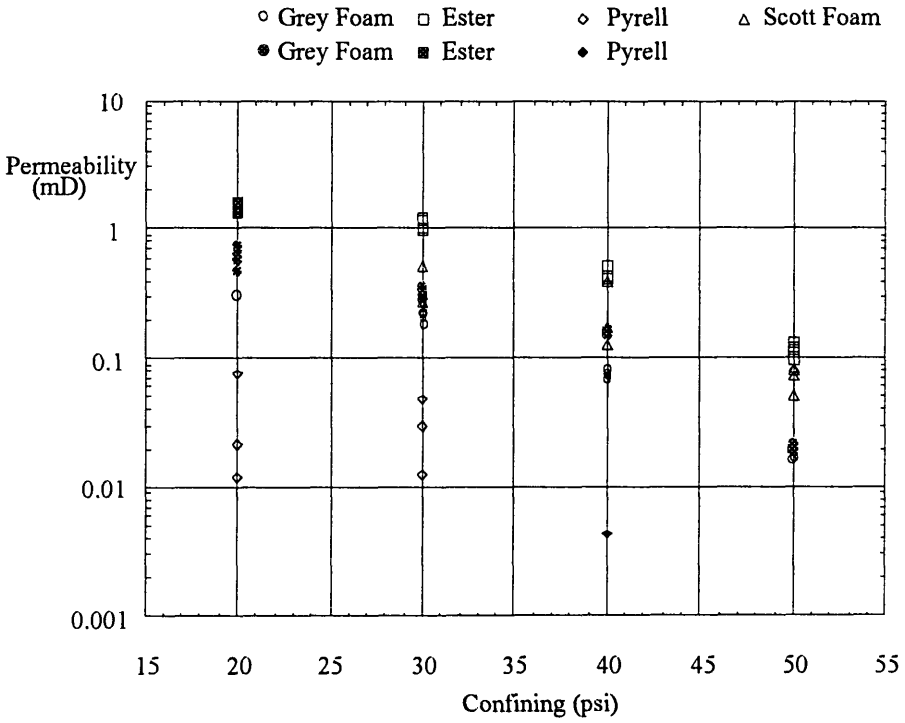

Figure E.2 Axial Permeabilities of Several Foams
Axial permeabilities of the foams vary significantly as a function of confining stress.

E.2 Transverse

E.2.1 COSPERT

Transverse permeability was measured in a similar device originally conceived to test the transverse permeability of Ottawa sand under large confining pressures, (hence the name Crushed Ottawa Sand PErmeability Radial Tester)**. The transverse permeameter, shown in Figure E.3, is capable of operating over a wide range of pressures

** Designed and Developed by Christian Hamer and Timothy S. Quinn, November 1993.

for confining pressures and fluid pressures. The confining pressure, typically 20 to 50 psi for foam or plastic granular material tests has also been run at pressures up to 10,000 psi for sand proppant experiments. The fluid pressures are typically maintained at 10 or 20 in Hg to ensure that the testing stays in the Darcy flow regime.

Samples are placed between the plates and the confining pressure is applied, (with compensation for system weight at low confining pressures). The samples maximum outer diameter must be 3 inches or less, as limited by the size of the plates, and the inner diameter is typically 2 inches to provide adequate sample depth without requiring excessively long times or high pressures for testing.

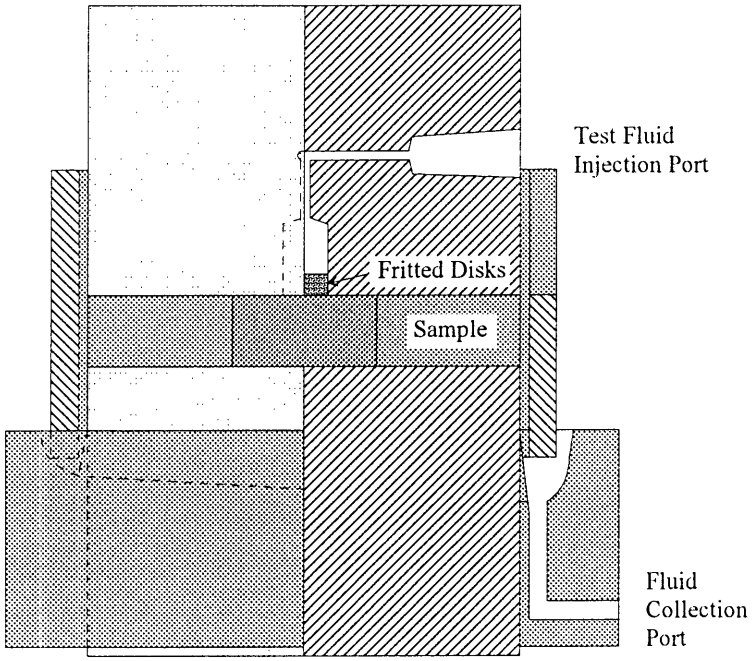

Figure E.3 Transverse Compressive Permeameter (COSPERT).

As with the axial tester, the stress deflection behavior is used to determine the height of the sample and the permeability can be determined using Equation (E.1) where h is the thickness of the sample, P_w is the driving pressure, R_i and R_o are the internal and external radii of the specimen, respectively. Typical foam transverse permeabilities are shown in Figure E.4.

$$k = \frac{Q\mu}{h2\pi P_w} \ln\left[\frac{R_o}{R_i}\right] \qquad \text{(E.1)}$$

The granular materials were similarly tested in axial and transverse directions and the results are shown in Figure E.5 below.

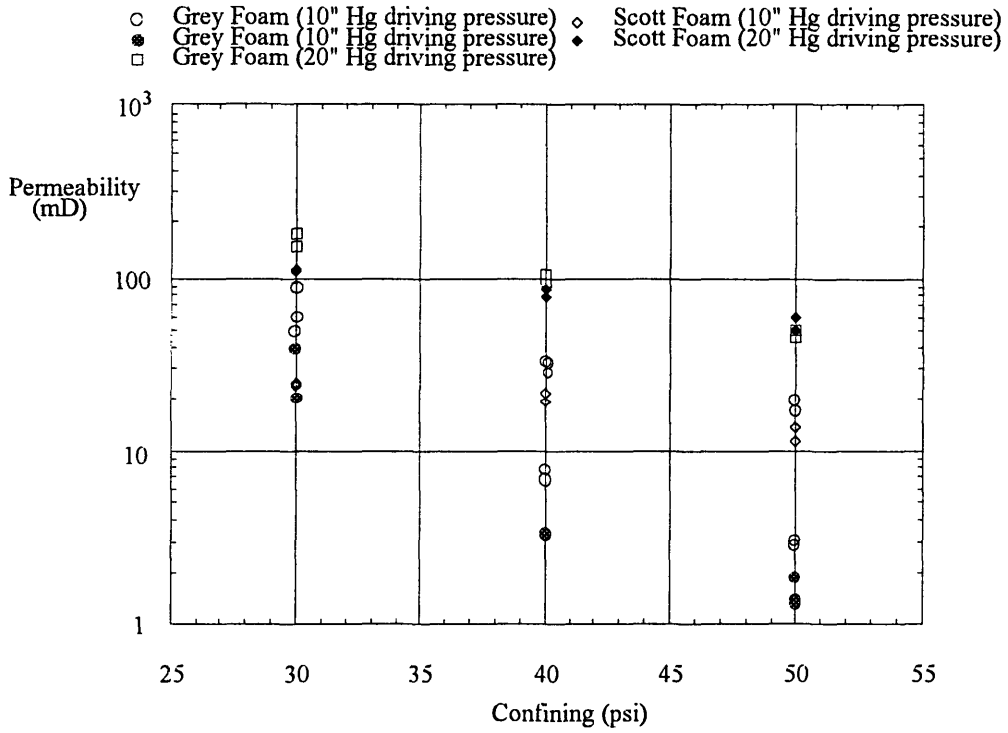

Figure E.4 Transverse Permeabilities for Several Foams

Transverse permeabilities of the foams vary significantly as a function of confining stress.

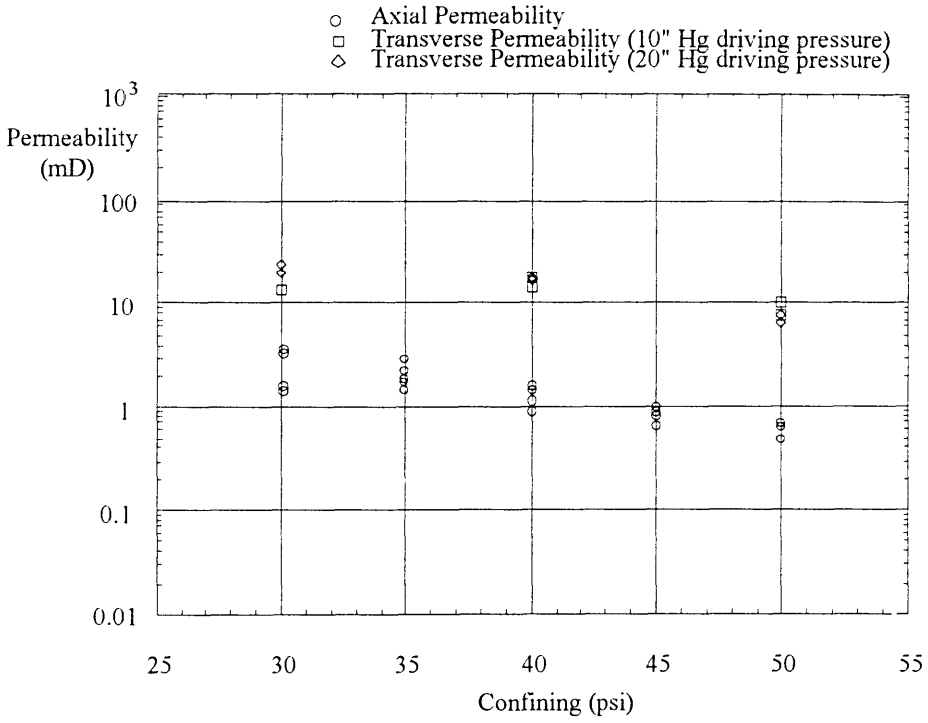

Figure E.5 Axial and Transverse Permeabilities for Bonded Granular Samples.

APPENDIX F
Dimensional Scaling

F.1 Dimensional Groups

After the relevant physical phenomena have been identified and the appropriate set of variables has been chosen (shown in Table F.1), a set of dimensionless groups can be formed algebraically, e.g. Refs. [79,80]. The grouping shown in Equations (F.1a)-(F.1e) are complete and, due the nature of dimensional scaling, non-unique.

Table F.1 Variables Used For Dimensional Scaling

Variable		Dimension
t	Time	(t)
Q	Injection Rate	(L^3/t)
R_w	Wellbore Radius	(L)
Γ	Separation Energy	(m/t^2)
$\bar{E}$	Crack Opening Modulus	(m/Lt^2)
$\bar{\mu}$	Effective Channel-flow Viscosity	(m/Lt)
K_l	Leak-off Coefficient	($L/t^{1/2}$)
σ_c	Confining Stress	(m/Lt^2)

Arranging these variables into dimensionless groups produces the following numbers [39]:

Time of Experiment: $$N_t = \frac{tQ}{R_w^3} \qquad \text{(F.1a)}$$

Crack Formation: $$N_\Gamma = \frac{\Gamma}{\bar{E}R_w} \qquad \text{(F.1b)}$$

Elastic Deformation:
$$N_{\bar{E}} = \frac{\bar{E} R_w^3}{Q\bar{\mu}} \tag{F.1c}$$

Leak-off:
$$N_{K_l} = K_\ell \sqrt{\frac{R_w}{Q}} \tag{F.1d}$$

Confining Stress:
$$N_{\sigma_c} = \frac{\sigma_c}{\bar{E}} \tag{F.1e}$$

Where the crack opening modulus, $\bar{E}$, is defined as:

$$\bar{E} = \frac{E}{4(1-\nu^2)} \tag{F.2}$$

The effective channel-flow viscosity, $\bar{\mu}$, is defined in terms of the "consistency index" K and the "flow behavior index" n which appear in the relationship between shear stress τ and shear strain-rate $\dot{\gamma}$.

$$\bar{\mu} = 2K\left(4+\frac{2}{n}\right)^n ; \qquad \tau = K\dot{\gamma}^n \tag{F.3}$$

The leakoff coefficient, K_ℓ, is defined (for high viscosity, Newtonian fluids injected into an "evacuated porous medium under conditions of linear flow" [6]) as:

$$K_\ell = \sqrt{\frac{\Delta p \phi k}{2\mu}} \tag{F.4}$$

Where the porosity, ϕ; the difference in pressure between the fluid in the fracture and the fluid in the reservoir, Δp; and permeability, k; are defined.† For use in the dimensionless numbers below, any consistent unit system can be used, (English and Field units are not consistent).

† The leakoff number is defined by the conditions of the surrounding reservoir and the fluid. This form of the leakoff number incorporates only the viscosity and relative permeability, additional mechanisms (not considered here), such as reservoir fluid compressibility and polymer wall building effects can be found in other references, e.g. [6,22,26].

F.2 Characteristic Scaling Parameters

In order to cast the above dimensionless equations into more useful forms it is possible to combine the groups into characteristic scaling parameters. These characteristic parameters can then be used to scale experimental results to the corresponding field dimensions and similarly, field values to laboratory scale for direct comparisons.

F.2.1 Characteristic Time

If leakoff and fracture toughness are neglected it is possible to define growth for a penny shaped crack as (Ref. [22,39]):

$$R = \left[\frac{9}{4} \frac{\gamma_{12}\gamma_{14}}{\gamma_1\gamma_{13}} \frac{\overline{E}}{\overline{\mu}} \left[\frac{Q}{2\gamma_\upsilon} \right]^3 \right]^{1/9} t^{4/9} \tag{F.5}$$

Where the gamma factors, γ_{ij}, represent functional coefficients which incorporate boundary and geometric conditions. Non-dimensionalizing the above equation yields:

$$\frac{R}{R_w} = \left[\frac{9}{32} \frac{\gamma_{12}\gamma_{14}}{\gamma_1\gamma_{13}} \frac{\overline{E}}{\overline{\mu}} \left[\frac{Q}{\gamma_\upsilon R_w^3} \right]^3 \right]^{1/9} t^{4/9} \tag{F.6}$$

By reforming Equation (F.6), above, to the functional relationship expressed in Equation (F.7), the characteristic time, τ^*, can be expressed as a function of the above dimensionless groups as in Equation (F.8)

$$\frac{R}{R_w} = f\left[\frac{t}{\tau^*} \right]^{4/9} \tag{F.7}$$

$$\tau^* = \left[\frac{R_w^3}{Q} \right]^{3/4} \left[\frac{\overline{\mu}}{\overline{E}} \right]^{1/4} = \frac{t}{N_t N_{\overline{E}}^{1/4}} \tag{F.8}$$

Despite τ^*'s generality, the nature of the characteristic time still remains. It should be noted that while previous researchers [11,39,45] have used this characteristic time to produce master curves, the results were based strictly on impermeable conditions.

Though τ^* can be used to scale results of permeable tests, master curves would not be produced due to the leakoff from the fracture. Attempts to produce master curves using the efficiency term described in Chapter 1 were successful for only discrete points in the fracture growth history, as one would expect, given the leakoff area dependence on fracture radius.

F.2.2 Characteristic Pressure

It is possible to similarly derive a characteristic pressure, σ^*. [22,34,39] Equation (F.9) represents the functional form of the pressure - time relationship, and Equation (F.12) gives the form of σ^* once the characteristic time has been removed from the right hand side of Equation (F.11).

$$\frac{\sigma_{net}}{\sigma^*} = g\left[\frac{t}{\tau^*}\right] \tag{F.9}$$

$$\sigma_{net} = \frac{\bar{E}}{\gamma_1}\left[\frac{4}{9}\frac{\gamma_1\gamma_{13}}{\gamma_{12}\gamma_{14}}\frac{\bar{\mu}}{\bar{E}}\right]^{1/3} t^{-1/3} \tag{F.10}$$

$$\sigma^* = \left[\left[\frac{\bar{E}}{R_w}\right]^3 \bar{\mu}Q\right]^{1/4} \tag{F.11}$$

F.2.3 Characteristic Radius

Although R_w does not share the superscript asterisk with the other characteristic numbers, the wellbore radius is also used as a scaling parameter to provide a length scale to the equations.

APPENDIX G
Inverse Permeability Barriers

This work has focused on the examination of permeability barriers to hydraulic fracture propagation and the underlying equations are valid for a wide range of conditions, with the assumption that the originating permeability is greater than the approaching permeability, $k_1 \geq k_2$. If the approaching permeability (k_2) is lower than the permeability in the initiated section of the fracture the fracture will be drawn into the lower permeability zone due to increased propagation performance. This situation is much more complex to model theoretically due to complicated leakoff geometry at the interface. Experimental investigations have confirmed the hypothesis discussed above and the results are shown below. It should be noted that the photographs emphasize the fluid front, but the preflood zone is not significantly large due to the low permeabilities and high viscosities used for this test.

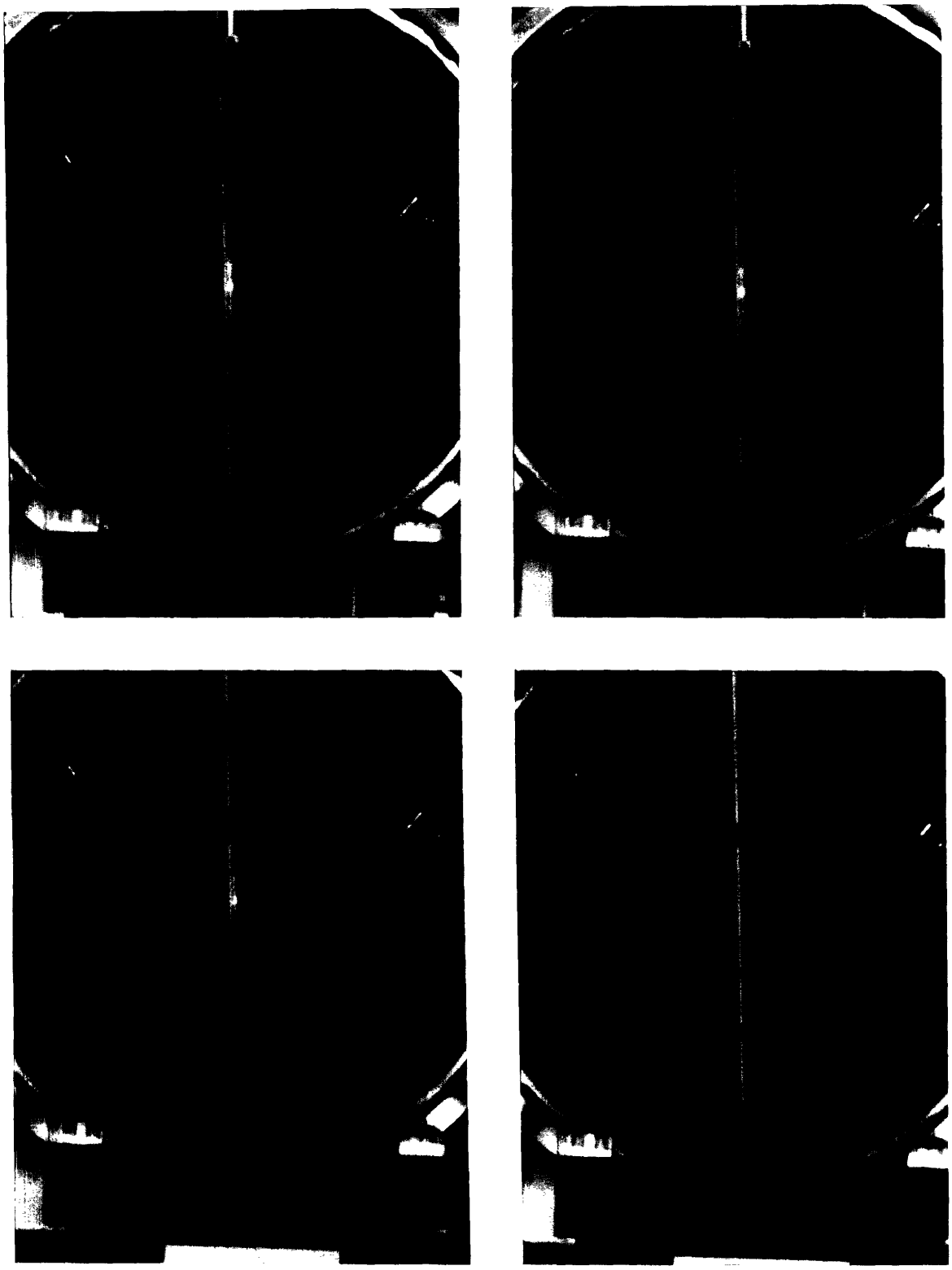

Figure G.1 DISLASH Simulation of Fracture Growth ($k_2 > k_1$).